COMPUTATIONAL INVESTIGATIONS OF THE ELECTRONIC STRUCTURE AND PROPERTIES OF BIMETALLIC BIOMIMETIC COMPEXES

A Dissertation

by

LINDY CHASE ELROD

Submitted to the Graduate and Professional School of
Texas A&M University
in partial fulfillment of the requirements for the degree of

DOCTOR OF PHILOSOPHY

Chair of Committee,	Marcetta Y. Darensbourg
Co-Chair of Committee,	Michael B. Hall
Committee Members,	Timothy Hughbanks
	Jamie C. Grunlan
	Micah J. Green
Head of Department,	Simon W. North

December 2021

Major Subject: Chemistry

ABSTRACT

Enzymes have evolved to perform specific functions with high efficiency and selectivity. It is estimated that approximately a quarter to a third of all proteins contain an essential metallic cofactor that enables catalysis of reactions that would difficult to perform otherwise. Certain classes of enzymes have evolved to incorporate multiple metals within their active sites to control their reactivity such as iron-iron hydrogenase, nickel-iron hydrogenase, and carbon monoxide dehydrogenase. The multiple metal centers can help position substrates, fine tune the potential for electrochemical transformations, or allow for more complicated chemical transformations than would be possible with a single metal. Density functional theory can expand upon experimental models of these enzymes by calculating potential intermediates and investigating possible mechanisms where experimental methods are insufficient or too impractical.

Computational investigations of a series of nickel-iron hydrogenases give insight into the increased oxygen tolerance of the selenium variant of the [NiFe]-Hydrogenase. Selenium forms a weaker terminal bond to oxygen disfavoring the formation of doubly oxygenated species and instead preferentially forming a singly oxygenated complex. This singly oxygenated complex is then capable of repairing the oxygen damage through a more accessible reduction process.

In another study, a dimanganese complex's assembly in solution was shown to proceed through a series of intramolecular rearrangements promoting loss of carbon monoxide ligands. The exchange of labeled ^{13}CO was found to go through an associative

interchange mechanism where an incoming CO breaks the bond between the manganese center and either a sulfur or amidic oxygen ligand followed by scrambling through a trigonal prismatic transition state.

Finally, the magnetic properties an iron-nitrosyl/nickel-dithiolene with four isolated radicals were interpreted by calculations to possess strong antiferromagnetic coupling of the central two radicals and weak ferromagnetic coupling between the two outer ones leading to a narrow gap between the ground state singlet and a low-lying triplet excited state. The electronic structure of this system was further described by using a linear H_4 model and full configuration interaction calculations to model the additional excited states.

DEDICATION

To my parents, Mike and Lisa, thank you for seeing my potential and giving me every chance to fulfill it along whatever path I chose. You have never doubted me and I have never once doubted your love and pride for everything I've done. Your sacrifices to get me here will never be forgotten or underappreciated.

To my grandparents, I wish you were here to see this.

To Chesley, for holding me together through this journey.

ACKNOWLEDGEMENTS

I would like to thank my advisors, Dr. Darensbourg and Dr. Hall, and my committee members Dr. Hughbanks, Dr. Grunlan, and Dr. Green, for their guidance and support throughout this arduous journey.

Thank you to my colleagues in Darensbourg and Hall groups for all the insightful discussions and troubleshooting. I would like to give special thanks to the following group members for their help and support, which has allowed me to be where I am today: Xuemei, who has been my closest collaborator. I believe we are both better for having met and I cannot imagine a better partner to have done so much of this work with. Manuel, Zachary, Trung, and Kyle for bantering ideas with me and opening my mind to chemical possibilities I would never have conceived of otherwise. You are the most productive lunch group I've ever had.

This journey would not have been possible without the wonderful people in the First Year Program, Dr. Lee, Dr. Pellois, Dr. Altemose, Veronica, Kelley, Travis, and Ken, who helped me grow as an educator and find my voice in the classroom.

Thank you to Dr. Perez of the Texas A&M High Performance Research Computing facility who walked me though technical troubleshooting when I barely understood how the computers I worked on operated. You have the patience of a saint and your ability to fix a problem I cannot explain continues to astound me.

None of this would have been possible without Cynthia Harper who inspired and encouraged my love for chemistry, leading to where I am today.

To Dr. Anne Gorden, my undergraduate research advisor, you gave me a place to learn and grow as a chemist and created a space that was challenging yet friendly. You helped me find my love of outreach and let me change course when I discovered a new chemical passion of inorganic chemistry. You helped cultivate that passion and recommended I apply to Texas A&M so without you this never would have happened.

To Chesley, when people ask if I would go through all of this hardship again, I always say yes. Not because of what it has given me professionally but because it gave me the chance to meet you. I wouldn't have survived this trial without you and I look forward to experiencing the rest of my life's adventure with you.

To my family, being halfway across the country from all of you has been one of the hardest parts of this journey. I have missed so many tailgates, lake days, dinners, holiday gatherings, births, and funerals in pursuit of this dream and your never wavering support and pride has meant more to me than I can ever express.

To my friends in College Station: Thank you for the laughs in the good times and listening to my rants in the bad. Kevin, for being the best desk mate I could ever ask for. Nate and Seth, for making Lazy Lane a home I could always look forward to entering at the end of the day. I'll see you on Wednesday. Angelo, Taylor, Chuck, Simone, Hayley, and Zach, for stupid games, good food, backyard volleyball, and spirited debate.

And finally, to my friends back home: Saxon, David, Will, and Bradley, reconnecting with you halfway through this journey is partly responsible for me being able to finish it. I may have spent more hours than I should admit staying up late to talk and

game with you but my sanity thanks you for the stupid jokes and nonsense conversations over the years.

CONTRIBUTORS AND FUNDING SOURCES

Contributors

This work was supervised by a dissertation committee consisting of Marcetta Darensbourg (Committee Chair), Michael Hall (Committee Co-Chair), Timothy Hughbanks and Jamie Grunlan of the Department of Chemistry, and Micah Green of the Department of Chemical Engineering.

The experimental work in this dissertation includes contributions from Trung Le (Chapters 2 and 3), Haley Naumann (Chapter 2), Hao Nguyen (Chapter 3), Manuel Quiroz (Chapter 4), Joseph Reibenspies (Chapter 2), Dr. Mohamed Saber (Chapter 4), Yohannes Rezenom (Chapter 2), Valeria S. Vega (Chapter 2), and Xuemei Yang (Chapter 2).

All computational work was conducted using resources from Texas A&M University's High-Performance Research Computing Facility and Laboratory for Molecular Simulations.

All other work presented in this dissertation was completed by the student independently.

Funding Sources

Graduate study was largely supported by a teaching assistantship from Texas A&M. This work was supported by the National Science Foundation (CHE-1300787, CHE-1664866 to Michael Hall and CHE-1266097, CHE-1665258 to Marcetta

Darensbourg) as part of the Robert A. Welch Foundation (A-0648 to Michael Hall and A-0924 to Marcetta Darensbourg).

The contents of this dissertation are not representative of the views of the above organizations.

NOMENCLATURE

AGUI	AMPAC Graphical User Interface
AIM	Atoms in molecules
BS	Broken symmetry
CCSD(T)	Coupled Cluster with Single and Double Excitations and Perturbated Triplet excitations
CH_4	Methane
CO	Carbon monoxide
CO_2	Carbon dioxide
CODH	Carbon monoxide dehydrogenase
CP^*	Pentamethylcyclopentadiene
CN	Cyanide
Cys	Cysteine
DCM	Dichloromethane
DFT	Density functional theory
DMSO	Dimethylsulfoxide
EMA	N,N'-ethylenebis(mercaptoacetamide)
EPR	Electron paramagnetic resonance
[FeFe]-H_2ase	Iron-Iron hydrogenase
FTIR	Fourier-transform infrared spectroscopy
ΔG°	Gibbs free energy change

Gly	Glycine
GSS	Ground state singlet
ΔH°	Enthalpy change
H_2	Molecular hydrogen
H_2O	Water
HER	Hydrogen evolution reaction
HF	Hartree-Fock
MBH	Membrane-bound respiratory [NiFe]-hydrogenase
MeOH	Methanol
MO	Molecular orbital
NAO	Natural atomic orbital
NBO	Natural bond orbital
[NiFe]-H_2ase	Nickel-Iron hydrogenase
NMR	Nuclear magnetic resonance
O_2	Molecular oxygen
ORR	Oxygen reduction reaction
QM/MM	Quantum mechanics/molecular mechanics
ΔS°	Entropy change
Ser	Serine
SMD	Solvation model based on density
SMM	Single molecule magnet
SOMO	Singly occupied molecular orbital

THF	Tetrahydrofuran
TOF	Turnover frequency
XRD	X-ray diffraction

TABLE OF CONTENTS

Page

LIST OF FIGURES

Page

LIST OF TABLES

Page

CHAPTER I

INTRODUCTION

1.1 An Introduction to Theoretical Efforts on Biomimetics

As the world moves towards widespread use of renewable energy sources a significant challenges is the capture and storage of excess energy generated during low demand hours for later use.[1] A solution being explored by chemists is conversion of the excess energy in chemical bonds to be released in a later chemical reaction. A logical candidate is molecular hydrogen as it can be generated by water electrolysis and produces water as the sole product during combustion, thus creating an ideally simple and carbon-neutral cycle.[2] The greatest chemical challenges to the implementation of hydrogen as an energy storage vector are the large overpotentials required for industrial sized electrolysis setups and poor selectivity of other hydrogen generation methods. For inspiration into solving these problems, researchers have turned to the highly efficient and selective biological machines that have been optimized by millions of years of evolution- the hydrogenase enzymes. The [NiFe] subclass of hydrogenases ([NiFe]-H_2ases) reversibly catalyzes the oxidation of H_2 and some are known to possess a moderate ability to operate even at low O_2 concentrations. This oxygen tolerance is not found in the other major hydrogenase subclass, the iron-iron hydrogenases ([FeFe] hydrogenases), and is a reason the [NiFe] subclass has seen increased research interest in recent years.

Since the structure of [NiFe]-H_2ase was first characterized by x-ray crystallography in 1995 researchers have sought to investigate the active site through the use of organometallic model compounds and density functional theory (DFT) calculations

in a synergistic feedback process.[3–11] Early results confirmed the Ni(II)Fe(II) bimetallic core structure, the presence of unusual inorganic carbon monoxide (CO) and cyanide (CN) ligands on the iron center, and several paramagnetic (off-cycle) intermediates arising from either Ni(I) or Ni(III) states.[12] Another key feature of the enzyme that has been confirmed by DFT is the role of one of the terminal cysteine residues as an internal base that assists in the heterolytic cleavage of the hydrogen molecule.[13] With the structure and key features of the active site now widely agreed upon, recent theoretical investigations have focused on the finer mechanistic details of the [NiFe]-Hydrogenase enzyme with a large focus being the binding or release of H_2 as well as the possible role of hydrides in the intermediate mechanistic steps.

A major hurdle in the production of efficient catalysts for the oxidation or production of molecular hydrogen (H_2) is selectivity against other small gaseous molecules such as CO[14]. In 2017, Ogo et al. designed a [NiFe]-H_2ase model compound that was able to selectively catalyze both processes based on pH, with H_2 oxidation occurring at low pH and CO oxidation at high pH.[15] The complex features an $IrClCp^*$ moiety in place of the $Fe(CO)_2CN$ found in the enzyme while the nickel center is in a square planar N_2S_2 coordination environment serving as a metallodithiolate donor to the Ir. A DFT analysis was then used to investigate the mechanism of the two catalytic processes.[16] In a key step of the mechanism, one of the hydrides is abstracted by an acetate leaving the other in a bridging mode between the two metal centers in a geometry reminiscent of that found in the Ni-R and Ni-C states of the enzyme. This hydride bridging species is also found as an intermediate in the oxidation of CO to carbon dioxide (CO_2)

by the complex. The calculated mechanism is summarized in **Figure 1**. This catalytic inflection point allows the complex to shift its function based on its environment in a manner not unlike the possible way common predecessors of both [NiFe]-hydrogenase and carbon monoxide dehydrogenase (CODH) enzymes may have adapted to their environments based on their available energy sources.

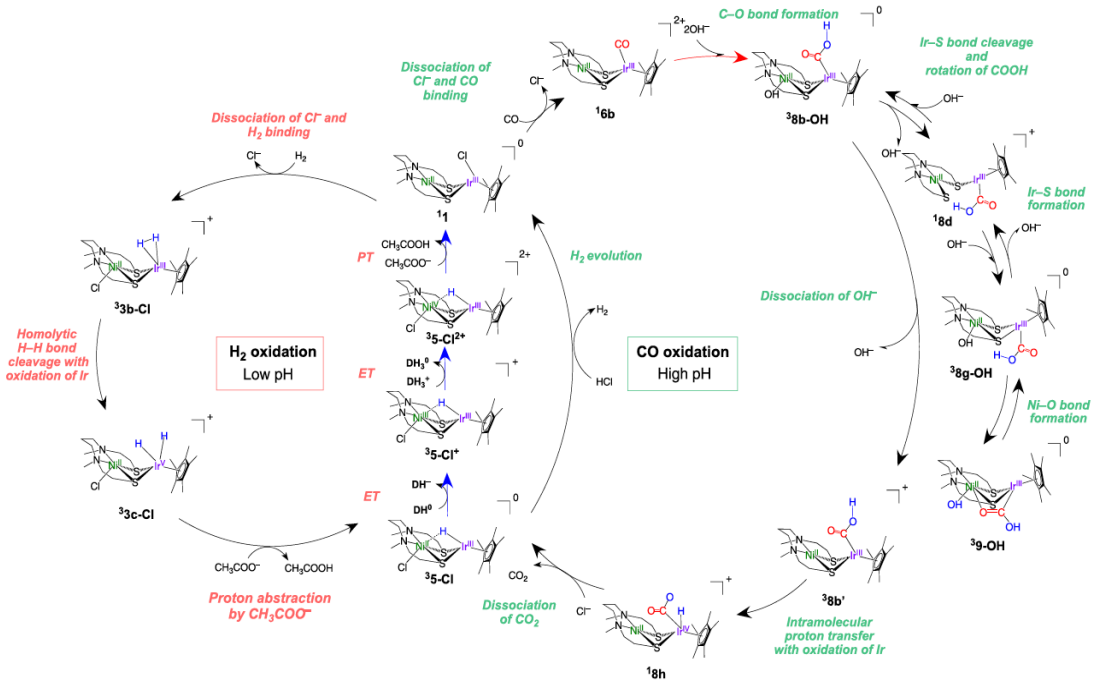

Figure 1 Mechanistic cycles for H_2 and CO oxidation by the Ogo NiIr complex. Reprinted with permission from "Selective Oxidation of H_2 and CO by NiIr Catalyst in Aqueous Solution: A DFT Mechanistic Study" *Inorg. Chem.* 2020, *59* (2), 1014–1028. Copyright 2020 American Chemical Society.

Other various mimics have been developed that can replicate the hydrogen oxidation or proton reduction catalysis of the enzymes but that fail to center the activity on the nickel atom. Ullou et al. and Isegawa et al. utilized phosphine and phosphite ligands to stabilize the metal atoms to develop model compounds that recreate the H_2 oxidation function of the enzyme, **Figure 2**.[10,17–19] The H_2 oxidation mechanisms of both complexes proceed through a bridging hydride as purported for the enzyme but with the hydride primarily bound to the Fe center and not the nickel.

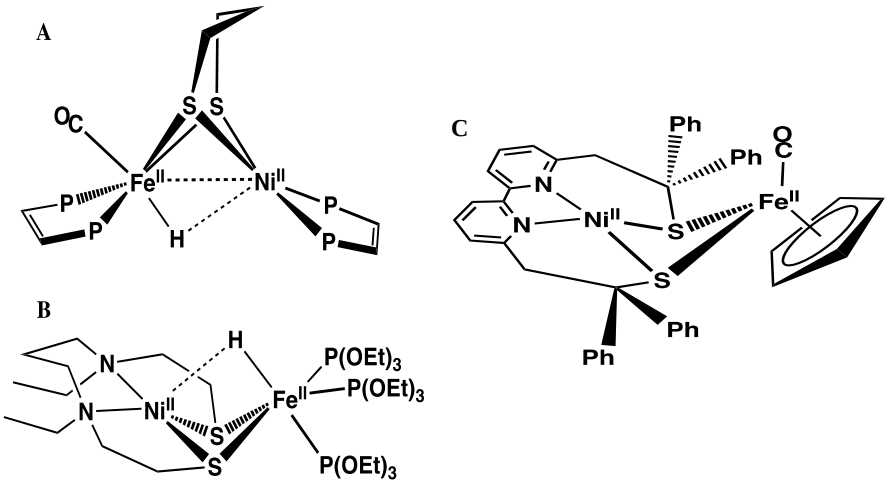

Figure 2 Biomimetic complexes from A) Rauchfuss, B) Ogo, and C) Artero.

Isegawa et al. investigated a [NiFe]-H_2ase model complex that was able to activate O_2 at the Fe center.[20,21] The complex features a Ni^{II} bound in a square planar environment by two nitrogen donors and two sulfur donors that also bridge to an Fe^{II} with a pentamethylcyclopentadiene (Cp*) ring and bound acetonitrile solvent molecule. The mechanism is summarized in **Figure 3**. Molecular oxygen (O_2) molecule binds after removal of the solvent and oxidized the Fe^{II} to a Fe^{IV} while itself being reduced to a peroxo

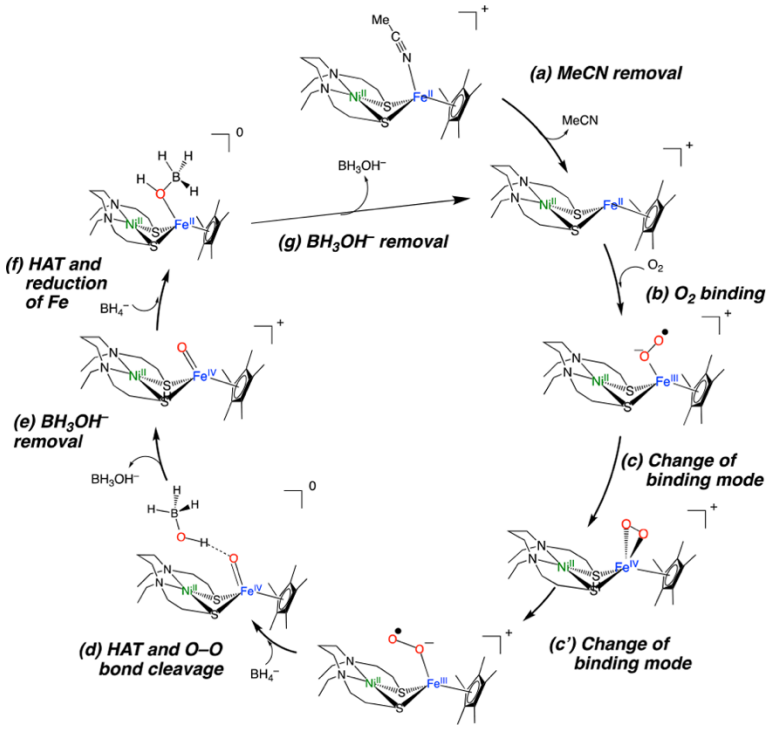

Figure 3 Mechanism of O_2 activation by model complex. Reprinted with permission from "DFT Study on Fe(IV)-Peroxo Formation and H Atom Transfer Triggered O_2 Activation by NiFe Complex" *Organometallics* 2018, *37* (10), 1534–1545. Copyright 2018 American Chemical Society.

ligand by way of a superoxide intermediate. The peroxide is removed by a pair of sequential hydrogen atom transfer steps by a sacrificial borane to regenerate the Fe^{II} center. This study shows a possible route for O_2 oxidation by a [NiFe]-H_2ase model

complex but the reactivity is centered at the Fe which not the case with the natural enzymes where the oxidative damage occurs at the Ni^{II}.

The previous mechanistic study shows how DFT can work to supplement experimental data and observations by providing more detailed information about a system. Establishing a reasonable set of expectations for the experiment is important for guiding the DFT calculations. These can come from well understood chemical principles like the $18e^-$ rule for organometallic complexes or the known preferred geometries for metal centers in a ligand field or from what is known about the enzyme the model compound is inspired from. These expectations guide what intermediates or transition states are reasonable to investigate for the catalytic cycle. The major drawback of current DFT methods on these types of systems is an inability to properly account for the many subtle factors that contribute to enzyme function including secondary sphere effects, participation from explicit solvent molecules, or gas channels that direct small molecules to specific reactive sites. These types of effects may be why the DFT calculated mechanism supports O_2 reacting at the iron center instead of the nickel as it does in the enzyme. Understanding the electronic and structural factors that enable the replication of the reactivity of O_2 within the [NiFe]-H_2ase active site is one of our goals.

CHAPTER II

ELECTRONIC STRUCTURE AND PROPERTIES OF SULFUR AND SELENEIUM VARIENTS OF A O_2 DAMAGED [NIFE]-HYDROGENASE MODEL[*]

2.1 Introduction

Hydrogenases are metalloenzymes that catalyze reversible H_2 production from protons and electrons. Likely originating in pre-biotic ages and under a reducing atmosphere, the active sites contain iron, nickel and sulfur, along with simple diatomic ligands, CO and CN, in optimal arrangements that produce superb biocatalysts found throughout nature.[22] These structures offer guidance for design of molecular catalysts comprised of earth abundant metals for application in electrolyzers and fuel cells.[23,24] The deleterious effect of O_2 comprises a major challenge in technological development of molecular catalysts for H^+ reduction based on abundant transition metals, needed for sustainable electron conversion to H_2.[25,26] Oxygen as a poison is also well known to the organisms dependent on Hydrogenase enzymes for H_2 production for its use as an energy vector in many biological pathways.[27] While the protein superstructures largely protect the biological redox centers from O_2 as an oxidant that competes with protons, there is ample evidence, including protein crystal structures, of the detrimental effects of O_2 invasion into the active site. The initial understanding of the [NiFeS]-H_2ase was plagued

---

[*]Part of the data in this chapter is reprinted and adapted with permission from "Oxygen uptake in complexes related to [NiFeS]- and [NiFeSe]-hydrogenase active sites" by Yang, X.; Elrod, L.; Reibenspies, J.; Hall, M.; Darensbourg, M., 2018. Chemical Science, 10, 1368-1373, Copyright The Royal Society of Chemistry 2018 and "Controlling O_2 Reactivity in Synthetic Analogues of [NiFeS]- and [NiFeSe]-Hydrogenase Active Sites by Yang, X.; Elrod, L.; Le, T.; Vega, V.; Naumann, H.; Rezenom, Y.; Reibenspies, J.; Hall, M.; Darensbourg, M., 2019. Journal of the American Chemical Society, 141, 15338-15347, Copyright American Chemical Society.

with Ni-based electron paramagnetic resonance (EPR) signals from various enzyme states damaged by partial oxidation or oxygenation that resulted in different levels of deactivation of the biocatalyst; vague terms such as “ready” and “unready” states, with recovery from oxygen damage on the order of seconds vs. hours, respectively, were adopted in attempts to express reductive (added H_2 or $H^+ + e^-$) reactivation requirements.[27,28]

At least three natural strategies have emerged to protect [NiFe]-H_2ases’ active sites from oxygen exposure: (i) a narrow hydrophobic gas channel that hinders diffusion of the bulkier O_2 into the protein-enclosed active site;[29,30] (ii) the presence of an unusual [4Fe-3S] iron-sulfur cluster subunit located at the proximal cluster of the O_2-tolerant membrane-bound [NiFe]- H_2ase such as that of Membrane-bound respiratory [NiFe]-hydrogenase (MBH) from the hyperthermophilic bacterium *Aquifex aeolicus* and *Ralstonia eutropha*, which provides “an electron-rich environment for O_2 detoxification”;[22,31–35] and (iii) the change of a terminal cysteine into selenocysteine in the O_2-resistant [NiFe]-H_2ase subclass, the [NiFeSe]-H_2ases.[28] This [NiFeSe]-H_2ase subclass is identical to the [NiFeS]-H_2ase except a terminal cysteine is replaced by selenocysteine. As the incorporation of selenocysteine requires an intricate dedicated biosynthetic machinery, as well as a high energetic cost, this form is found in few microorganisms; an example is *Methanococcus Voltae*.[36,37]

Known to be superior to the all-sulfur analogue, the [NiFeSe]-H_2ase subfamily shows higher activity in HER; reduced inhibition by the product H_2; and, when damaged by adventitious O_2, a more rapid recovery.[38–40] The last feature is likely the greatest contributor to its reputation for O_2 tolerance. The overall protein as well as the active sites of [NiFeS]- and [NiFeSe]-H_2ase are structurally analogous. In the same position as a terminal cysteine sulfur in the former that acts as a proton shuttle to the hydride-loaded NiFe unit, the selenocysteine appears to be poised for the same function in [NiFeSe]-H_2ase.[41] Although SeR^- is a poorer Brønsted-Lowry base than SR^-, and expected to be less prone to proton binding, its larger size renders it a better proton shuttle or directing agent, as it both attracts and releases protons.[28,37] Nevertheless, its incorporation into synthetic molecular catalysts for proton reduction has been thus far limited.[40,42–44]

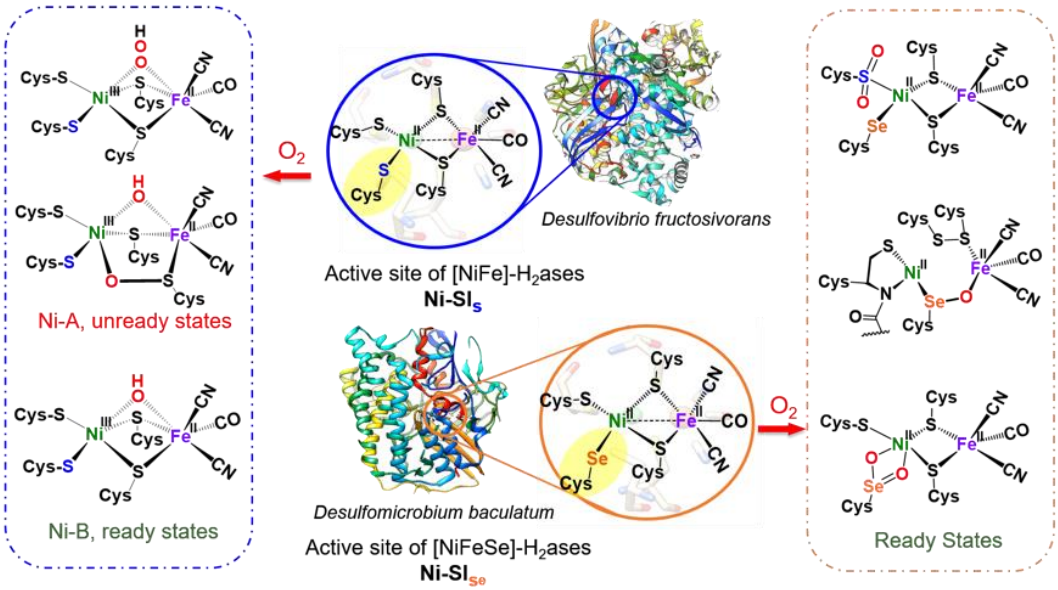

Figure 4 Reduced (middle) active sites of [NiFe]-H_2ases and selected oxidized active sites of [NiFeS]- (left) and [NiFeSe]-H_2ases (right). Reprinted with permission from (Yang, 2018).

Upon exposure of a [NiFeS]-H_2ase to O_2, the active site deactivates to the so-called "Ni-A" (unready) and "Ni-B" (ready) states.[22] The more O_2-tolerant [NiFeS]-H_2ases prefer to form "Ni-B" displayed as a bridging hydroxo ligand between Ni(III) and Fe(II), **Figure 4**.[45] When electron and protons from the normal reductive processes are pumped into this ready state, the oxygen is quickly removed ($t < 1$ min) as water (H_2O) and catalytic activity is recovered.[26,46–49] However, the "Ni-A" state, with a possible hydroxo bridge between Ni(III) and Fe (II) as well as a bridging sulfenate, requires longer times ($t > 1$ h) to be reactivated, **Figure 4**.[50] Several structures of these oxygenates have been determined by crystallography, and signals of their presence have long been known from EPR studies which identified Ni(III) as the redox level in these off-cycle species.[51,52] Studies by Lenz and Zebger, et al., show that the conversion of Ni-A to Ni-B in soluble NAD^+-reducing [NiFe]-H_2ase could proceed via oxygenation of the bridging sulfur in Ni-B, whose active site is a structure similar to another unready state found by Fontecilla-Camps.[53,54] It should be pointed out that some 15 to 20 structures with varying degrees of oxygenation at metal or chalcogen in [NiFeS]- and [NiFeSe]-H_2ases active sites are found in the protein data bank (PDB) to date. We selected a subset of these to describe in **Figure 4**. Undoubtedly, there will be more in the future.[22,45,51,52]

In contrast to the [NiFeS]-H_2ase, oxygen-damage of [NiFeSe]-H_2ase results in various O-uptake levels, none of which feature paramagnetic Ni(III). However, selenium and/or sulfur are found oxygenated or oxidized as dichalcogenides in the structures.[55,56] Such oxygenation products of [NiFeSe]-H_2ase, as well as of [NiFeS]-H_2ase active sites, can be interpreted as a protective maneuver avoiding further metal oxidation and

degradation of the Ni-Fe core structures in each.[43,44] Reductive repair processes return the enzymes' function in both cases.[57]

Recent reports from Pereira, et al., have provided key experiments that constrain the differences in activity of [NiFeSe]- and [NiFeS]-H_2ases to selenium itself rather than any structure changes in the protein.[58] Thus the simplest explanations for the greater hydrogenase activity and easier reactivation of oxygen-degraded [NiFeSe]-H_2ase as contrasted to the all-sulfur analogue lie in the greater polarizability of selenium, and the weaker Se-O bonds as contrasted to S-O.[37] As such soft descriptions are difficult to quantify we have pursued relevant structure/function analyses in well-characterized heterobimetallic synthetic analogues containing S and Se.

As these oxygenated chalcogenides play vital roles in the reversibility of oxygen damage, small molecule analogues are needed to explore aerobic damage and repair, both for insight into the biomechanistic properties of the enzyme as well as the design of robust

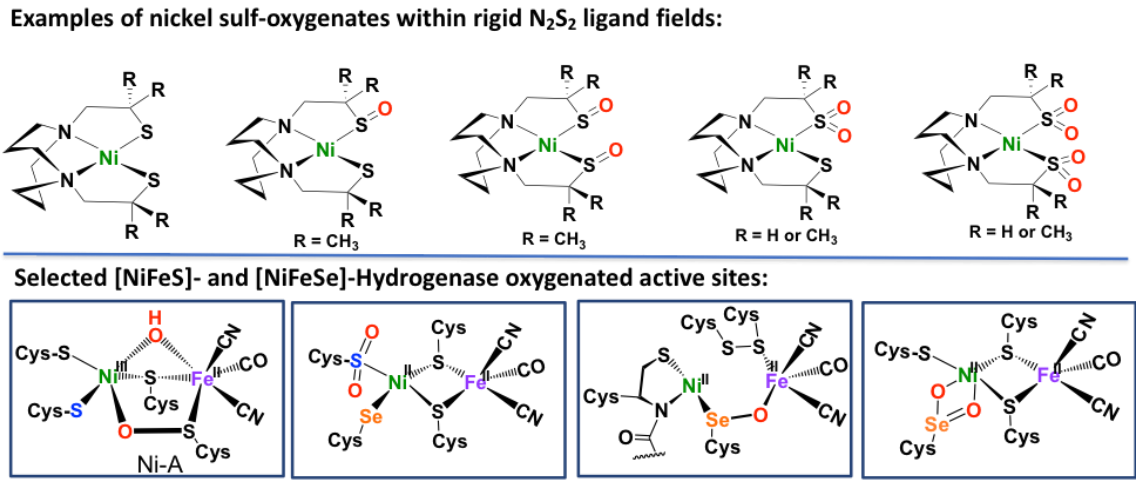

Figure 5 Selected S-oxygenated thiolates in monomeric nickel complexes, and examples from crystallography of oxygen-damaged [NiFe]-H_2ase active sites. Reprinted with permission from (Yang, 2019).

synthetic catalysts. Ogo, *et al.* isolated a high valent iron(IV) peroxo complex on reacting solvent-coordinated complexes $[Ni^{II}LFe^{II}(RCN)(\eta^5\text{-}C_5Me_5)]^+$ with O_2.[20,21,59] However, no oxygenated sulfur species were reported from their system. The first S-oxygenated [NiFe] complex was reported by Driess's lab as a model for sulfenate intermediates in O_2-tolerant hydrogenase; it was synthesized from $FeBr_2$ and the pre-formed sulfenato nickel complex rather than direct oxygenation.[60,61] Examples of S-oxygenated thiolates are plentiful in monomeric complexes containing nickel bound within a rigid tetradentate N_2S_2 ligand field; several examples are displayed in **Figure 5**.[60,62–66]

The synthesis of nickel-iron bimetallic complexes containing both sulfur and selenium, thus providing faithful synthetic analogues of the active sites of [NiFeS]- and [NiFeSe]-H_2ases, represents a considerable challenge.[8,32,49] My labmate/coworker, Xuemei Yang (now Dr. Yang) expanded a strategy found to be successful in the preparation of synthetic analogues of the nickel superoxide dismutase,[68] and to address other questions in the bioinorganic chemistry of nickel: this strategy is the splitting of dimeric $[NiN_2S]_2^{2+}$ by exogeneous thiolates.[55,68,69]

Dr. Yang's synthesized models served as inspiration for theoretical calculations into the electronic structure and the bonding interactions of the complexes. Density functional theory has established itself as the backbone of theoretical chemistry investigations due to its combination of generally high accuracy and low computational cost.[70,71] The accuracy and cost of DFT functionals generally increase with progress up on the 'Jacob's Ladder' hierarchy first established by John Perdew, **Figure 6**.[72] This places Hartree-Fock (HF) with its lack of correlation energy at the bottom and true chemical

accuracy at the top with DFT functionals in between grouped by what components they contain. When determining what functional to use for a problem, researchers traditionally must balance the accuracy typically gained by more complex functionals with the increased resources required to use them. Some of the recently developed functionals that fall into the upper rungs of the ladder tend to be highly parameterized and designed with a particular application in mind. This potentially limits their use in broader applications and requires careful benchmarking by researchers wanting to use these functionals expecting them to give more accurate results.

We examine here a part of the periodic table that has been excluded in the benchmarking data sets to date, heavier main group elements, leading to questions about

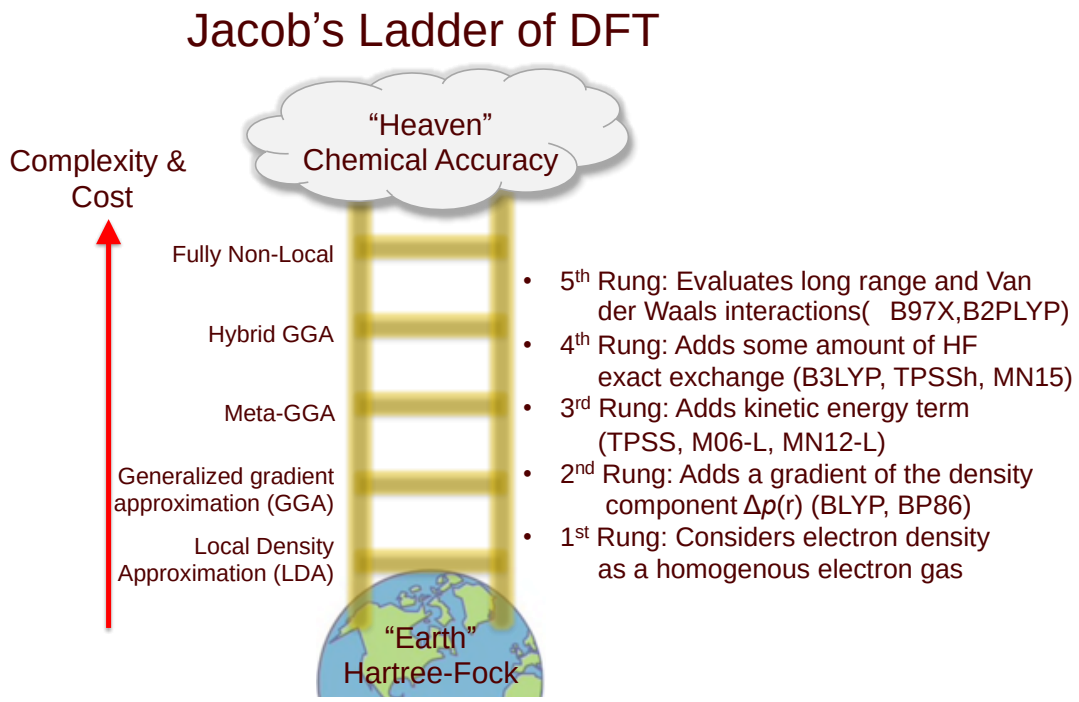

Figure 6 Jacob's Ladder of DFT detailing the hierarchy of DFT functionals.

what functional would handle systems containing these elements the best. Our aim is to use sets of benchmarking reactions with small molecules containing oxygen, sulfur, and selenium to focus on how each functional describes the properties of the chalcogen bonds in order to determine the functional that will best describe the full **Ni**(μ-E_{Ph})(μ-S'_{N2})**Fe** models.

2.2 Synthesis and characterization of [NiFeS]- and [NiFeSe]-H_2ases models

Nickel dithiolate complexes such as NiN_2S_2 are well known to react as metalloligands by formation of Ni-(μ_2-SR)$_2$-M' bridges.[73] Adopting a $[NiN_2S]_2^{2+}$ bimetallic nickel dimer as a platform for dimer cleavage reactions, my coworker, Dr. Yang, prepared and isolated monomeric Ni(N_2S)(EPh) (E = S and Se, complexes A and B

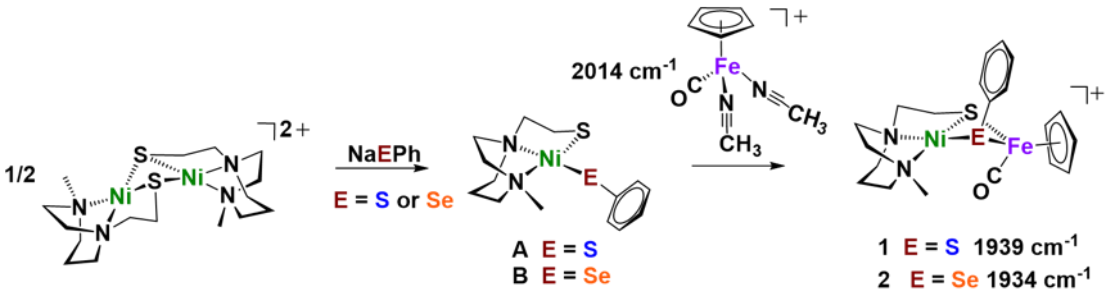

Figure 7 Synthetic scheme for $NiE_{Ph}Fe^+$ complexes 1 and 2. The *ν*(CO) IR values of the products recorded in CH_2Cl_2. Reprinted with permission from (Yang, 2018).

respectively in **Figure 7**).[68,73–75] These *cis*-dichalcogenides are subsequently used as metalloligands to an iron receiver unit, $(\eta^5\text{-}C_5H_5)Fe^{II}(CO)^+$, in analogy to well-known NiN_2S_2 derivatives.[19] The lower value of ν(CO) (1934 cm^{-1}) in the $NiSe_{Ph}Fe^+$, complex **2,** (1939 cm^{-1}) as contrasted to $NiS_{Ph}Fe^+$, complex **1**, is attributed to the better electron donor properties of Se over S,[37] resulting in better π-backbonding from Fe^{II} to the CO reporter ligand, **Figure 7**.

Molecular structures determined by X-ray diffraction (XRD) are unexceptional but provide a valuable starting point and reference for the DFT calculations, **Figure 8**. Further modifications to these complexes were made by exploiting the fact that dimeric $[NiN_2S]_2^{2+}$

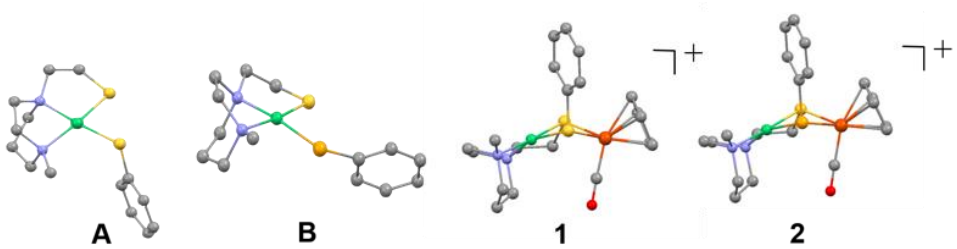

	A	B	1	2
Ni···Fe/Å	-	-	3.170	3.253
Ni-E_{Ar}/Å	2.184(3)	2.309(6)	2.199(1)	2.311(1)
Fe-E_{Ar}/Å	-	-	2.300(2)	2.406(1)
∠Fe-E_{Ar}-Ni/°	-	-	89.57(5)	87.17(4)
∠S-Fe-E_{Ar}/°	-	-	79.40(5)	79.62(5)
∠S-Ni-E_{Ar}/°	88.4(3)	94.19(3)	84.71(5)	84.47(6)
∠E_{Ar}-Ni-N	100.3(3)	93.94(8)	101.1(1)	101.4(2)
E_{Ar}-C_{Ph}	1.754(6)	1.918(3)	1.789(5)	1.931(6)
Hinge angle/°	-	-	141.15	142.69

Figure 8 Molecular structures of A, B and 1 ($NiS_{Ph}Fe$), 2 ($NiSe_{Ph}Fe$), determined by single-crystal XRD, with the BF_4^- ions and hydrogen atoms omitted for clarity. E in A and 1 is sulfur; E in B and 2 is selenium. Reprinted with permission from (Yang, 2018).

complexes are readily cleaved by various nucleophiles, including aryl chalcogenides, E_{PhH}^-, E = S and Se.[67,68] Unlike the stable S-oxygenates described in **Figure 5**, the

resulting monomeric **Ni**(E_{PhX})(S'_{N2}) complexes are air-sensitive resulting in degradation. Nevertheless, when combined with $(\eta^5\text{-}C_5H_5)Fe^{II}(CO)(CH_3CN)_2^+$, displacing the CH_3CN labile ligands, the resultant Ni-Fe complexes provide examples of stable products of O_2 uptake, **Figure 9**. The X substituents on the aryl ring do not substantially modify the

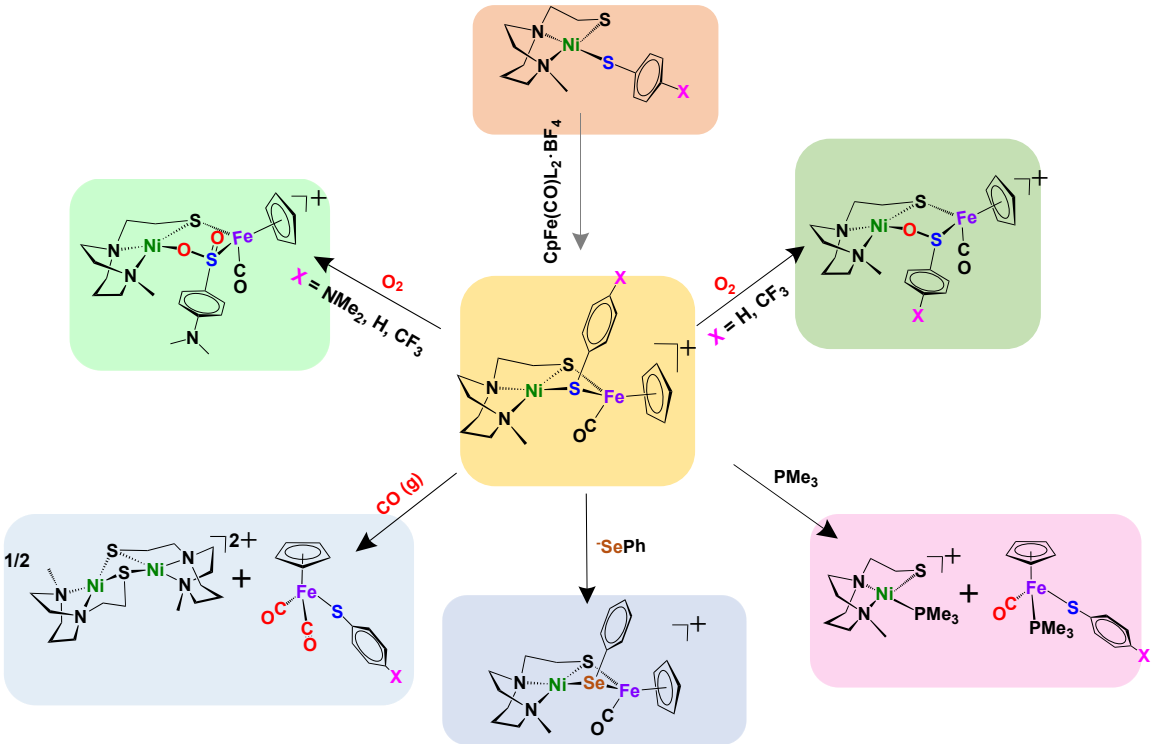

Figure 9 Synthesis of NiFe complexes containing para-substituted arylthiolates and various reactions. L in the $CpFe(CO)L_2^+$ synthon, 12 o'clock arrow position, is CH_3CN as labile ligand. Reprinted with permission from (Yang; 2019).

structures for any of the complexes that have been isolated and studied by XRD, **Figure 10**. While these models are imperfect structural analogues of the oxidized enzymes, these NiFe small molecules offer a paradigm for contrasting S and Se in relevant O_2-addition and repair processes. Moreover, the arylchalcogenides are susceptible to modifications by para-substituents on the arene,[44] giving clues regarding electronic effects operative on oxygen uptake and product distribution. A summary of the reactions explored by my

coworker Dr. Yang is found in **Figure 9**.[67,76] The two species highlighted in green boxes, their selenium containing analogs, and the aryl substituted variants constitute the primary focus of the computational work on this project.

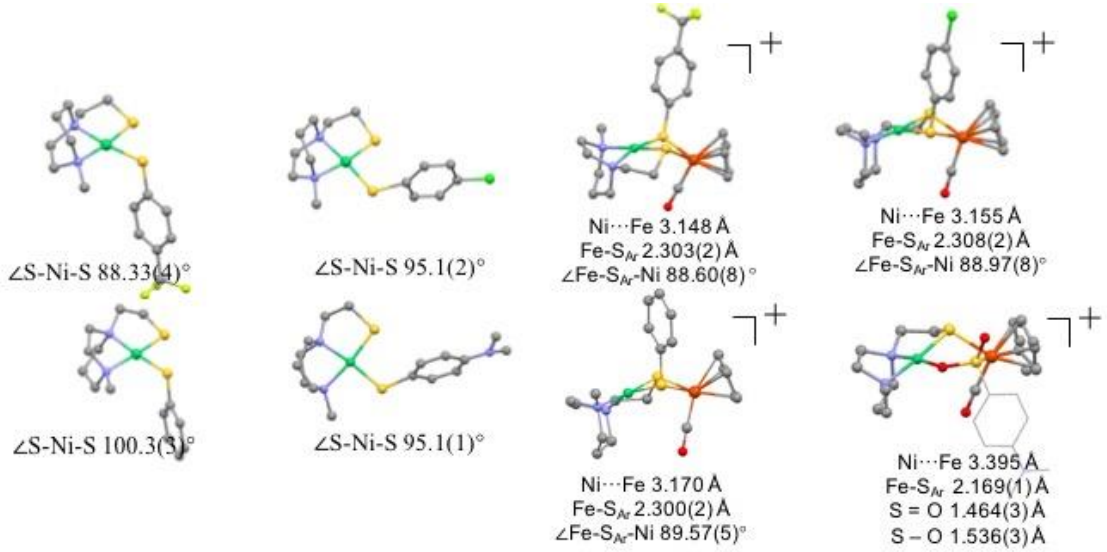

Figure 10 Molecular XRD structures determined for monomeric Ni and for the **Ni**(μ-S_{PhX})(μ-S'_{N2})**Fe** complexes. Reprinted with permission from (Yang, 2019).

Correlations of the Hammett σ_p parameter with ν(CO) IR values and $Ni^{II/I}$ reduction potentials derived from cyclic voltammetry, for the series of NiFe complexes are presented as plots in **Figure 11**.[77] Both theoretical (DFT-derived) and experimental values of the ν(CO) in **Ni**(μ-S_{PhX})(μ-S'_{N2})**Fe** and $E_{cathode}$ potentials for Ni^{II}/Ni^{I} in monomeric **Ni**(S_{PhX})(μ-S'_{N2}) complexes correlate well with the Hammett parameters of the X substituents on the $^{-}S_{PhX}$ ligands. Specifically, more electron-donating substituents result in lower ν(CO) values, illustrating electronic communication over 5 bonds and the influence on π-backbonding from Fe^{II} to the CO. The **Ni**(μ-Se_{PhX})(μ-S'_{N2})**Fe** series shows ν(CO) responses to X similar to the sulfur analogues, however moderated in value. Interestingly, the phenyl derivative with the most electron-donating substituent, **Ni**(μ-

S_{PhNMe2})(μ-S'_{N2})**Fe**, gives the same ν(CO) value (1934 cm^{-1}) as found in **Ni**(μ-Se_{PhH})(μ-S'_{N2})**Fe**. There is not such a match in the $Ni^{II/I}$ reduction potential.

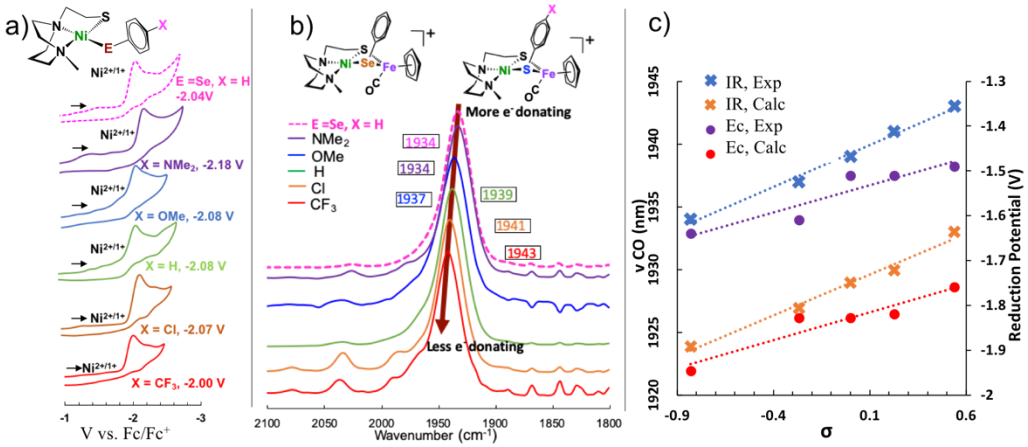

Figure 11) Cyclic voltammograms in E_c region for Ni^{II}/Ni^{I} and monomeric Ni complexes; b) The ν(CO) IR spectra of **Ni**(μ-E_{PhX})(μ-S'_{N2})**Fe**; c) Correlations of Hammett σ parameters with experimental and calculated ν(CO) values and E_c values of Ni^{II}/Ni^{I}. Reprinted with permission from (Yang, 2019).

2.3 Reactivity

The results of the reactions of complexes **1** and **2** with oxygen are summarized **in Figure 12**. Both **1+O** and **2+O** were detected by Fourier transform infrared (FTIR hereafter abbreviated as IR) spectroscopy but only **2+O** was able to be structurally

characterized by XRD, **Figure 13**. The reactivity difference (i.e., the reaction time) is consistent with the fact that S^{2-} is oxidized with more difficulty than Se^{2-}.[37] Based on DFT calculations (*vide infra*), complex **1+O** is of a similar structure as **2+O**. Both oxygenated

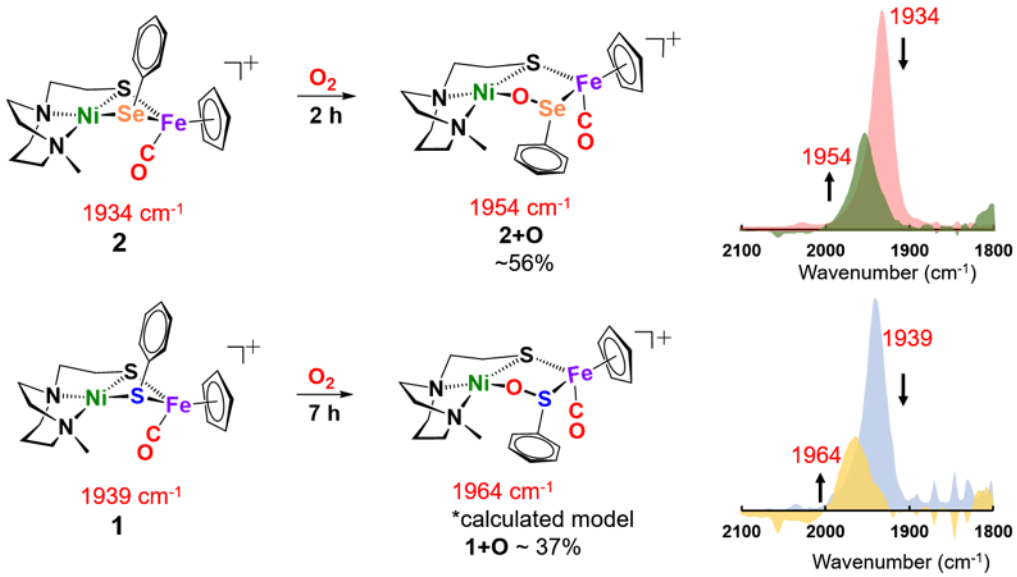

Figure 12 Reactions of 1 and 2 with 1 atmosphere O_2; conversions determined by *ν*(CO) analysis. Reprinted with permission from (Yang; 2018).

complexes show sharp signals in the nuclear magnetic resonance (NMR) spectra and are EPR-silent, indicating that the oxidation states of Ni and Fe are low spin +2 species. As seen in the overlays in **Figure 13**, the DFT optimized structures of **2** and **2+O** have excellent agreement with the XRD structure. Complex **2+O** is, to our knowledge, the first model of an oxidized [NiFeSe]-H_2ase synthetic analogue.

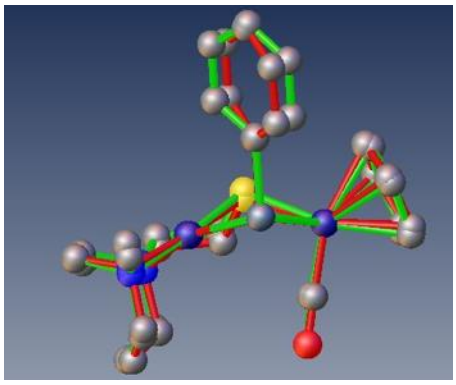

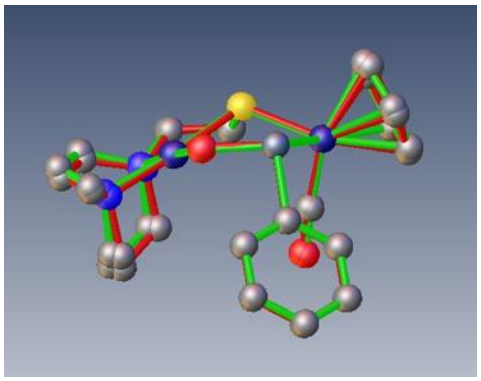

	2 Exp.	**2** Calc.		**2+O** Exp.	**2+O** Calc.
Ni- - -Fe/Å	3.253	3.23	Ni-Fe/Å	3.568	3.615
Ni-Se/Å	2.3110(11)	2.3383	Ni-Se/Å	3.168	3.209
Fe-Se/Å	2.4059(12)	2.4388	Ni-S/Å	2.1528(8)	2.1754
Ni-Se-Fe/°	87.17(4)	85.15	Ni-O/Å	1.870(2)	1.869
Hinge/°	142.69	136.77	Fe-S/Å	2.2484(9)	2.2795
			Fe-Se/Å	2.3326(6)	2.3355
			O-Ni-S/°	92.93(7)	93.05
			Se-Fe-S/°	86.15(3)	86.22

Figure 13 Overlay of experimental and computational structures of 2 and 2+O along with selected geometric parameters. Hydrogens deleted for clarity. Reprinted with permission from (Yang; 2018).

As a comparison to the $NiE_{Ph}Fe$ complexes **1** and **2**, constrained NiN_2S_2 derivatives, $[NiN_2S_2{\cdot}Fe(\eta^5\text{-}C_5H_5)(CO)]^+[BF_4]^-$ and $[NiN_2S_2{\cdot}Fe(\eta^5\text{-}C_5Me_5)CO)]^+[BF_4]^-$ (N_2S_2 = bismercaptoethanediazacycloheptane) were tested for reactivity with oxygen.[78,79] After stirring their solutions in an O_2 atmosphere for several days, they remain intact with no indication of reaction. We surmise that the CO which is bound to Fe prevents O_2 activation at the Fe center and both sulfur and nickel are deactivated towards O_2 reactivity in the rigid chelating N_2S_2 ligands. However, in complexes **1** and **2**, the mobility at EPh (E = S or Se) provides a potential site for O_2 attack on the Ni or Fe. The strength of the metal-chalcogen bonds in the tetradentate analog of **2** and the importance of the aryl chalcogenate in relation to oxygen reactivity is further explored below, **Figure 16.**

As arbiters between O_2 and the [NiFe] or [NiFeSe]-H_2ase active sites, chalcogenides prevent complete degradation of the organometallic active sites of hydrogenases, and perform this role reversibly.[26,54] To explore the possibility of reversal

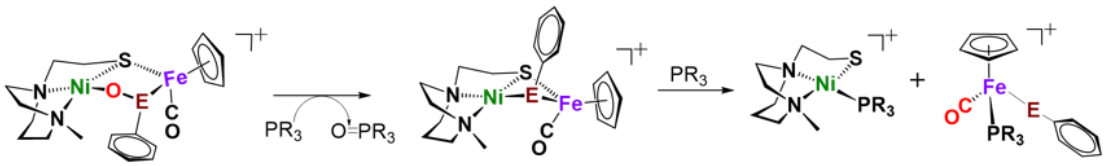

Figure 14 Reaction of complex 2+O (E = Se) or 1+O (E = S) with O-abstracting agents, PR_3 (R = Me or o-tolyl). Reprinted with permission from (Yang, 2018).

of oxygenated selenate/sulfenate, O-abstracting agent PMe_3 was employed for O-atom removal, **Figure 14**. The results showed that both **1+O** and **2+O** could be converted back into their respective reduced forms, **1** and **2**. The conversion for **2+O** proceeded cleanly with 1 equivalent of PMe_3 but only partial conversion was achieved for **1+O**. The reduction of **1+2O** does not occur even with excess PMe_3. These results are corroborated by electrochemical reduction using Cp_2Co as an electron source and HBF_4 as a proton source, **Figure 15**. These results support the hypothesis that nature invests in the

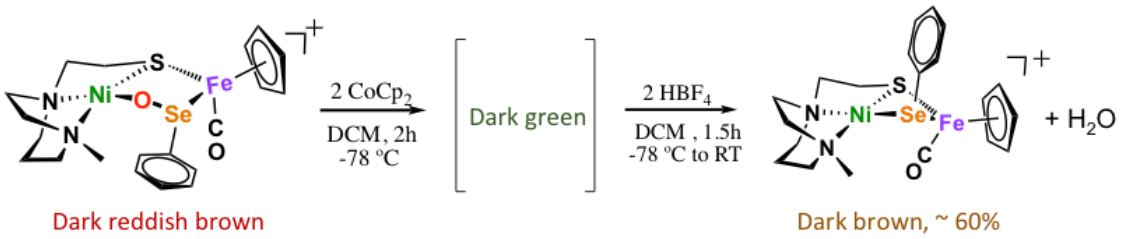

Figure 15 Oxygen removal reaction using Cp_2Co as reductant and HBF_4. Reprinted with permission from (Yang, 2019).

energetically expensive replacement of cysteine with selenocysteine in the [NiFe]-H_2ase active site in order to provide a more facile path towards repair after damage due to oxygen exposure.

2.4 Computational results

The structure of **2+O** was investigated to determine contributing factors to the thermodynamically favored oxygenation product. A less rigid model of **2+O** was made by breaking the carbon-carbon bond linking the sulfur donor to the neighboring nitrogen donor, changing the resulting methylene fragments into methyl groups. For computational economy the phenyl group on Se-Ph was replaced by with a methyl group. This bidentate $N_2S_{Me}Se_{Me}$ model, with unconnected SMe, is designated as **3** and is designed to create similar bonding around the sulfur and selenium atoms. Another model, labeled as **4,** connected the Se_{Ph} to the N_2S backbone creating a more rigid structure more analogous to previously reported ligands.[73]

Four oxygenated isomers, **2+O$_{a-d}$,** as well as four corresponding isomers for both the bidentate and tetradentate forms, **3+O$_{a-d}$** and **4+O$_{a-d}$,** were calculated in which the location of the oxygen atom was varied according to the scheme described in **Figure 16**. The isomer **2+O$_a$**, which corresponds to the experimental structure, is indeed the lowest energy isomer of **2+O**; the next lowest isomer, **2+O$_b$**, is 8.6 kcals higher in energy. This contrasts with the $N_2S_{Me}Se_{Me}$ model in which the lowest energy isomer, **3$_d$**, has the oxygen atom inserted between the nickel and the sulfur atoms rather than the nickel and selenium. The corresponding isomer **2+O$_d$** is the highest energy isomer for the tridentate model and the oxygen atom appears in a position bridging the nickel sulfur bond rather than full insertion. This is likely due to the geometric restraints imposed by the tridentate N_2S ligand that disfavor the addition of the oxygen atom into its rigid binding arrangement.

This constraint is not found in the more open bidentate model with separated S_{Me} donors. There it is found that formation of a sulfur-oxygen bond is thermodynamically favored, by 3.2 kcal/mol, as compared to the formation of a selenium-oxygen bond. In the more

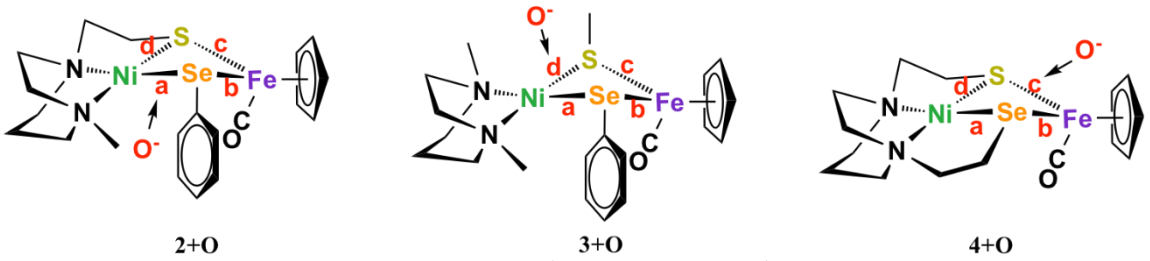

	a	b	c	d
2+O	0	8.6	10	15.5
3+O	3.2	10	14.2	0
4+O	n/a	0.5	0	8.3

ΔG° (kcal/mol)

Figure 16 Relative energies of oxygenated isomers of N_2SSe_{Ph} model, 1+O, the bidentate, separated donors in the $N_2S_{Me}Se_{Me}$ model, 1, and the tetradentate donors in the N_2SSe model in kcal/mol. Reprinted with permission from (Yang, 2018).

constrained tetradentate model, the lowest energy isomer is $\mathbf{4_c}$ with $\mathbf{4_b}$ only being 0.5 kcal/mol higher in energy. The $\mathbf{4_a}$ isomer, corresponding to the lowest energy isomer for **2**+O was not found computationally. All attempts at geometrical optimization resulted in the oxygen atom inserting into the selenium-carbon bond to form a Ni-Se-O-$(CH_2)_2$-N six-membered ring preserving the nickel-selenium bond. The last isomer, $\mathbf{4_d}$, is 8.3 kcal/mol higher in energy than the lowest energy isomer. This structure features the oxygen in a position above the nickel-sulfur bond due to the rigidity of the N_2S_2 background.

The computational methods yielded the structures and energies of the **Ni**(μ-S_{PhX})(μ-S'_{N2})**Fe** complexes as well as their singly and doubly oxygenated forms. These calculations aimed to examine how the properties of the model complexes depended on

the chalcogen identity, sulfur vs. selenium, and with para substituents, X, that modified the electron-donating properties of the E-PhX. Our computational method accurately reproduces the trends seen in the experimental data for structures (where available), the trends in *ν*(CO) IR values (absolute values are underestimated), and the positions of $Ni^{II/I}$ reduction potentials, **Figure 10**.

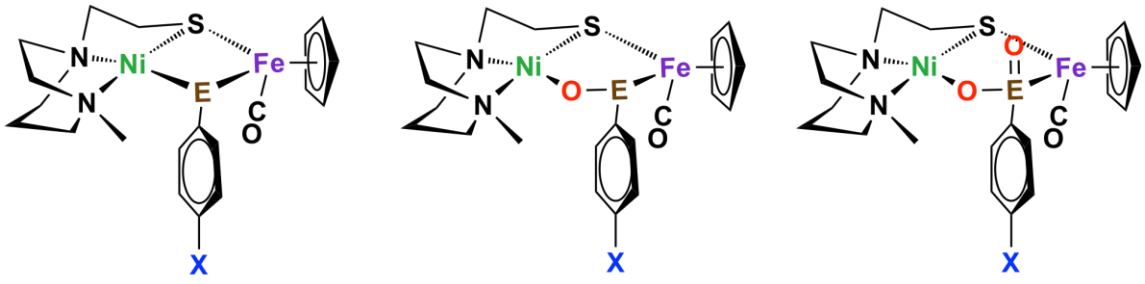

	A	B	C
E=S, X=NMe2	1895 (1934)	1921	1924 (1960)
E=S, X=OMe	1898 (1937)	1923	1928
E=S, X=H	1900 (1939)	1924 (1964)	1931
E=S, X=Cl	1901 (1941)	1926	1933
E=S, X=CF3	1904 (1943)	1927	1934
E=Se, X=NMe2	1890 (1929)	1914 (1950)	1930
E=Se, X=H	1895 (1934)	1919 (1954)	1936
E=Se, X=CF3	1897 (1936)	1920 (1959)	1937

Figure 17 DFT calculated *ν*(CO) values for $NiE_{PhX}FeO_n$ complexes with n= 0, 1, or 2. Experimental values where available are in parenthesis.

As mentioned above, the **Ni**(μ-E_{PhX})(μ-S'_{N2})**Fe** complexes with E = Se, X = H and with E = S, X = NMe_2 display the same *ν*(CO) values in experiment (1934 cm^{-1}) and from theory (1895 cm^{-1}). These equivalent values indicate that, as relayed by iron to the carbon monoxide ligand, the $^{-}Se_{PhH}$ and the $^{-}S_{PhNMe2}$ are equally strong electron donors. Similarly, the calculated *ν*(CO) stretch for the singly oxygenated **Ni**(μ-O-μ-Se_{Ph})(μ-S'_{N2})**Fe** (1919 cm^{-1}) is comparable to that of **Ni**(μ-O-S_{PhNMe2})(μ-S'_{N2})**Fe** (1921 cm^{-1}). In contrast with the doubly oxygenated complexes the *ν*(CO) value calculated for the two-oxy species, the

Ni(μ-O-(O=)Se_{PhH})(μ-S'$_{N2}$)**Fe** complex (1936 cm^{-1}) is now most similar to the sulfur analogue with the electron withdrawing X = CF_3, i.e., **Ni**(μ-(μ-O-S(=O)$_{PhCF3}$)(μ-S'$_{N2}$)**Fe**. **Figure 17** contains the calculated *ν*(CO) values for all complexes studied as well as the experimental values where available.

The O-uptake distinctions in the Ni—Fe complexes inspired further DFT computations that addressed thermodynamic driving forces for O_2 reactions and the two types of products. As summarized in **Figure 18,** the free energies, ΔG° , for the sulfur and selenium single oxygenation reactions are found to be similar at -14.3 and -15.6 kcal/mol, respectively. The double oxygenation reactions however show a greater difference; the ΔG° in the selenium case is -25.2 kcal/mol whereas the sulfur case is favored by -35.5 kcal/mol. The selenium 2-oxy species is more stable than the 1-oxy but the energy gap

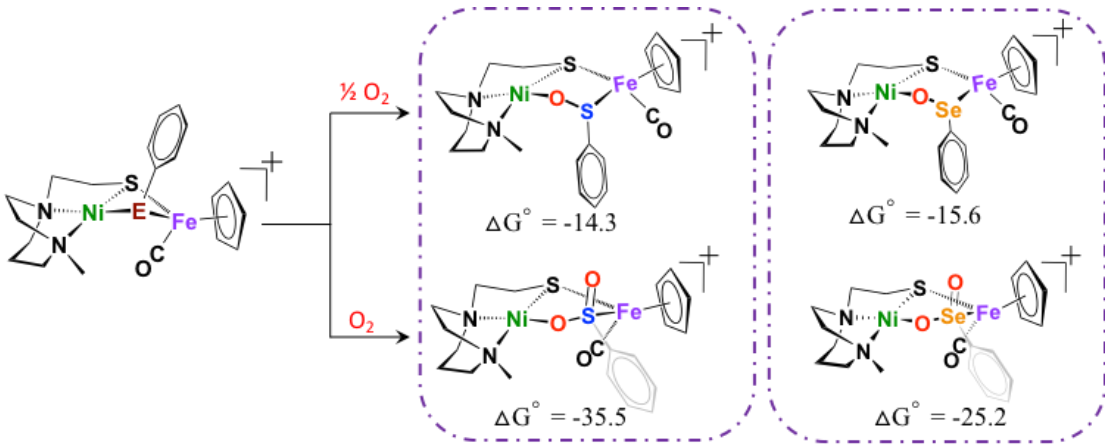

Figure 18 DFT calculated free energy values, ΔG° , for comparison of oxygen-uptake reactions of Ni(μ-E_{PhH})(μ-S'$_{N2}$)Fe complexes, E = S and Se, in kcal/mol. Reprinted with permission from (Yang, 2019).

between the levels (9.6 kcal/mol) is approximately half as large as the energy gap for the sulfur analogues (21.1 kcal/mol). While the reaction energies indicate in both cases the 2-oxy species should be the thermodynamic product, only the sulfur displays the sulfinate.

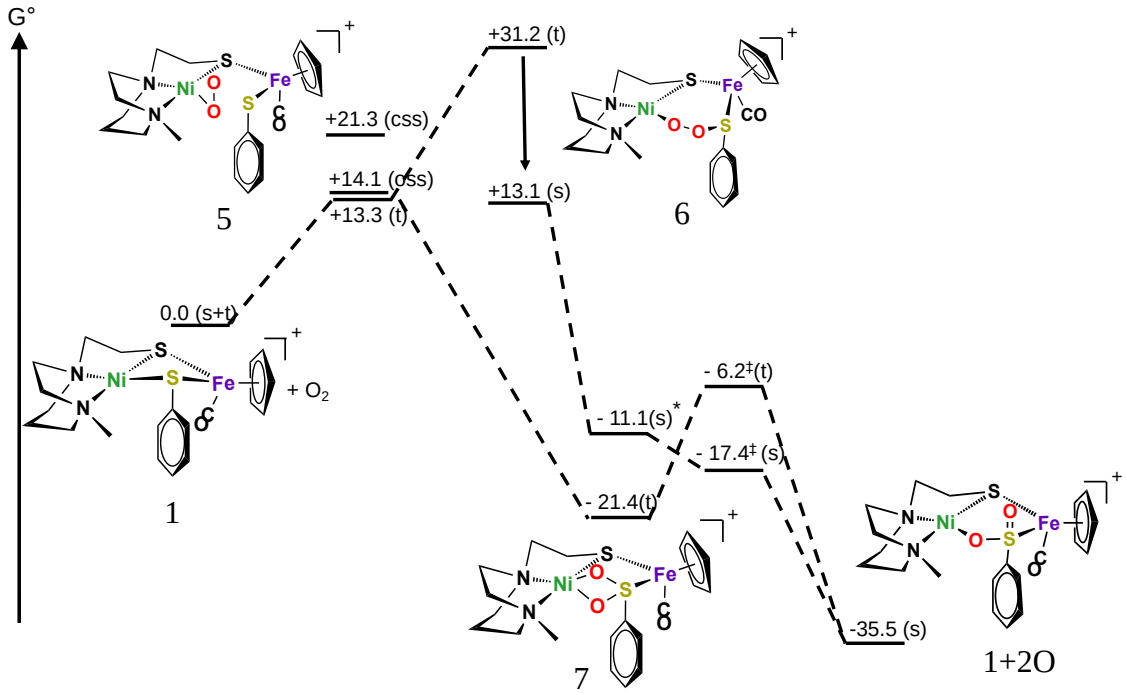

Figure 19 DFT calculated intermediates and transition states for a proposed reaction of Ni(μ-E_{PhH})(μ-S'$_{N2}$)Fe with O_2. Spin state of structures are in parenthesis. Asterisk denotes a non-optimized structure. Double daggers denote transition states. All free energies are in kcal/mol.

Due to the mixture of products upon exposure to oxygen, mechanistic details for oxygenation of the model complexes proved difficult to obtain experimentally, while DFT calculations have provided some insights into possible intermediates, **Figure 19**. Initially, the O_2 molecule inserts into the nickel-sulfur bond of **1** maintaining the square planar geometry around the nickel. This results in an oxidized Ni^{III} and a bound superoxide, **5**. This assignment aligns with the small energy difference between the ground state triplet

and open shell singlet state that is only 0.8 kcal/mol higher in energy. The small difference arises because the nickel and superoxide are bound at a 111° angle creating near orthogonality between the Ni d_{xy} singly occupied molecular orbital (SOMO) and the superoxide π^* SOMO.

There are two plausible paths forward from the superoxide structure depending on what binding mode the complex goes through. The first is to an end-on binding mode where one atom oxygen atom binds the nickel and the other binds the sulfur forming a peroxide bridge, **6**. According to the calculations, going to this binding mode would lead to a spin crossover giving a singlet ground state. This intermediate must then transition into the other binding mode which features the oxygens bound in a side on fashion, **7**. This mode effectively breaks the oxygen-oxygen bond and has each oxygen form a bond to both the sulfur and the nickel. This intermediate can also result directly from the superoxide intermediate and maintain the triplet spin state. A single point calculation finds the singlet state to be 9.7 kcal/mol higher than the triplet. The single point calculation was required instead of a geometry optimization because the transition state for between this intermediate and the final product, **1+2O**, was low enough to create a barrier-less process on the potential energy surface. The triplet form of this intermediate would need to go through a spin crossover event which is likely as the calculated transition state for the triplet is 10.8 kcal/mol higher than the singlet. The difficult nature of pinpointing these spin crossover points has prevented a full mechanistic pathway from being developed. The selenium mechanism has not yet been fully explored but our hypothesis is that because the oxygenated form is less favorable as a final product as compared to the sulfur variant there

will be a divergent path that begins either from the superoxide complex, the peroxide bridged species, or the double μ-O bridged species.

In the absence of a definitive mechanism for the O_2 uptake reaction we suggest possible working hypotheses: (#1) the selenium 2-oxy product is less kinetically accessible than the 1-oxy product; or (#2) the 2-oxy product is formed but the weak terminal Se=O allows the complex to undergo comproportionation with the mixed chalcogenide precursor to form two equivalents of 1-oxy products. This type of reactivity

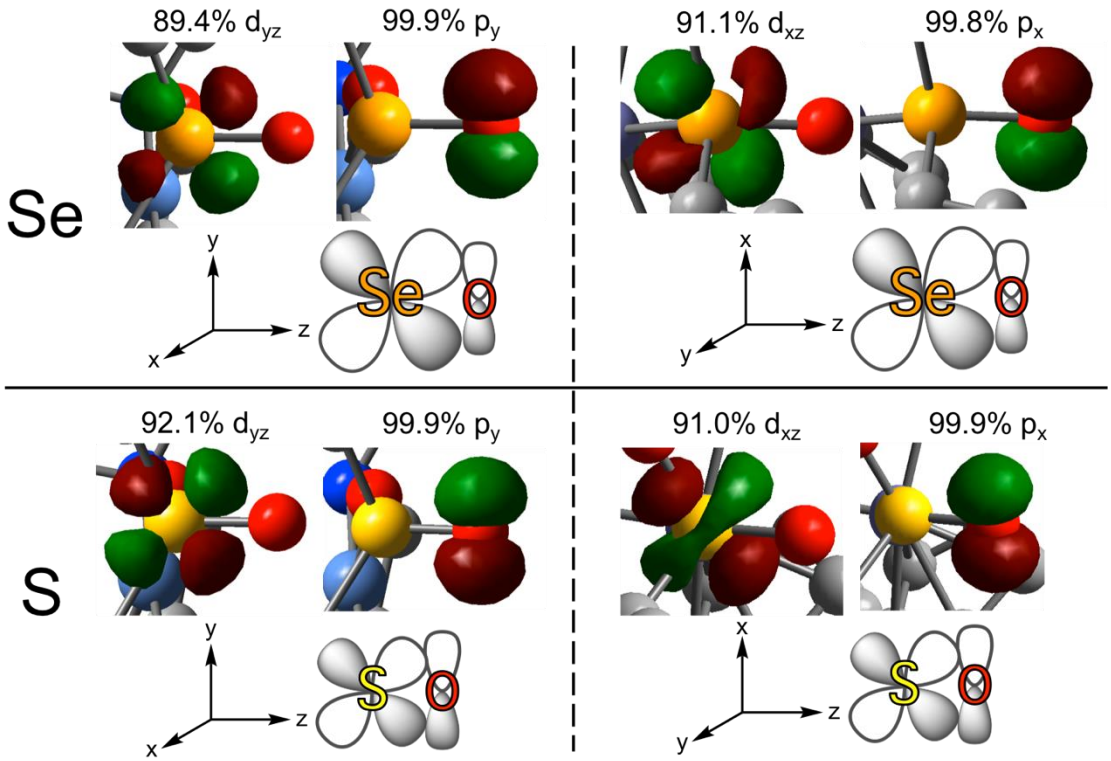

Figure 20 NBO analysis of the sulfur and selenium 2-oxy species highlighting the donor-acceptor orbitals involved in the E=O bond, shown at an isovalue of 0.11. Orbital composition is almost identical for sulfur vs selenium indicating the difference S=O and Se=O pi bond strengths is due to the more contracted nature of the s and p orbitals and the more diffuse nature of the d orbitals for selenium. Reprinted with permission from (Yang, 2019).

has no direct analog in enzymes due to the enclosed nature of the active site but the possibility was explored further computationally *vide infra*.

Reasonable support for hypothesis #2 is that the difference in the ΔG° for the 2-oxy complexes correlates with the strength of the π bond to the terminal oxygen for sulfur vs. selenium. The Natural Bond Orbital (NBO)[80] analysis (second order perturbation), **Figure 20**, reveals the total stabilization energy coming from interactions of the lone pairs on the terminal oxygen with the chalcogen to be 24.4 kcal/mol for the sulfur and 13.0 kcal/mol for the selenium variant. These interactions involve the following orbitals. The electron donating lone pairs on the oxygen atom are found in three natural atomic orbitals (NAOs) with two having almost exclusively p orbital character (>99.8%) and the other being an sp hybrid (>75% s character) in both the sulfur and selenium 2-oxy complexes. The three most significant (>80% of the total stabilization energy) electron accepting orbitals for the sulfur and selenium complexes are two NAOs with primarily d character (>89%) and one pd hybrid orbital (68:31 and 54:42 ratios of p:d character for the sulfur and selenium complexes, respectfully). While the natural atomic orbitals that make up the S=O and Se=O π interaction appear nearly identical, the greater electronegativity difference for Se and the greater orbital size mismatch for Se results in the weaker π bond with the terminal oxygen as compared to sulfur. We believe it is the weakness of this Se=O π that prevents the stable formation of **2+2O**.

To further explore the nature and differences of the S=O and Se=O bonds required a more rigorous approach to the functional benchmarking. This is because while TPSSTPSS worked well to replicate the geometry of the various **Ni**(μ-E_{Ph})(μ-S'_{N2})**Fe**

complexes, one cannot assume it will accurately describe the bonding interactions. Previous work by Liu et al. has shown the sensitivity of sulfur, oxygen, and first row transition metal bonding interactions to DFT functional choice in an [FeFe]-H_2ase model.[81] They saw a range of over 70 kcals/mol in isomer preference when comparing a bridging oxide between the two iron centers or a terminal S=O on the diazo bridge. This large range was attributed to the difference in exact exchange in the over 20 functionals tested.

The determination of the best functional for chalcogen oxygenation reactions was based on overall functional performance across three main test reactions with the small model compounds. These were a) oxygenation of the reduced compounds by O_2 (**Figure 21**), b) comproportionation reaction between the reduced compound and doubly oxygenated form to produce two equivalents of the singly oxygenated form (**Figure 23**), and c) the isomerization reaction that takes the terminal oxygen and inserts it into the sulfur/selenium-hydrogen/carbon bond (**Figure 24**). The values obtained from the CCSD(T) benchmarking calculations were treated as the "true" values and the results from the DFT functionals were based on how closely they

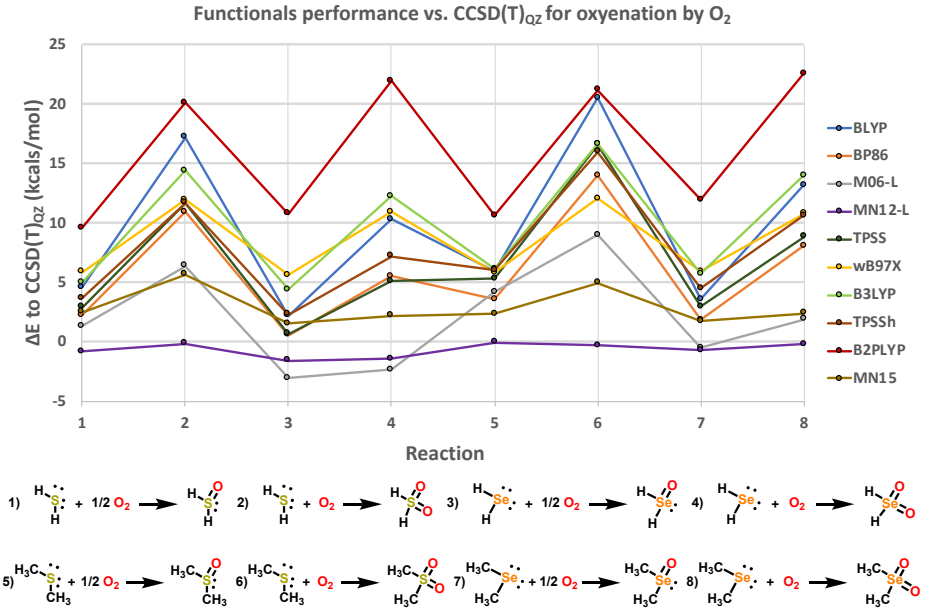

Functional	Total Error (kcals/mol)
CCSD(T)	0
BLYP	77.6
BP86	46.8
M06-L	28.8
MN12-L	5.2
TPSS	54.1
wB97X	69.0
B3LYP	78.6
TPSSh	62.0
B2PLYP	128.8
MN15	23.4

Figure 21 Comparison of DFT functionals performance on the energy of the oxygenation reactions of the chalcogen small model compounds as compared to the CCSD(T) benchmark. The top four performing functionals are highlighted in the table. Total error is defined as the unsigned sum of all errors for each functional across all test reactions within the set.

replicated those values. For the reaction of the small models with O_2, **Figure 21**, the MN12-L semi-empirical meta-GGA type functional far outperformed the others with a total error across the eight test reactions of only 5.2 kcals/mol. The next closest was the MN15 global hybrid meta-GGA type functional with a total error of 23.4 kcals/mol. These oxygenation reactions were an important benchmark as they most closely resemble the experimental reaction of interest with the [NiFe]-H_2ase models. The most interesting outlier in this group is the B2PLYP double hybrid functional which has the highest error for each individual reaction and therefore the highest total error at 128.8 kcals/mol. A possible explanation is the large underestimation error the B2PLYP functional has in the bond dissociation energy for O_2, **Figure 22**.

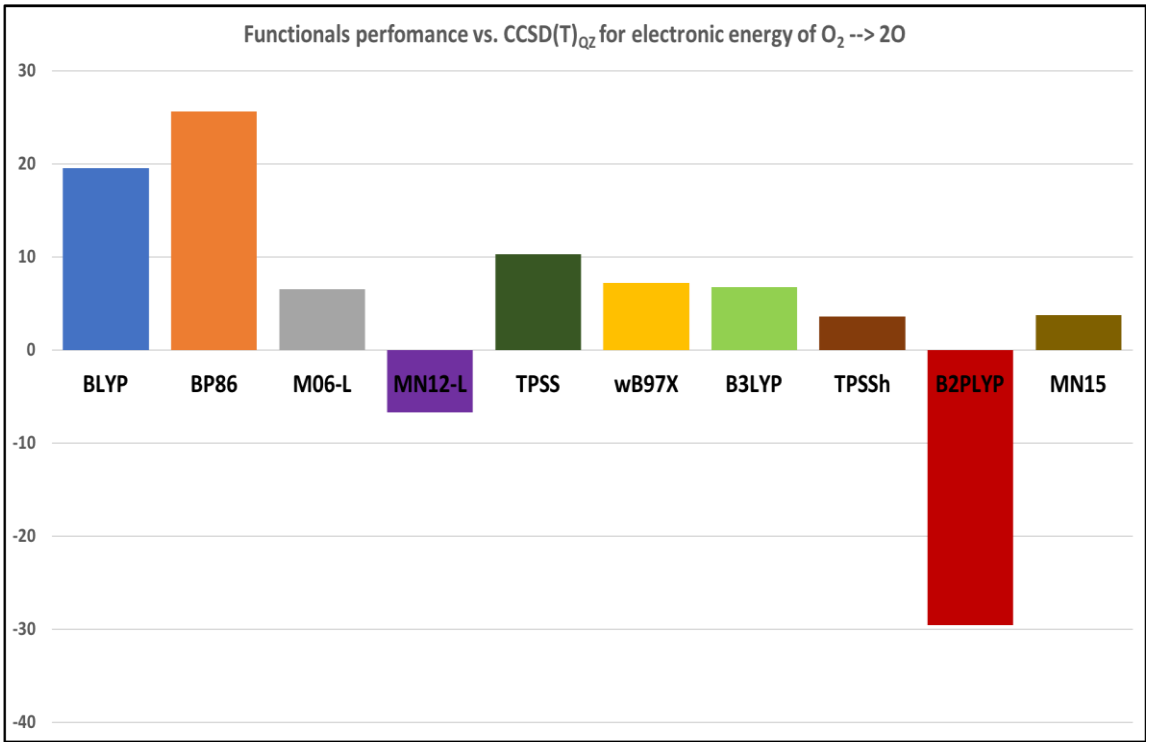

Figure 22 Comparison of DFT functionals performance on the energy of dissociating an O_2 molecule into two oxygen atoms as compared to the CCSD(T) benchmark.

Comproportionation was used as a test reaction due to the propensity of sulfur-based oxygenates to undergo this process and the possibility that the singly oxygenated forms of the [NiFe]-H_2ase model complexes might be the result of a comproportionation reaction in solution, **Figure 23**.[82] The results of the benchmarking were a close grouping of well performing functionals: MN12-L, MN15, B2PLYP, and ωB97X with 4.7, 2.8, 2.6, and 2.1 kcals/mol of total error respectively across the four comproportionation benchmarking reactions. The comproportionation benchmarking data shows an overall smaller range of errors as well as much less error overall than the oxygenation data, possibly due to the reaction remaining in the same spin state and the improved cancellation of errors that occurs when making and breaking bonds of a similar type. The majority of

the functionals tested overestimate the energy of the comproportionation reaction. The data also appears to show a correlation between the total error and the complexity of the functional used. This also supports the hypothesis that the decrease in overall error is due to an improvement in the cancelation of errors in modern functionals.

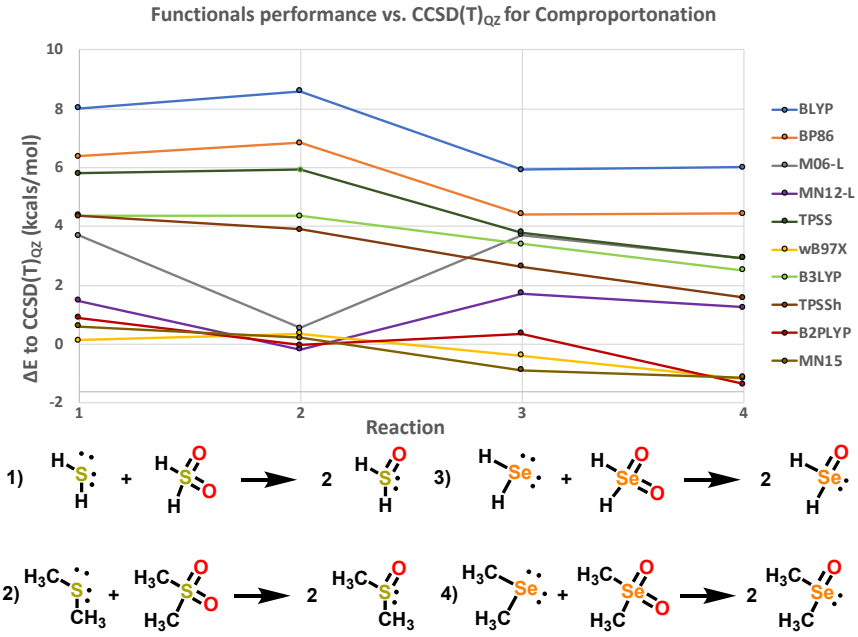

Functional	Total Error (kcals/mol)
CCSD(T)	0
BLYP	28.5
BP86	22.1
M06-L	10.9
MN12-L	4.7
TPSS	18.5
wB97X	2.1
B3LYP	14.7
TPSSh	12.5
B2PLYP	2.6
MN15	2.8

Figure 23 Comparison of DFT functionals performance on the energy of comproportionation as compared to the CCSD(T) benchmark. The top four performing functionals are highlighted in the table.

The third and final benchmarking set was isomerization of the terminal chalcogen-oxygen bond into an internal one, **Figure 24**. This was done to ensure proper determination of the lowest energy isomer of the previously reported, Yang *et al.*, [NiFe]-H_2ase singly-oxygenated model complexes as various positions of oxygen have been reported in the X-ray crystal structures of both oxygen-damaged [NiFeS]-H_2ases and [NiFeSe]-H_2ases as well as the model compounds of these enzymes.[3,22,45,51–53,56,60,62–64,83] The results of the isomerization benchmarking show that MN12L is the best performing functional with a total error of 11.1 kcals/mol. A majority of the functionals underestimate the energies of the isomerization reaction but the M06-L functional overestimates 6 of the 8 data points and has the most positive error at each data point compared to the other functionals.

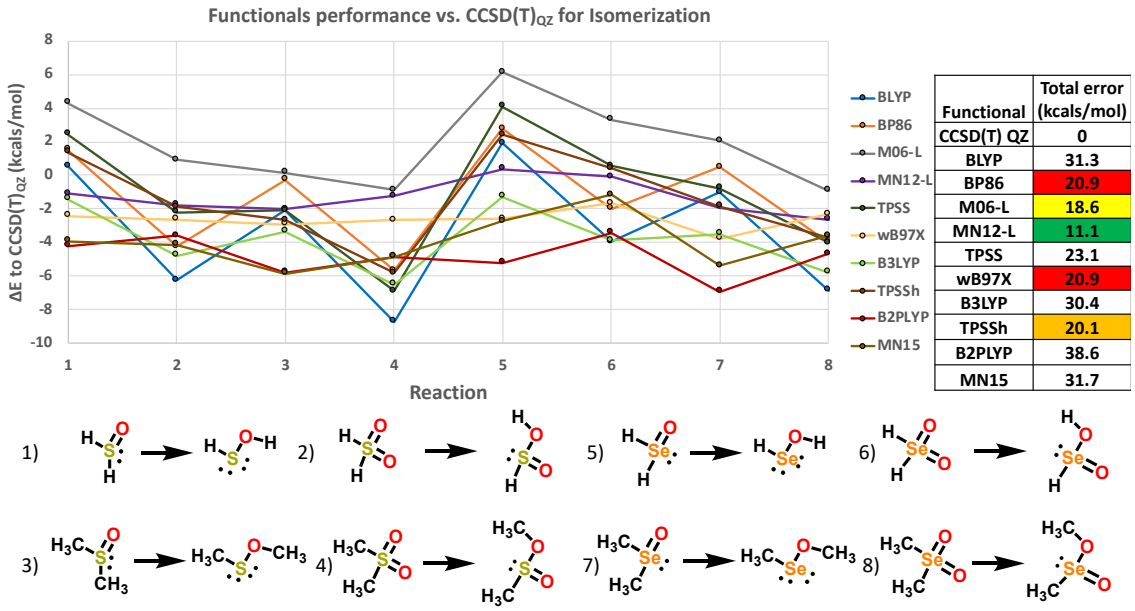

Functional	Total error (kcals/mol)
CCSD(T) QZ	0
BLYP	31.3
BP86	20.9
M06-L	18.6
MN12-L	11.1
TPSS	23.1
wB97X	20.9
B3LYP	30.4
TPSSh	20.1
B2PLYP	38.6
MN15	31.7

Figure 24 Comparison of DFT functionals performance on the energy of isomerization of the terminal chalcogen-oxygen bond to an internal one as compared to the CCSD(T) benchmark. The top five performing functionals are highlighted in the table.

With the three benchmarking sets completed, the overall performance of each functional was determined by ranking its performance within each set and aggregating the results, **Figure 25**. The MN12-L is the best overall functional for the chalcogen reactions being tested based on it being the only functional to perform in the top four in each benchmarking set. It was the best functional for both oxygenation and isomerization and was in a close fourth for comproportionation. The next best overall performing functionals in order were M06-L, ωB97X, and MN15. These functionals, especially MN12L and MN15, represent some of the most heavily parameterized ones tested in this study.

Total error comparison of DFT functionals to $CCSD(T)_{QZ}$

	O_2 Addition	Comproportionation	Isomerization
CCSD(T)	0	0	0
BLYP	77.6	28.5	31.3
BP86	46.8	22.1	20.9
M06-L	28.8	10.9	18.6
MN12-L	5.2	4.7	11.1
TPSS	54.1	18.5	23.1
wB97X	69.0	2.1	20.9
B3LYP	78.6	14.7	30.4
TPSSh	62.0	12.5	20.1
B2PLYP	128.8	2.6	38.6
MN15	23.4	2.8	31.7

Figure 25 Comparison of DFT functionals performance as compared to the CCSD(T) benchmark for all three benchmarking reaction sets. The top four performing functionals for each reaction are highlighted in the table. Values are in kcals/mol.

With a champion functional in hand, the full [NiFe]-H_2ase model complexes were calculated to both confirm the previously reported isomer results as well as determine the value for the single and double oxygenation reactions and possible comproportionation,

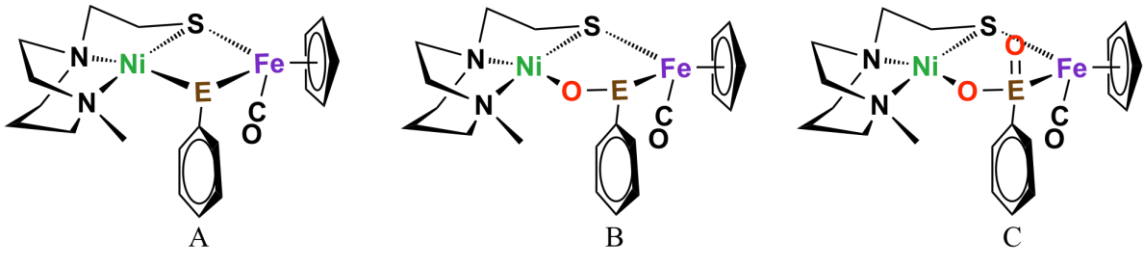

E	O Addition (A + O)	O_2 Addition (A + O_2)	Comproportionation (A + C → 2B)
Se	-20.1	-31.7	8.6
S	-20.3	-50.4	-9.8

Figure 26 DFT results for energies of single and double oxygenation and comproportionation reactions for full [NiFe]-H_2ase model complexes using MN12L functional. Values are given in kcals/mol.

Figure 26. The results for single oxygenation of the complexes are very similar for both sulfur and selenium with free energies of the reactions of -20.3 and -20.1 kcals/mol, respectively. There is a sizable energy difference however when adding the second oxygen with the sulfur and selenium reactions having free energies of -50.4 and -31.7, respectively. The reason for this difference has been attributed by Yang *et. al.* to the difference in the strength of the terminal oxygen bond for sulfur and selenium as determined by NBO analysis. The comproportionation results show that the reaction would be favored for sulfur by -9.8 kcals/mol and disfavored for selenium by 8.6 kcals/mol. These results along with the previously reported O^{16}/O^{18} mass spectrometry data indicate the singly oxygenated selenium complex found by XRD is most likely due

to the removal of the terminal oxygen by another species in solution. The identity of the species is still unknown but is under further investigation.

2.4.1 Computational Methodology

The crystal structures of **2** and **2+O** were used as geometric starting points for DFT calculations (TPSSTPSS functional with the 6-311++G(d,p) basis set on all nonmetal atoms and the 6-311+G basis set for Ni and Fe atoms) and then optimized using the Gaussian 09 program using the SMD implicit solvation model with acetonitrile as the solvent.[84] The calculated structures for **2** and **2+O** showed excellent agreement with the corresponding experimental structures, **Figure 7**. Similar structures were found for **2+2O** as well as the sulfur analogues, **1**, **1+O**, and **1+2O**.

For the modified phenyl-chalcogenate structures, DFT calculations were performed using the TPSSTPSS functional with the 6-311++G(d,p) basis set on the nonmetal atoms and the 6-311+G basis set on nickel and iron in the Gaussian 16 suite.[85] The molecular structures from XRD presented above were used as geometric starting points with all other structures made by the appropriate atomic substitutions in the AMPAC Graphical User Interface (AGUI).[86] All structures were optimized in solvent by using the SMD solvation model with acetonitrile as the solvent. Vibrational frequencies were calculated in solvent and all species were confirmed to be minimum energy structures by the absence of any imaginary frequencies. Standard statistical mechanical and solvation corrections were applied to the electronic energy of the optimized structures to give free energy values.

The small model calculations to determine the best functional to describe the E=O bonding were performed using the Gaussian16 suite.[85] All small model compounds geometries were first optimized using the TPSSTPSS functional with Def2TZVPP basis set and tight convergence criteria. The TPSSTPSS functional was chosen as it had previously performed well in replicating the geometries of the **Ni**(μ-E_{Ph})(μ-S'_{N2})**Fe** complexes, **Figure 13**. All species were confirmed as minimum energy structures by the absence of imaginary frequencies. The optimized geometries were then used in single-point CCSD(T) calculations using a CC-PVQZ basis set. Standard statistical mechanical corrections were applied to obtain gas phase free energy values. The small models were then calculated using each of the 10 selected DFT functionals with the same optimized geometry as the CCSD(T) calculations using the CC-VPVTZ basis set and the same corrections were applied to find the gas phase free energies. The functionals used were B2PLYP, B3LYP, BLYP, BP86, M06-L, MN12L, MN15, TPSSTPSS, TPSSh, and ωB97x. These functionals were chosen as they cover several different types of functional, **Figure 6**, and were deemed to perform well overall in an extensive functional review by Mardirossian & Head-Gordon.[87] The full model compounds **1, 1+O, 1+2O, 2, 2+O,** and **2+2O**, were calculated using the previously reported X-ray crystal structures as geometric starting points.[67] The structures were then optimized in solvent using the SMD implicit solvation model with acetonitrile as the solvent and the best performing functional MN12L. The models used a split basis set with a 6-311++G(d,p) basis set being used for the nonmetals and a 6-311+G basis set used for the metals. The same check for imaginary frequencies as well as the corrections to free energy were performed. The DFT functionals

performance was based on the total error compared to the CCSD(T) benchmarks. This error was calculated by summing the absolute value of the error for each compound in a given reaction type. The best performing functional therefore would have the lowest overall error when compared to the others.

2.5 Conclusion

In summary, we have observed oxygenation and O-atom removal from two biomimetic complexes with features of the [NiFe]/[NiFeSe]-H_2ase active sites. The complexes synthesized by Dr. Yang highlight the usefulness of the $[NiN_2S]_2^{2+}$ synthetic platform for generating NiFe biomimetic complexes. The asymmetric oxygenation pattern of the sulfur and selenium containing variants afforded an opportunity for computational investigation into the underlying chemical properties of sulfur and selenium. The substitution of these two elements has a profound effect on these complexes and gives insight into their importance in the [NiFe]-H_2ase active site.

Clearly the $NiE_{Ph}Fe^+$ biomimetic differs from the active site of [NiFeSe]-H_2ase as the selenium in the former is in a bridging position, rather than the terminal position as nature has adopted. Nevertheless, the relative reactivities are consistent with what is found in nature. As compared to complex **1**, the selenium-bridged complex **2** required a shorter time to generate oxygenated selenium, **2+O**. The partial conversion of oxygenated chalcogenides (Se or S oxidation states of 0) back to reduced S/Se (oxidation state -2) in our studies provides a foundation for the mechanism of reactivation of S/Se-oxygenated [NiFeE]-H_2ases. Oxygen-uptake by S/Se in [NiFeS]- and [NiFeSe]-H_2ases results in

modification of the active site, but less severe than would result in irreparable degradation from metal oxidation.[26] During the oxygenation and O-atom removal from the chalcogen atom, we note that the mobility in the Ni-E bond plays a vital role.

The variety of chalcogen oxygenates thus far found in nature, **Figure 4**, speaks to the ability of the chalcogens to maintain a close attachment to the NiFe site. Detailed O_2/H_2ase active site reaction mechanism remain obscure but are of great interest.[88,89] Our studies of model complexes point to the possibility of opening the Ni-E bond in the Ni-(μE_{Ph})-Fe unit. Such bond cleavage exposes a reactive lone pair on E that attracts the electrophilic O_2 molecule concomitant with providing an open site on Ni^{2+} for assisted activation, leading to the proposed superoxide intermediate and the subsequent product. A related strategy for protection of the active site from oxidative damage is seen in the membrane-bound respiratory [NiFe]-hydrogenase wherein the proximal [4Fe-3S] cluster donates two electrons and one proton for reduction of adventitious O_2.[30] This work highlights the usefulness of the $[NiN_2S]^{2+}$ synthetic platform for generating NiFe biomimetic complexes.[34]

The nominal models of [NiFeS]- and [NiFeSe]-H_2ase active sites described above with bridging chalcogenides function as a probe of O_2 reactivity that yield isolable NiFe complexes where thiolate and selenolate are converted into sulf- and seleno-oxygenates. The presence of a carbon monoxide reporter ligand on Fe offered opportunity to explore "electronic alchemy" through remote effects of substituents on the E_{PhX} ligand that effectively (electronically) transformed S into Se. This is seen by the almost identical ν(CO) shifts for the S_{PhNMe2} and Se_{PhH} complexes both experimentally as well as

computationally. Preliminary Mossbauer studies by my coworker Kyle Burns find simple quadrupole doublets and nearly identical isomer shifts for the parent Ni-Fe-S and Ni-Fe-Se reduced complexes. Thus, the increased electron density from the Se that influences the *v*(CO) IR values via Fe^{II} has no effect on the iron nuclei. This observation has not yet been explained by theoretical investigations.

The stability of these NiFe complexes, even under siege by O_2, is impressive. Crystallography finds only minimal changes in the coordination sphere of the bimetallic complex; the NiFe core is maintained with marginal differences in the Ni--Fe distances even though the -E_{PhX} bridging ligand has been expanded into an Ni-O-S-Fe or Ni-O-Se-Fe unit.

We surmise that the rigidity of the tridentate N_2S "pincer" type ligand guides production of E-oxygenates at the more mobile, mono-dentate, bridging E_{PhX} ligand site. Consistent with this conclusion are results from the Ogo group using NiN_2S_2 (with N_2S_2 as a fixed tetradentate binding site for Ni^{II}) as metalloligand to Cp^*Fe^{II}, bearing an open site on iron.[21,88,89] Under O_2 such Ni-Fe complexes yield isolable Fe^{IV}(peroxo) species, with O_2^{2-} side-on bound to Fe in $[NiN_2S_2\text{-}Fe(O_2)Cp^*]^+$ rather than any of the S-oxygenates displayed in **Figure 5**. This is also supported by the results shown in **Figure 16**. The N_2SE_{Ph} ligand field falls in a "Goldilocks" zone of rigidity and accessibility as compared to the analogous N_2S_2 and $N_{2(}E_{Ph})_2$ ligand environments. The N_2SE_{Ph} helps direct the O_2 towards the accessible binding site on the nickel center where the nearby E_{Ph} can act as a sacrificial reductant and protect the two metal centers from oxidation and deactivation.

The oxidation states of Ni and Fe in the product oxygenates of our study remain at Ni^{II} and Fe^{II} for both the selenium and the sulfur derivatives. However, we note that low temperature (0°C) monitors of the O_2 reactions with the Ni-Fe containing the μ-S_{PhNMe2} bridging ligand found a buildup of a transient EPR-active species as the reaction proceeded; a signal at $g_{avg} \approx 2.09$ is assigned to Ni^{III} while one at g = 4.19 is likely Fe^{III}. At reaction's end, oxygenated sulfurs were produced and the (presumed) Ni^{III} signal had disappeared. Some byproduct containing iron(III) is found in the oxidized residue from these reactions. These observations are reminiscent of the early EPR studies of [NiFe]-H_2ase redox poised in different levels, which gave rise to signals for Ni-A and Ni-B.[25,51,52]

The preference of O-atom bridged S and Ni, that we observed here, is seen in the sulfinato complex of O-damaged [NiFeS]-H_2ase, **(Figure 5)**. The Ni-O-Se-Fe as a bridging unit is also observed here, but it is opposite to the Ni-Se-O-Fe arrangement found in one of the forms of O-damaged [NiFeSe]-H_2ase.[55,56] In fact, protein crystallography has uncovered a variety of chalcogen-oxgenates and myriad binding modes in the structures of oxygen-damaged [NiFe]-H_2ase enzyme active sites; such a display is likely a benefit of reaction within a restrictive enzyme active site cavity that partially accounts for the longevity of these species. One specific binding mode that should be investigated more closely is the one involving a selenocysteine bound the the nickel center through two oxygen atoms as seen in **Figure 4**. This configuration appears to contradict the results we have seen computationally in which a doubly oxygenated selenoate is unstable. It is possible that either the nickel center or some secondary sphere residues with hydrogen bond donors provide enough stabilization for this binding motif to exist in nature where it

does not in the model complexes. The mechanism and various configurations of oxygenation in the protein active site is best explored through a hybrid quantum mechanics/molecular mechanics (QM/MM) approach that allows for accurate electronic structure calculations while considering the secondary sphere effects of the amino acid residues surrounding the active site. Breglia et al. has begun utilizing this approach in their work on the oxidation of the Ni-C state to the "unready" Ni-A and Ni-B states and subsequent reactivation.[90,91] In contrast, in oxygenated solutions containing our small molecule active-site analogues, serious oxygen exposure and damage is likely to lead to intractable metal oxides.

While there are discernible variations in oxygen uptake and product distributions that show correlations with electronic differences in the para-substituent series, the possible causes are many and expected to be intricately interrelated. For example, enhancement of electron-rich character at E in E_{PhX} from the para-substituent effect, increases the likelihood for O_2 binding both to E, S or Se, as well as to the metals which they bridge. Assuming that the affinity for the E_{PhX} ligand by Fe^{II} continues to be greater than to the Ni^{II}, then the O_2-uptake activity should be limited to the two sites, Ni^{II} and $^{-}E_{PhX}$.

We have seen in these studies, consistent with the enzyme studies or results, that selenium exhibits more rapid reactions for O_2 uptake. The observed oxygenated Se product is a single oxy species (we cannot discount a di-oxy species as intermediate), and O-atom removal is facile for selenium. Excellent commentaries regarding "Why nature chose-"[37,92] heavier elements in the chalcogen or pnictogen family for numerous biological

processes clearly point to their intricate interactions with oxygen. In hydrogenase enzyme chemistry, the many benefits of selenium incorporation include not only enhancement of catalytic activity through proton shuttling and hydrogen expulsion rates, but also of protection of the active sites from the poisonous O_2. Such benefits apparently outweigh the added cost to the organism of the biosynthesis. As of now, there are few synthetic hydrogen evolution reaction (HER) or oxygen reduction reaction (ORR) molecular catalysts that target selenium substitution and explore possible paybacks for the minimal synthetic expenditure.[26] One example is the HER catalyst developed by Pan et al. which features a nickel center ligated by a 1,2-benzenediselenoate.[93] This substitution from the analogous dithiolate to the analogous diselenoate improves the turnover frequency (TOF) from 600 s^{-1} to 7838 s^{-1} respectively. The catalyst also demonstrates no product inhibition by H_2 and operates at roughly 90% efficiency under atmospheric levels of O_2 compared to idealized anaerobic conditions. Moving forward, the integration of the insights from experimental optimization of catalyst production with the insights from computational investigations of the fundamental properties that make the [NiFeSe]-H_2ases such efficient and robust catalysts will lead to the development of better fuel cells and electrolyzers.

CHAPTER III

ASSEMBLY AND CARBON MONOXIDE EXCHANGE PROPERTIES OF A THIOLATE BRIDGED DIMANGANESE COMPLEX

3.1 Introduction

Metalloproteins exemplify how transition metal cations achieve favored coordination numbers, geometries and donor types from a variety of ligand types in order to assemble complex structures with highly tuned functions. In addition to the highly prevalent cysteine-S and histidine-N amino acid donor sites, the Cys-X-Cys tripeptide motif is well known to use deprotonated amido nitrogen bases to bind Ni, Fe, and Co in a stable N_2S_2 ligand field.[94] The active site of nitrile hydratase features an iron or cobalt ligated in a Cys-Ser-Cys environment with the terminal thiolates having been oxygenated.[95] A Ni analog found in acetyl-CoA synthase binds one nickel within the Cys-Gly-Cys pocket and uses the two thiolate sulfurs to bind an exogeneous Ni critical for enzymatic activity.[96–98] Attempts to model these natural processed have inspired synthetic bioinorganic research towards small molecule analogs of these enzyme active sites. The Cys-X-Cys small molecule mimic, a tetraanionic N_2S_2 ligand known as *'ema'* (N,N'-ethylenebis(mercaptoacetamide), has served as a crucial tool in efforts to replicate the efficient and selective reactivity of the natural enzymes and the robustness while achieving the desired robustness and output of commercial catalysts.[99,100]

Our group has developed simplified models of the biological Cys-Gly-Cys Ni-binding sites by using the dianionic bis-mercaptoethane-diazacyclooctane, -heptane, and -hexane ligands and their open chain analogues to produce neutral MN_2S_2 complexes.[73,101]

The cis-dithiolates of these MN_2S_2 have lone pairs oriented in a way that allows for accessible binding of additional metals to generate diverse clusters and views the MN_2S_2 metalloligand as a versatile analog of bipyridine or diphosphines.[73,102] With these metalloligands, previous group members have prepared bimetallic complexes MN_2S_2•$Mn(CO)_3Br$ (M = {FeNO, {CoNO} and Ni^{II}) similar to the $(bipy)Mn(CO)_3X$ known for electrocatalytically reducing CO_2, but creating the opportunity for inclusion of pendant metal.[103–110] My coworker Trung Le targeted electron-rich versions of these MN_2S_2 complexes made from the ema^{4-} ligand of $[V{\equiv}O]^{2+}$, Ni^{2+}, and Fe^{3+}, complexes **2**, **3**, and **4**, in **Figure 27**. He expected to generate heterobimetallic complexes similar to those that have been previously reported but with a more labile bromide due to the increased electron density of the manganese.[111,112] This labile bromide was expected to lead to increased activity in the reduction of CO_2. His results instead showed two manganese atoms trapped in an unexpected orientation of the H_2ema^{2-} ligand, **5** in **Figure 27**. This result created an opportunity for examination of **5**'s structure and synthesis through DFT methods and has more general implications for the selective synthesis of other homobimetallic complexes.

3.2 Synthesis and Characterization of (Mn*ema*)$_2$

The vanadyl and nickel MN_2S_2 complexes , **2** and **3** in **Figure 27**, were previously reported by Jenkins et al. and Kruger et al., respectively, and compound **4** was recently reported by Le et al.[99,113,114] Reactions of each of these species with $Mn(CO)_5Br$ (**1**)

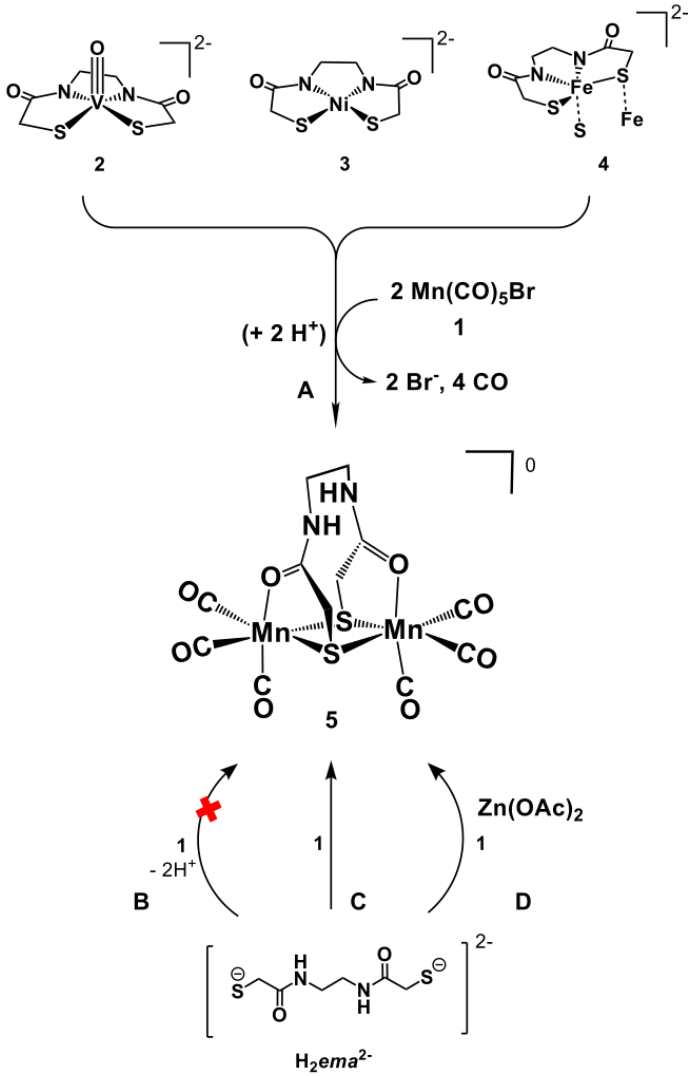

Figure 27 Synthesis of 5 under diverse conditions: A) $[M(ema)]^{2-}$ (Metal templating); B) as attempted from $(ema)^{4-}$; C) from $(H_2ema)^{2-}$ in absence of metal; D) from $(H_2ema)^{2-}$ in the presence of 1 equiv. $Zn(OAc)_2$ as *in situ* templating metal. Reprinted with permission from (Le, 2019).

(**Figure 27-A**) led to the same isolable dimanganese product , **5**, as confirmed by identical ν_{CO} IR spectral changes and m/z in the mass spectrum. Two versions of the isolated

H_2*ema*-bridged dimanganese XRD structure is shown in **Figure 28**. The metal inside the N_2S_2 pocket of each of the metallodithiolates synthons was displaced by two hydrogen atoms originating from adventitious water in the solvent that formed protonated amido nitrogens. This made complex **5** unusual as an S-bridged binuclear species with a

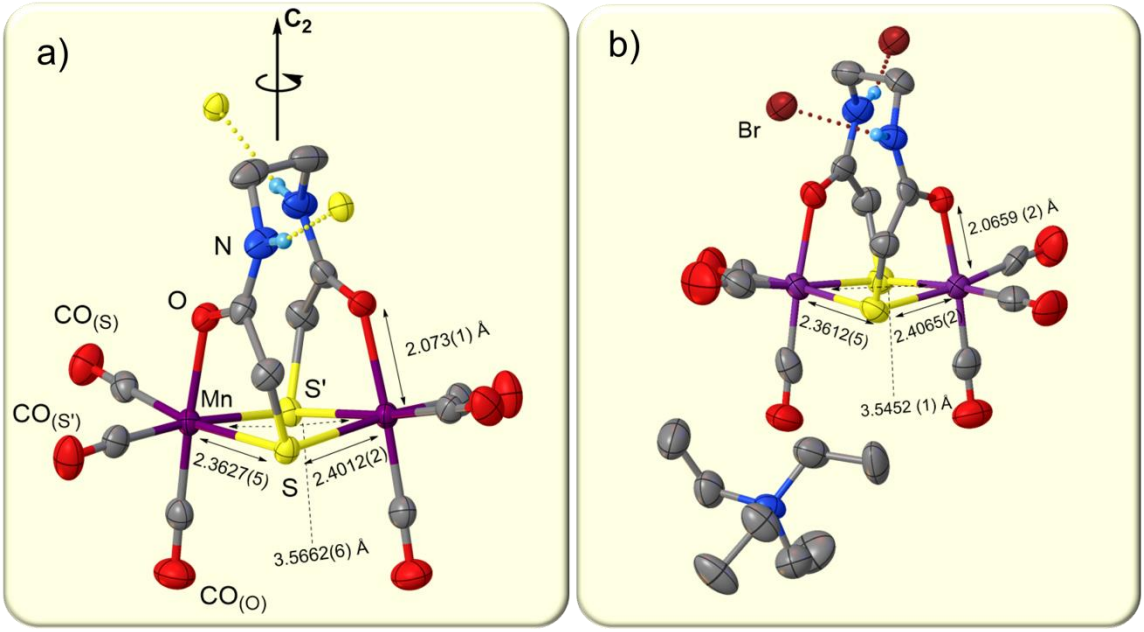

Figure 28 Thermal ellipsoid plots at 50% probability of two isolated crystalline forms of 5 showing intermolecular hydrogen bonding; H atoms omitted except for amide H. a) Complex 5 exhibiting H-bonds with the bridging S of adjacent molecules. b) Complex 5·Et_4NBr showing H-bonds with Br^-. Reprinted with permission from (Le, 2019).

carboxamide oxygen donor in comparison to the expected S-bridged heterobimetallic clusters that have previously been seen.[73]

The unexpected structure of **5** seemed to defy the conventional understanding of the tetradentate '*ema*' ligand and led to the exploration of alternate synthetic routes for the formation of **5**. **Figure 27**, routes **B**, **C** and **D**, implicate a templating effect with driving forces arising from the more favorable carboxamide oxygen metal binding compared to the deprotonated amido nitrogens. Route **D** shows the effects of adding kinetically labile

Zn^{2+} to promote the folding of H_2ema^{2-} through metal templating. This approach resulted in almost quantitative conversion to **5** as compared to the previous approximately 50% yield without the added Zn^{2+}.

3.3 ^{13}CO exchange Experiments

To study the chemical heterogeneity of the CO ligands around each Mn^{I} center, $^{13}CO/^{12}CO$ exchange reactions were conducted in multiple solvents and the results of FT-IR and C-13 NMR spectroscopies are summarized in **Figure 29**. The enrichment of the ^{13}CO NMR signal in methanol (MeOH) was appreciably faster than in either tetrahydrofuran (THF) or dimethylsulfoxide (DMSO). Three new ν(CO) bands appeared simultaneously that had an observed $\Delta\nu(CO) \approx 43$ to 48 cm^{-1}

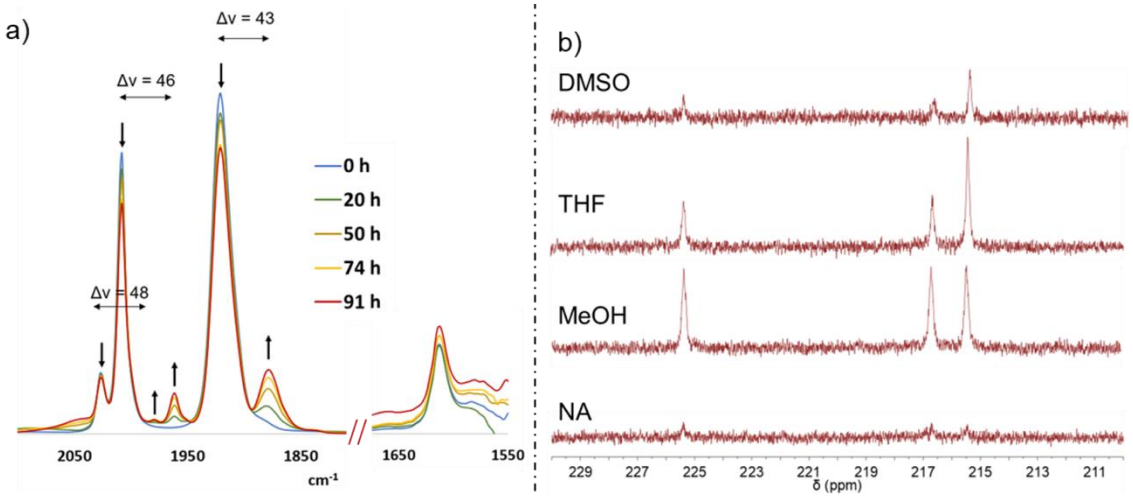

Figure 29 a) FT-IR spectra of 5 under ^{13}CO ($\geq$ 1 atm) in MeOH b) Stacked ^{13}C – NMR spectra (taken in DMSO-d_6) of 5 isolated from partial ^{13}CO enrichment in different solvents, as indicated, in comparison with the natural abundant ^{13}C – NMR spectrum with δ_{CO} (ppm): 215.4, 216.7 and 225.4. Reprinted with permission from (Le, 2019).

(**Figure 29a**) consistent with the difference in reduced mass. The ^{13}C-NMR spectrum of the exchange in MeOH agrees with this observation (**Figure 29b**) where the intensities of

all three resonances assigned to CO ligands increase at the same rate, maintaining their 1:1:1 relative ratio. The exchange in THF (or DMSO) was slower and showed one signal at 215.4 ppm growing in faster than the other two. This suggests selectivity in the CO exchange process in these solvents that is not seen in MeOH. This difference was explored by DFT calcualtions to determine the link between solvent identity and selectivity as well as the mechanism of CO exchange.

3.4 Computational Investigations

The formation of **5** is striking not only because of its composition, but also because it deviates so drastically from previously reported compounds. This includes **2**, **3**, and **4** from **Figure 27** that from stable bimetallic compounds with their bridging thiolates in a butterfly geometry instead of the diamond seen in **5**.[111,112] The other striking feature of this synthesis is the impact of using Zn^{2+} as a templating agent which improves the synthetic yield from approximately 50% to quantitative.

Initially the mechanism was explored starting from H_2ema^{2-} and $Mn(CO)_5Br$, route **C** from **Figure 27**, as this provided a more straightforward path than route **A** which necessitates mass and charge balancing of the equation with several unknown products. The only side products in Route **C** are CO molecules and a bromide ion. To avoid errors associated with solvation of free bromide the $Mn(CO)_5Br$ reagent was replaced with $Mn(CO)_6^+$. We propose that the assembly of **5** from 2 equivalents of $Mn(CO)_6^+$ and H_2ema proceeds through a route analogous to the one depicted in **Figure 30**. The first step is the substitution of one CO for one of the thiolates of the H_2ema ligand to form **6**. This creates

the possibility for two plausible paths involving the other thiolate of the H_2*ema* ligand. Either an intramolecular ligand substitution occurs where the thiolate replaces a second

CO on the bound manganese center, **7**, or an intermolecular ligand substitution in which

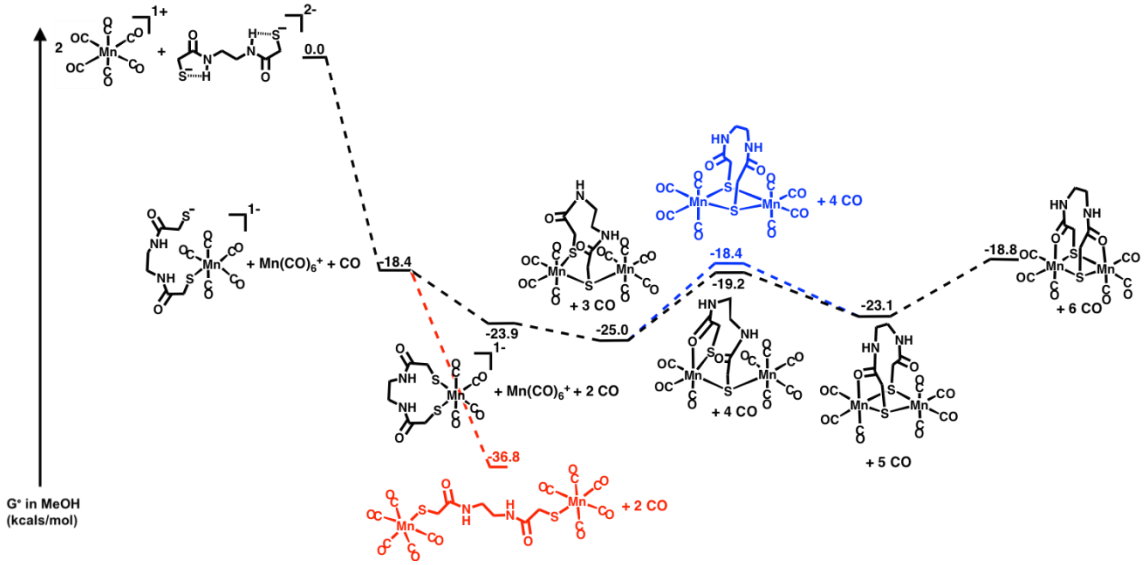

Figure 30 DFT computed mechanism for the assembly of **5** starting from $Mn(CO)_6^+$ and H_2*ema*.

the thiolate replaces the CO on a second equivalent of $[Mn(CO)_6]^+$ **8**. The intermolecular product **8** is more stable than the intramolecular product by 12.9 kcals/mol.

This difference explains the why adding Zn^{2+} to the reaction mixture has such a profound impact on the yield of **5**. Without the Zn^{2+}, in order for the reaction to proceed to **5**, the more kinetically accessible intramolecular reaction to form **7** must first occur. Then the subsequent reaction with another equivalent of $[Mn(CO)_6]^+$ must form **9** before the more thermodynamically favorable **8** can be realized. The Zn^{2+} likely forms a complex with H_2*ema* in solution that prepositions the thiolates in close proximity to each other leading to a faster formation of **7** and preventing the possibility of the side product **8**.

Attempts to discern the active zinc complex or find intermediates involved in this templating effect have been met with limited success.

After formation of **9**, the reaction proceeds through intramolecular ligand exchange reactions of the labile CO's for the thiolate and amide donors of the H_2*ema* ligand. Starting from the asymmetric $Mn(CO)_4(Mn(CO)_5$ complex, **9**, the reaction can proceed to form either the asymmetric $Mn(CO)_3(Mn(CO)_5$ complex, **10**, or the symmetric $Mn(CO)_4(Mn(CO)_4$ complex, **11.** These two species are only 0.8 kcals/mol apart in energy and both lead to the penultimate intermediate $Mn(CO)_3(Mn(CO)_4$ complex, **12**, which loses a final CO to produce **5**. These reactions from **9** to **5** are fairly flat along the potential energy surface for the reaction but appear to be uphill according the DFT calculations. The reaction steps should be more favorable from the entropic driving force of CO ligand

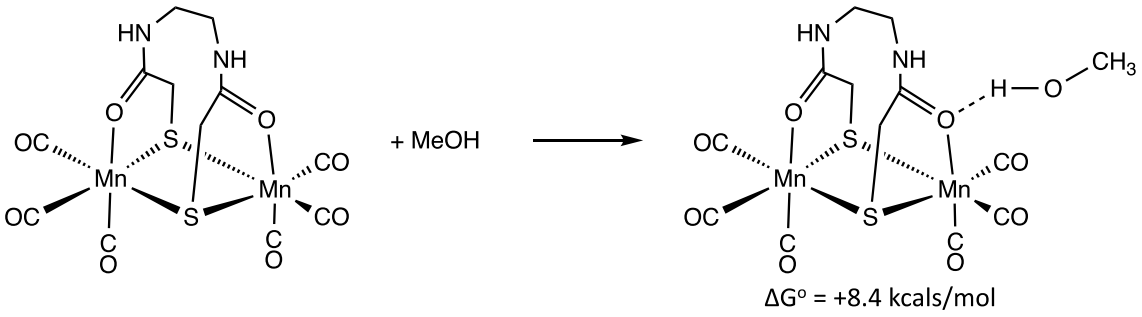

Figure 31 DFT calculated free energy change of hydrogen binding a methanol molecule to **5**.

loss which will bubble out of solution as the reaction proceeds and shift the reaction equilibrium towards product formation according to Le Chatelier's principle.

The asymmetric CO exchange behavior seen in the ^{13}CO labeling experiments,

Figure 29, was also explored through computational chemistry. The biggest difference between methanol and the other two solvents, THF and DMSO, is the ability of methanol to act as a hydrogen bond donor. **Figure 31** shows that the process of binding a methanol molecule to the amide oxygen donor is an endergonic process by 8.4 kcals/mol. This process is uphill because the energy released from the formation of the hydrogen bond is not enough to overcome the energy lost by the destabilization of the O-Mn bond and its elongation from 2.082 Å to 2.098 Å.

As the two manganese centers in **5** are in stable 18 e^- coordination environments, a dissociative pathway for CO exchange was hypothesized to be the most plausible.

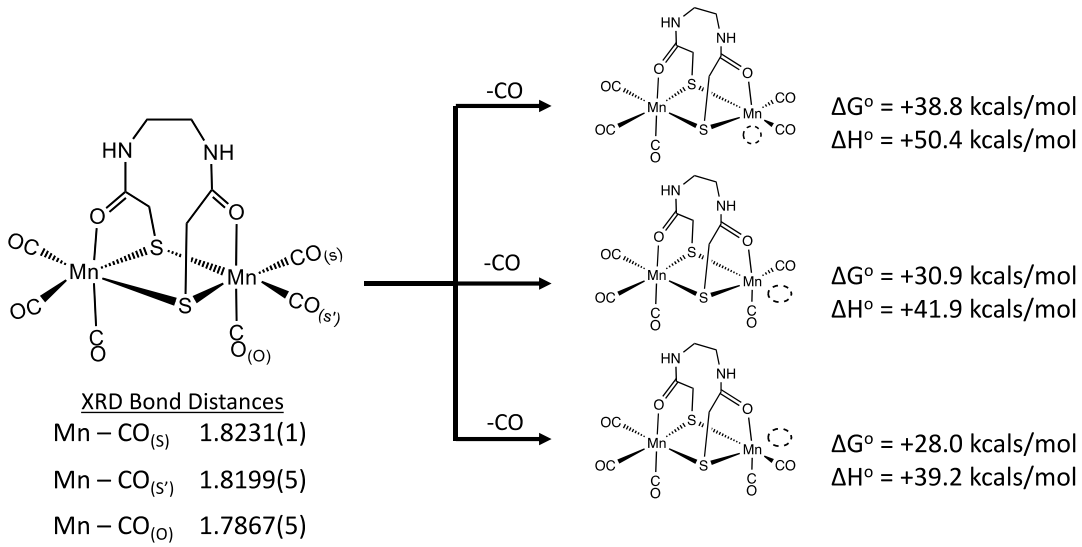

Figure 32 Free energy and enthalpy changes for the dissociation of the CO's from **5** along with the Mn-C bond distances for each CO from the XRD structure.

Figure 32 shows the difference in free energy and enthalpy for the dissociation of each chemically unique CO. The weakest bound CO is the one trans to the sulfur that forms a

five membered ring with the Mn and amide oxygen; i.e., the shorter of the two Mn-S bonds. Since the reaction involves little rearrangement and the breaking of a single bond,

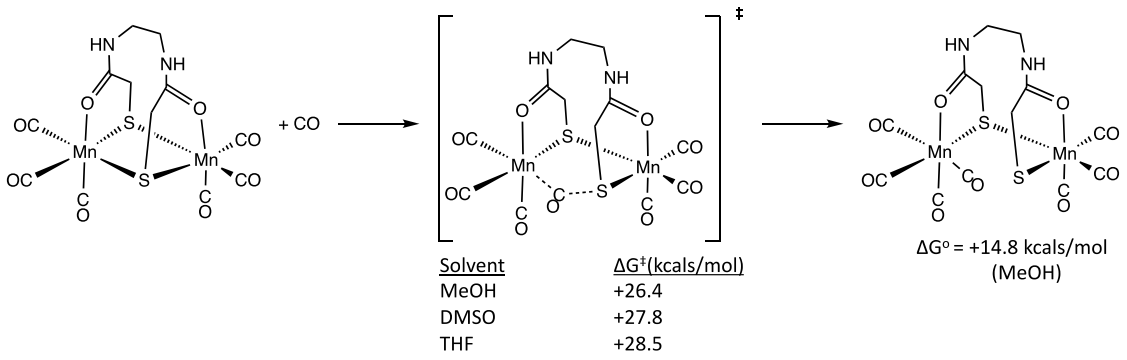

Figure 33 Insertion of CO into the longer Mn-S bond. Free energy values are in kcals/mol.

the enthalpy change of the reaction, 39.2 kcals/mol, should be close to the activation energy of the reaction. As the CO exchange occurs at room temperature, this value for the activation energy is too large for the CO-dissociative mechanism to be plausible.

An interchange mechanism requires a free CO to bind to the manganese center while either one of the thiolates or the amidic oxygen is simultaneously displaced. Insertion into the longer Mn-S bond is an uphill reaction in MeOH by 14.8 kcals, **Figure**

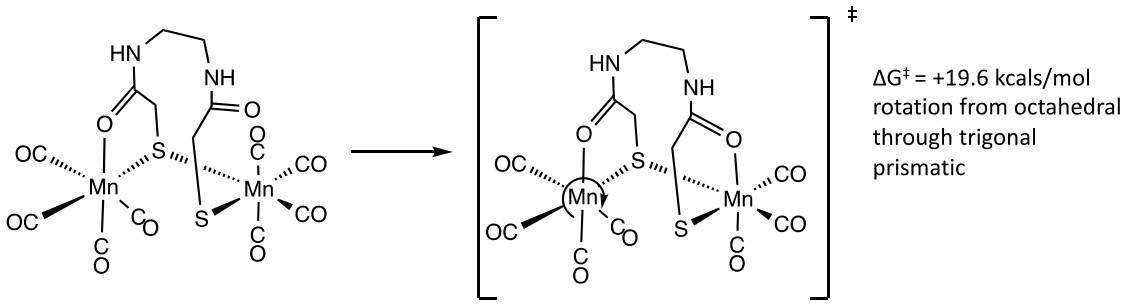

Figure 34 Rotation through a trigonal prismatic transition state for the proposed $Mn(CO)_4Mn(CO)_3$ intermediate for CO scrambling.

33. The transition state for such an insertion ranges from 26.4 kcals/mol for MeOH to 28.5

kcals/mol for THF, all of which are accessible barriers at room temperature. A rotational rearrangement of the CO ligands is required to generate the multisite scrambling seen in **Figure 29**. A rotation of three of the CO's through a trigonal prismatic transition state has a barrier of an additional 19.6 kcals/mol, **Figure 34**. The overall barrier then for this scrambling would be 46 kcals/mol in MeOH, again putting it outside the realm of

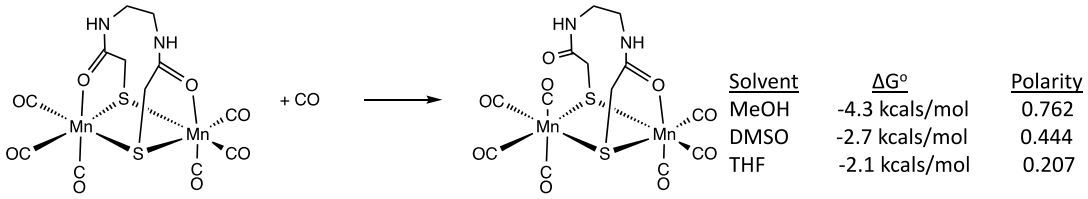

Figure 35 DFT calculated free energy for the replacement of the amidic oxygen donor with a CO.

plausibility to occur at an appreciable rate at room temperature.

Another possibility for an interchange process is for the incoming CO ligand to replace the amidic oxygen donor, **Figure 35**. This reaction is thermodynamically downhill for each of the three calculated solvents with MeOH being the most favorable at -4.3 kcals/mol. The free energy change for this reaction correlates with the relative polarity of

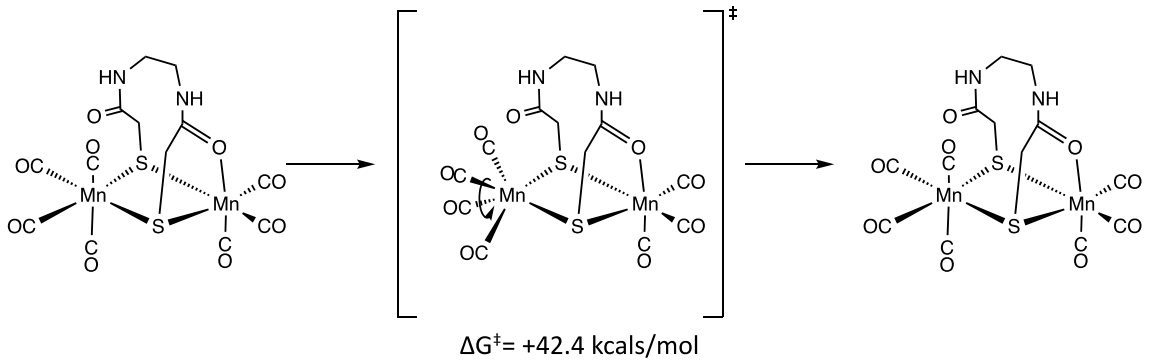

Figure 36 DFT calculated transition state involving the simultaneous rotation of all four CO's on the manganese center.

the solvents which takes into account the dielectric constant of the solvent as well as its

dipole moment and ability to hydrogen bond among other empirical parameters.[115] The more favorable binding in MeOH could facilitate the formation of the isotopomers. as the barrier for the reverse reaction would be highest for MeOH compared to the other solvents and therefore slower. A potential isomerization process was considered in which the four CO ligands rotate simultaneously, **Figure 36**. This transition state has a high barrier of 42.4 kcals/mol. The steric encumbrance of the manganese from the amide oxygen on one side and the hydrogens on the nearby methylene linker to the thiolate on the other side along with the necessity of moving all four CO's together leads to this inaccessible transition state. It is possible that a trigonal prismatic transition state similar to the one calculated in **Figure 34** exists but attempts to calculate it have so far proved unsuccessful. The intermediate from **Figure 36** should possess a transition state similar to the one seen in **Figure 34**, This would be a feasible pathway to explain the experimental results from the $^{13}CO/^{12}CO$ scrambling studies, **Figure 29**.

3.4.1 Computational Methodology

The molecular structure of **5** from XRD presented above was used as the geometric starting point with all other structures made by the appropriate atomic substitutions in the AMPAC Graphical User Interface (AGUI).[86] DFT calculations (TPSSTPSS functional with the 6-311++G(d,p) basis set on all nonmetal atoms and the 6-311+G basis set for the Mn atoms) and then optimized using the Gaussian 16 program using the SMD implicit solvation model with methanol as the solvent.[85] Vibrational frequencies were calculated in solvent and all species were confirmed to be minimum energy structures by the absence

of any imaginary frequencies. Transition states were confirmed by the presence of a singular imaginary frequency. Standard statistical mechanical and solvation corrections were applied to the electronic energy of the optimized structures to give free energy values.

3.5 Conclusions

While the mimics of biological N_2S_2 binding sites, including those with the *ema* ligand are well known, this example of H_2ema^{2-} as a binucleating ligand via a square M_2S_2, face to face, core has not been reported to date. The various synthetic routes to complex **5** illustrate the types of ligand exchange processes that occur in the formation of metalloproteins and enzymes. An example is the bioassembly of the active H-cluster in [FeFe]-H_2ase which involves the generation and attachment of CO and CN ligands to the iron centers by a trio of key mutase enzymes HydE, HydF, and HydG.[116] The folding and protonation of *ema* to form **5** evokes similarities the system studied by to Dunbar, *et al.*, where the preference of metals binding to small peptides through either a deprotonated amido nitrogen or the tautomeric carboxyl oxygen was determined.[117]

Complex **5** is a highly stable thermodynamic sink but also possess the ability to perform ligand exchange reactions at ambient conditions. Computational studies have helped elucidate a possible pathway in the assembly of complex **5** as well as a potential side product that forms without the addition of Zn^{2+} as a chelating agent. Future studies should aim to derive the full mechanism with transition states for the CO removal as well as explore the selective formation of **5** instead of the expected heterobimetallic complex similar to previous studies.[73,103] More calculations are required to fully determine the

mechanism by which CO binds and exchanges in **5**. While a dissociative mechanism has currently been ruled out in favor of an interchange mechanism, the process by which the CO ligands exchange within the molecule is still uncertain. Additional experimental studies conducting the ^{13}CO exchange in various solvents could help clarify the role of the solvent in determining the $^{13}CO/^{12}CO$ exchange behavior. Specifically, the inclusion of an additional protic solvent could establish whether hydrogen bonding plays a significant role in producing the results seen in MeOH.

CHAPTER IV

UNUSUAL SPIN PROPERTIES OF AN IRON NITROSYL-NICKEL DITHIOLENE DIMER

4.1 Introduction

The ability to store and retrieve electrons to and from a stable molecule is the foundation of efforts to develop better redox catalysts, single molecule magnets, or materials for magnetic storage that can utilize the multiple electronic states generated by the spin coupling of multiple electrons.[118–123] The presence of multiple unpaired electrons within a metal complex for these purposes is a feat usually accomplished synthetically with an f-block element or a combination of high spin first row transition metals with redox active ligands such as bipyridine or nitrosyl.[121,124–126] The expansion of redox active ligands to metalloligands allows for the investigation of more complex electronic structures and reactivities. It also inspires synthetic efforts for the development of complexes designed to replicate the active sites of bimetallic enzymes such as the [FeFe]- and [NiFe]-hydrogenases and the Mo/Cu dependent CO-dehydrogenase among others. These enzymes accomplish the storage of electrons through the use of iron-sulfur clusters.[127,128] $[Fe_4S_4]$ clusters in particular are known to possess multiple redox states and the reduced $[Fe_4S_4]^{3-}$ form can possess different ground state configurations varying from $S = {}^{1}/_{2}$ to $S = {}^{7}/_{2}$.[129,130] Metalloligands offer the opportunity to replicate the redox and spin properties of these iron-sulfur clusters while providing easier routes to synthetic modification.

The dithiolene unit has been used extensively in organometallic chemistry to synthesize metal bis(dithiolene) complexes with intriguing redox, chemical, and optical

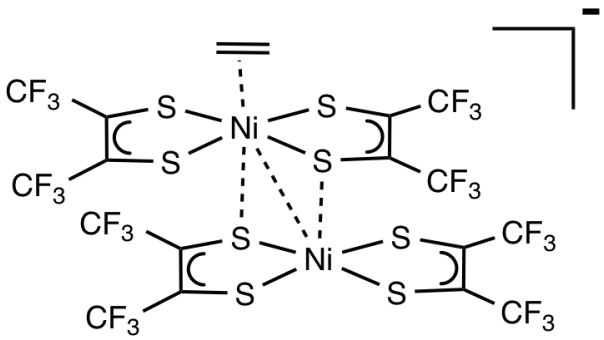

Figure 37 Reduced dimeric intermediate caluclauted by DFT and proposed to be involved in the addition of ethylene to nickel bis(dithiolene) complexes.

properties derived from the non-innocence of the dithiolene ligand.[131–133] It has been shown that nickel (bis)dithiolene complexes react with ethylene to form a cis-interligand adduct in which the ethylene forms a new connection between two of the dithiolene sulfurs.[134,135] This process is reversible and shows potential for practical use in olefin purification. A calculated mechanism detailed how the symmetry forbidden reaction can occur through a reduced bimetallic intermediate featuring a diamond Ni_2S_2 core, **Figure 37**.[136] Related palladium-dithiolene complexes do not form a dimer but instead a hexametric cubic structure with the dithiolene ligands again serving to bridge the multiple metal cetners.[137]

In the course of synthetic efforts to produce organometallic complexes with multiple stable redox levels, a heterobimetallic complex has been synthesized and its

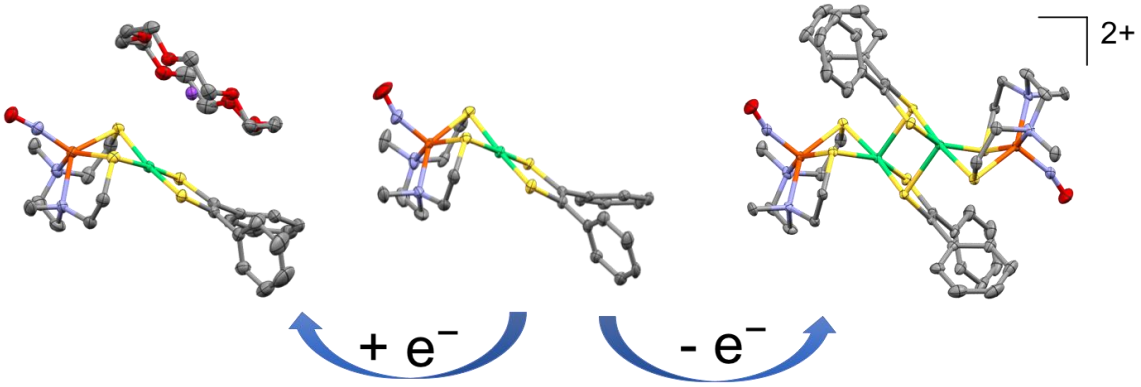

Figure 38 XRD structures of [Fe(NO)-NiS] (center) along with its reduced (left) and oxidized (right) forms.

physical properties characterized by my coworker Manuel Quiroz. The Fe-Ni features nickel dithiolene bound to a Fe-NO unit contained within a N_2S_2 ligand field. This complex was isolated and characterized in three different redox states by XRD, **Figure 38**. Several intricacies have been noted within the series for which computational studies were required for understanding; they include the following:

1) Calculation of vibrational modes for assignment of multiple bands in the solution IR spectrum, which displayed a solvent-dependent dimer-monomer equilibrium;
2) Deconvolution and assignment of the magnetic properties of the oxidized product which is dimeric, $[Fe(NO)\text{-}NiS]_2^{2+}$, in the solid state and in less polar solvents;
3) Address of the fundamental factors and their magnitude that drive the formation of the dimer and the Ni_2S_2 core.

Such computational studies and results are presented below in sections **4.2 – 4.4**.

4.2 Spectroscopic properties and equilibrium of [Fe(NO)-NiS] and $[Fe(NO)\text{-}NiS]_2^{2+}$

The solution IR spectrum of $[Fe(NO)\text{-}NiS]_2^{2+}$ shows two *ν*(NO) bands at 1738 cm^{-1} and 1777 cm^{-1} upon dissolving pure crystals in organic solvent, **Figure 39**. This contrasts to the single band that was observed at 1734 cm^{-1} in the solid state. This led to the hypothesis that the dimer, $[Fe(NO)\text{-}NiS]_2^{2+}$, dissociates into two monomers, $[Fe(NO)\text{-}NiS]^+$, in solution. The DFT calculated *ν*(NO) stretches for the monomer and dimer were

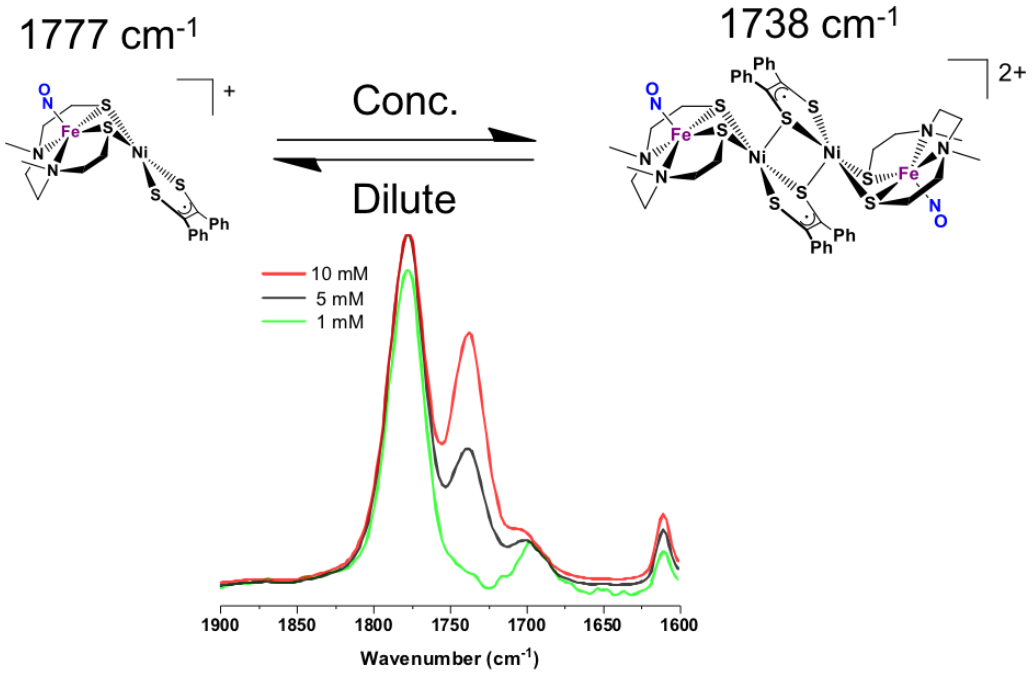

Figure 39 Normalized IR spectra after solvation of $[Fe(NO)\text{-}NiS]_2^{2+}$ in THF showing equilibrium shift to $[Fe(NO)\text{-}NiS]^+$ at lower concentrations.

found to be 1782 cm^{-1} and 1718 cm^{-1} in solution respectively. This corroborates the experimental assignment of the higher wavenumber band at 1777 cm^{-1} to the $[Fe(NO)\text{-}NiS]^+$ monomer due to the disappearance of the 1738 cm^{-1} band at lower concentrations.

There is only one band for the $[Fe(NO)\text{-}NiS]_2^{2+}$ dimer because the symmetric stretch is dipole forbidden so only the asymmetric stretch is detectable by IR spectroscopy.

An expanded list of IR values in various solvents is presented in **Table 1**. The *ν*(NO) values were calculated with two different methods for the monomer. The first, labeled as 'Single Point' in **Table 1**, took the gas phase optimized structure of the cationic monomer and then used that geometry for additional single point frequency calculations in additional solvents. The other method, labeled as 'Optimized' in **Table 1**, optimized the

Table 1 Calculated IR signals for the *ν*(NO) signal of $[Fe(NO)\text{-}NiS]^+$ and $[Fe(NO)\text{-}NiS]_2^{2+}$ in various solvents. Experimental values are given where available.

	ν(NO) Band (cm^{-1})						
	Monomer			Dimer[c]			
	Experimental	Single Point[a]	Optimized[b]	Experimental	Single Point	Solvent Polarity	Donor Number
MeOH	N/A	1744	1770	N/A	1675	0.762	19.0
MeCN	1786	1772	1787	1738	1701	0.460	14.1
DMSO	N/A	1775	1787	N/A	1703	0.444	29.8
DCM	1782	1777	1788	1747	1706	0.309	1.0
THF	1777	1782	1788	1738	1718	0.207	20.0
Et2O	1774	1786	1790	1743	1736	0.117	19.2

[a] 'Single Point' values are from frequencies calculations performed on the same gas phase optimized geometry but in different solvents.
[b] 'Optimized' values are from frequency calculations performed at the optimized geometry for that solvent.
[c] Solid state IR for $[Fe(NO)\text{-}NiS]_2^{2+}$ has single band at 1734 cm^{-1}.

monomer geometry in each solvent and then calculated the IR bands. The DFT values agree well in both cases with unsigned mean errors of 9 cm^{-1} and 8.5 cm^{-1} for the single point and optimized values respectively. For the dimer, the IR values were determined using a modified single point method. The IR values for the dimer have an unsigned mean error of 26 cm^{-1}, larger than either method for the monomers. The *ν*(NO) values increase in wavenumber in less polar solvents for both the monomer and dimer in the single-point calculations but experimentally the monomer shows the opposite trend and the dimer

appears to have no trend at all.[115] We are currently investigating possible causes for this discrepancy. Because the monomer band does not trend with the donor number of each solvent, we conclude that the dimer is not directly cleaved by solvent molecules directly inserting into the Ni-S bonds but rather the dimer dissociates due to strong dipole-dipole interactions with the solvent.[138] It is expected that the experimental equilibrium values will trend with the solvent polarities and corroborate this hypothesis.

The calculations predict that at room temperature in solution the dimer complex will be a triplet ground state and the monomer will be a BS singlet. The cleavage of the triplet dimer to two equivalents of BS singlet monomer in solution was found computationally to be thermodynamically favorable with a free energy change, $\Delta G°$, of -12.6 kcals/mol. The calculated enthalpy and entropy changes are $\Delta H° = 1.6$ kcals/mol and $\Delta S° = 47.9$ cal/mol•K respectively. The signs for the enthalpy and entropy align with expectations for the dissociation of the dimer in to two monomers as energy is required to is break both Ni-S bonds in the diamond core and experiments indicate the equilibrium shifts to produce more dimer at lower temperatures. The calculated enthalpy change is in good agreement with 6.5 kcals/mol $\Delta H°$ that was determined experimentally by measuring the difference in IR absorbance of the two species as a function of the temperature. Attempts to decipher the bonding interactions in the Ni_2S_2 core proved unsuccessful due to the extensive delocalization of electron density across the nickel atoms and dithiolene ligands. Further calculations using Atoms in Molecules (AIM) or NBO could prove insightful in where the nature of the bonds holding the dimer together.

4.3 Magnetic properties of $[Fe(NO)\text{-}NiS]_2^{2+}$

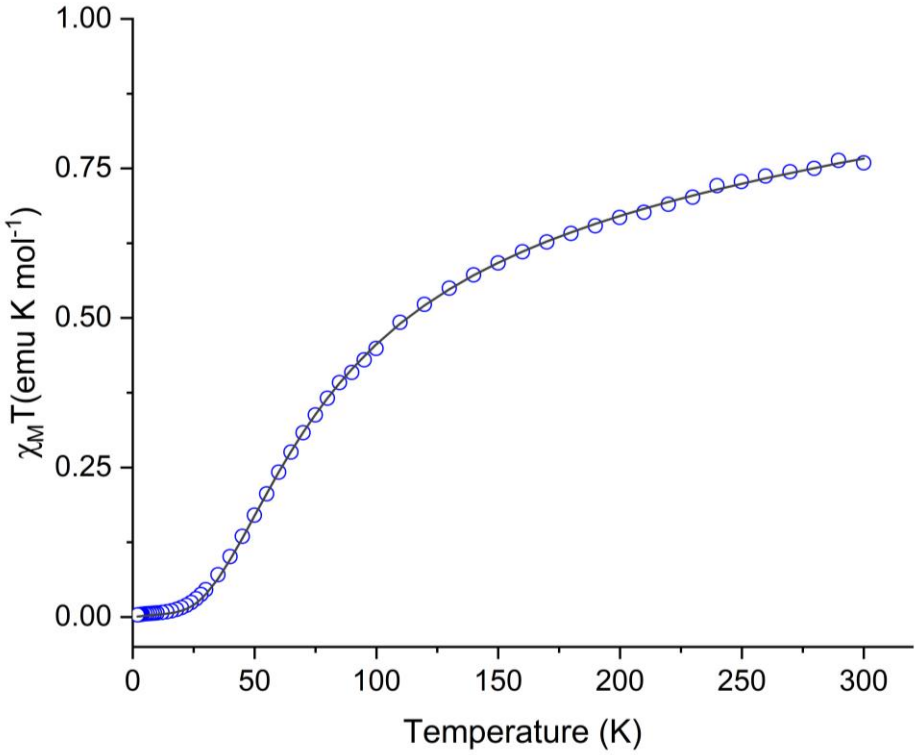

Figure 40 Variable temperature susceptibility measurements for $[Fe(NO)\text{-}NiS]_2^{2+}$ between 2 and 300 K with a 0.1 T field. Figure was obtained by Dr. Mohamed Saber using freshly prepared crystalline samples in an applied magnetic field of 1000 Oe on a Quantum Design SQUID, Model MPMS with a 7 T magnet.

The $[Fe(NO)\text{-}NiS]_2^{2+}$ dimer also possessed intriguing magnetic properties which were measured by Dr. Mohamed Saber using direct current molar magnetic susceptibility on a SQUID, **Figure 40**. The $\chi_m T$ value goes to 0 at low temperatures indicating a S=0 singlet ground state for the molecule. As the temperature increases to a maximum value of 0.76 emu K mol^{-1} at room temperature consistent with a system of two weakly-interacting radicals. This raises the question of where these two radicals are located within the dimer as the system could have a total of four unpaired electrons with two on each of the FeNO units and two on each dithiolene. This question of electronic structure created

an opportunity for elucidation by DFT calculations to determine the difference in energy of the spin states and the location of the unpaired electrons.

A four-radical system like $[Fe(NO)\text{-}NiS]_2^{2+}$ will have a total of six discrete spin states: two singlets, three triplets, and a quintet. Of the six possible states, only four single determinant solutions for the dimer were found computationally using single point calculations on the XRD geometry, a low-energy broken-symmetry (BS) singlet, a triplet,

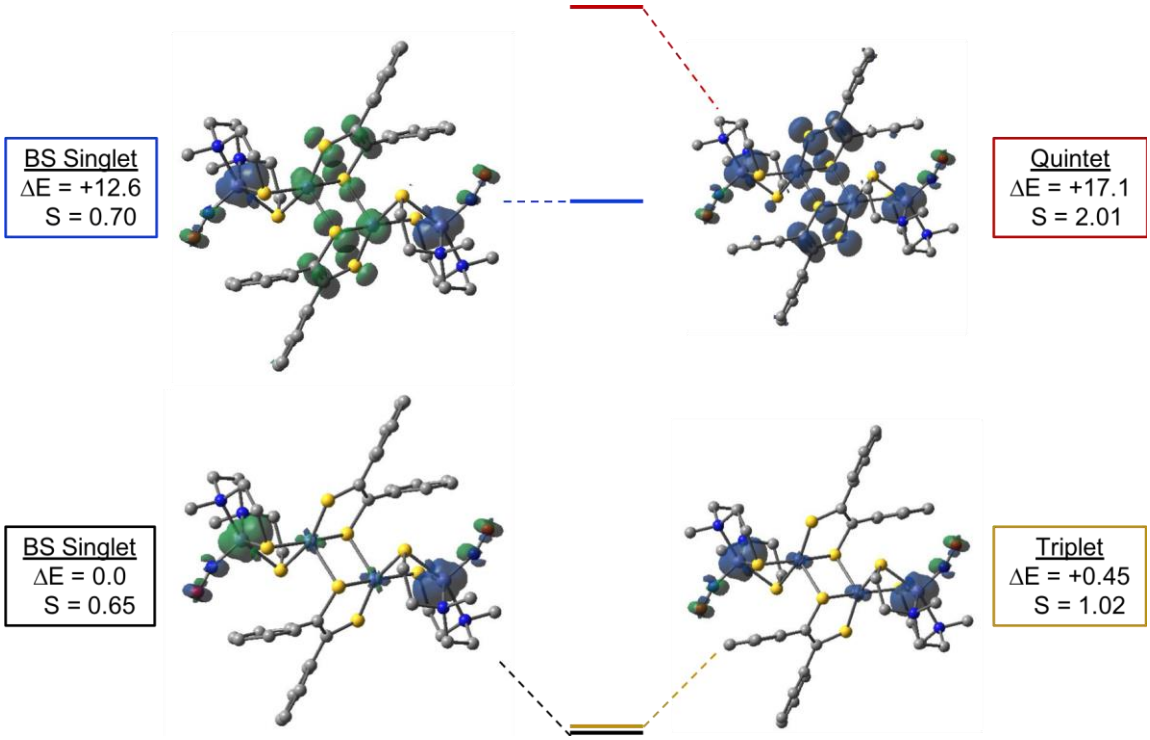

Figure 41 DFT calculated spin ladder of $[Fe(NO)\text{-}NiS]_2^{2+}$. Values are referenced to the projected energy of the low-energy BS singlet to account for the spin contamination in the calculation.

a high-energy BS singlet, and the quintet state, **Figure 41**. The DFT calculations converged to essentially correct spin states for the quintet and triplet, but the BS singlet states are highly contaminated single determinant results (S = 0.65 and 0.70) and not exact singlet states (S = 0). However, because of the strong coupling of the nickel-dithiolene

units, the minimally contaminated low-energy BS triplet can be used to correct the low-energy BS singlet's energy, via the projection formula developed by Yamaguchi that determines the correct energy of the singlet state by removing from the BS singlet the spin contamination from the triplet.[139]

The two low-energy determinants (BS singlet and triplet) feature a core with the two dithiolene radicals antiferromagnetically coupled. The BS triplet is only 0.45 kcals/mol higher in energy than the projected energy of the low-energy BS sing let indicating weak coupling between the two outer $\{Fe(NO)\}^7$ units. The coupling constant, J, was calculated to be -77 cm^{-1} which is good agreement to the experimental value of 51±3 cm^{-1}. The two higher energy determinants are an BS determinant (which is $M_S = 0$, but is contaminated by higher-energy triplets and the quintet) at +12.3 kcals/mol above the ground state and a quintet state at +16.9 kcals/mol. The large energy difference between the low-energy determinants. where the dithiolene core is singlet coupled, and the high energy ones, where it is triplet coupled, indicate the strength of the antiferromagnetic coupling between the nickel-dithiolene units that hold the dimer together.

4.4 A linear H_4 model for the spin states of $[Fe(NO)\text{-}NiS]_2^{2+}$

It was hypothesized that a simple model of the $[Fe(NO)\text{-}NiS]_2^{2+}$ complex could elucidate where the missing states fit within the spin ladder of $[Fe(NO)\text{-}NiS]_2^{2+}$. The simplest depiction of an actual molecular four-spin system is four hydrogen atoms, so a linear H_4 molecule should serve as a good model for $[Fe(NO)\text{-}NiS]_2^{2+}$. The H_4 model

contains two distances: R_1, the distance between the outer hydrogen atoms and their nearest inner neighbor, and R_2, the distance between the two inner hydrogen atoms.

To benchmark the R_1 distance, full configuration interaction (CI) calculations were performed on H_2 at various H-H distances until a distance was found where the singlet-triplet gap for H_2 was equal to the gap for the cation monomer, $[Fe(NO)\text{-}NiS]^+$. The value of the singlet-triplet gap for $[Fe(NO)\text{-}NiS]^+$ when optimized in dichloromethane (DCM) as calculated to be 1.662 kcals/mol. An H-H distance of 2.65 Å for the H-H bond in H_2 gives a singlet-triplet gap of 1.683 kcals/mol in excellent agreement with the projected value for the singlet-triplet gap in the monomer cation. The singlet-triplet gap for $[Fe(NO)\text{-}NiS]^+$ at its solid-state geometry in the $[Fe(NO)\text{-}NiS]_2^{2+}$ XRD structure was found to be 4.166. An H-H distance of 2.39 Å gives a singlet-triplet gap of 4.173 again in excellent agreement with the projected value. The R_2 distance was benchmarked by setting the R_1 distances to either 2.65 Å or 2.39 Å and scanning the R_2 distance until the energy between the ground state singlet (GSS) to the quintet state matched the DFT calculated value from $[Fe(NO)\text{-}NiS]_2^{2+}$ of 17.10 kcals/mol, the energy difference between the projected energy of its BS singlet and its quintet. An R_2 distance of 1.985 Å with an R_1 distance of 2.65 Å and an R_2 distance of 2.035 Å with an R_1 distance of 2.39 Å both gave a GSS-quintet gap of 17.06 kcals/mol, in excellent agreement with the large molecule.

A comparison of the final spin ladders for $[Fe(NO)\text{-}NiS]_2^{2+}$ and the linear H_4 molecule is shown in **Figure 6**. The H_4 model based on the optimized monomer geometry has a similar low energy triplet at +0.10 kcals/mol compared to $[Fe(NO)\text{-}NiS]_2^{2+}$ at +0.45 kcals/mol. The high-energy singlet in H_4 is +2.0 kcals/mol higher in energy than the

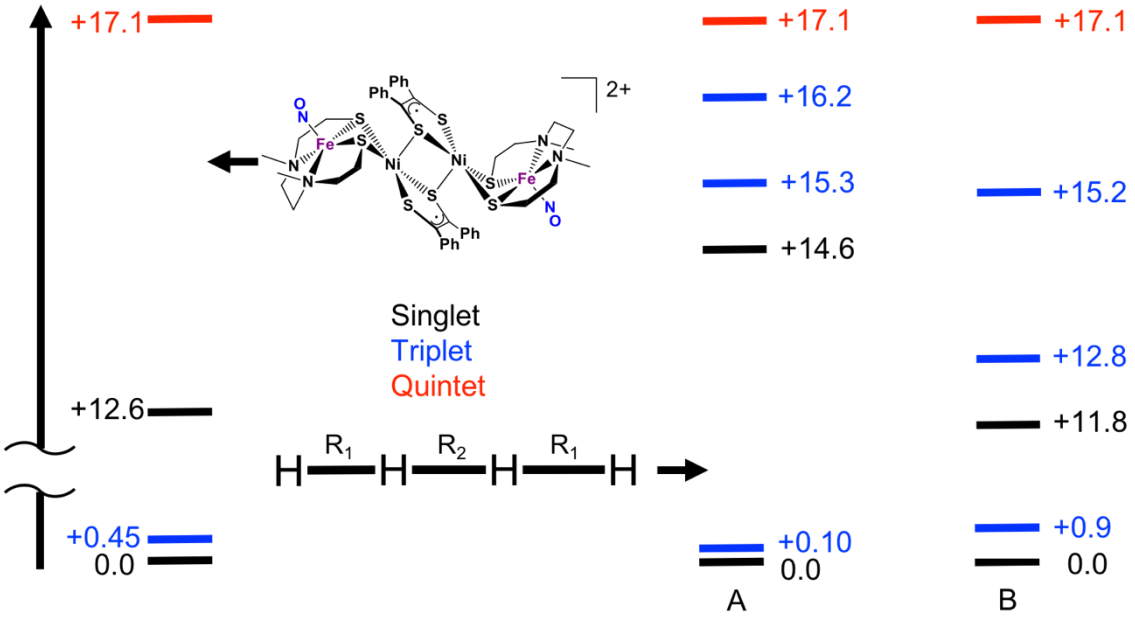

Figure 42 DFT calculated spin ladders for $[Fe(NO)\text{-}NiS]_2^{2+}$ and linear H_4. Column A for H_4 is based on a H_2 benchmark to the singlet-triplet gap of the optimized monomer in solution. Column B for H_4 is based on the singlet-triplet gap for the monomer using its geometry in the dimer XRD structure. All energy values are in kcals/mol.

related high-energy BS M_s=0 determinant in $[Fe(NO)\text{-}NiS]_2^{2+}$. The two additional triplet states for H_4 lie between the high energy singlet and quintet at +15.3 and +16.2 kcals/mol. When the H_4 model is based on the geometry of the monomer in the $[Fe(NO)\text{-}NiS]_2^{2+}$ XRD structure, the high energy states are less tightly grouped and the low-energy triplet shifts towards higher energy but all of the states retain their order.

To gain a better understanding of how the two distance R_1 and R_2 affect the spin ladder shown in **Figure 42**, calculations were performed where the R_1 and R_2 distances

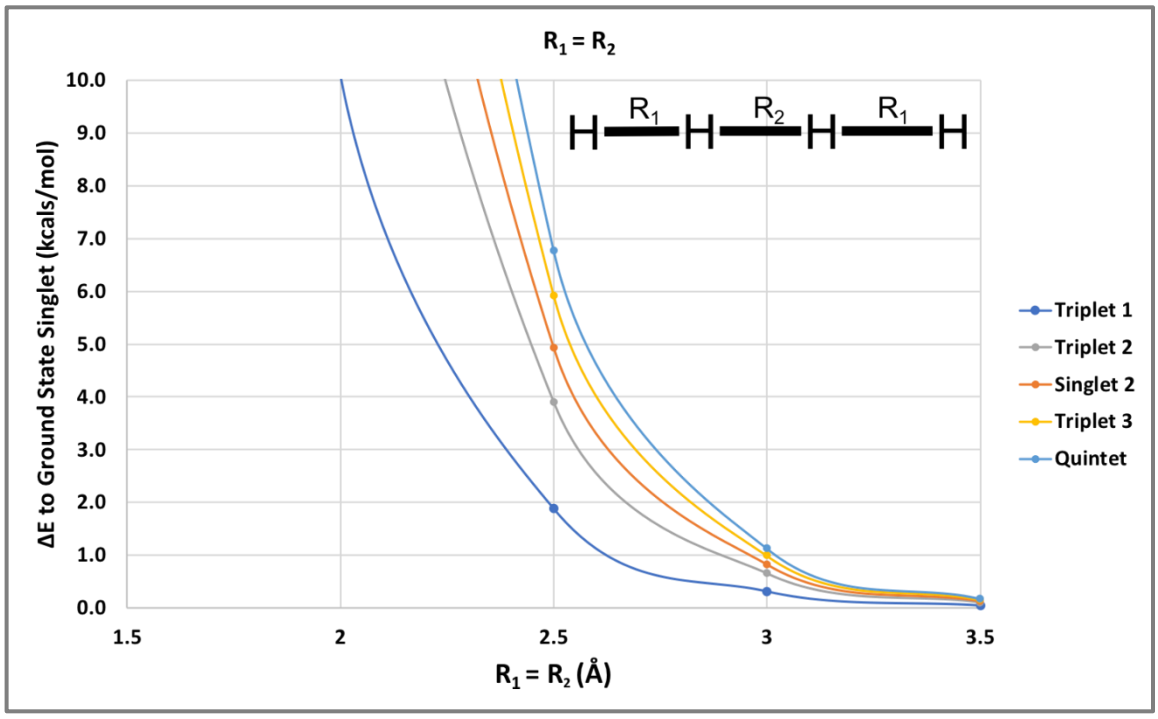

Figure 43 Energy difference between spin states in H_4 related to distance between atoms when R_1=R_2=2.5 Å.

were varied to see how the electronic coupling changes between the radicals and orders of the excited spin states relative to the GSS. **Figure 43** shows the case for R_1= R_2 where at long distances differences go towards 0 as the H_4 molecule begins to separate into four separate hydrogen atoms which have no coupling between them and no barrier to changing spin. As R_1 and R_2 shorten the other states rise in energy where the triplet arising from radicals on the two distance Hs remains somewhat lower in energy that the other four states.

The behavior changes when one bond distance, R_1, is held constant at 2.5 Å and the other, R_2, is varied, **Figure 44**. At long distances the model is equivalent to two separate H_2 molecules with a low energy GSS (both H_2 molecules in their singlet states), a pair of higher energy triplet states around 2.8 kcals/mol (one H_2 molecule in its singlet

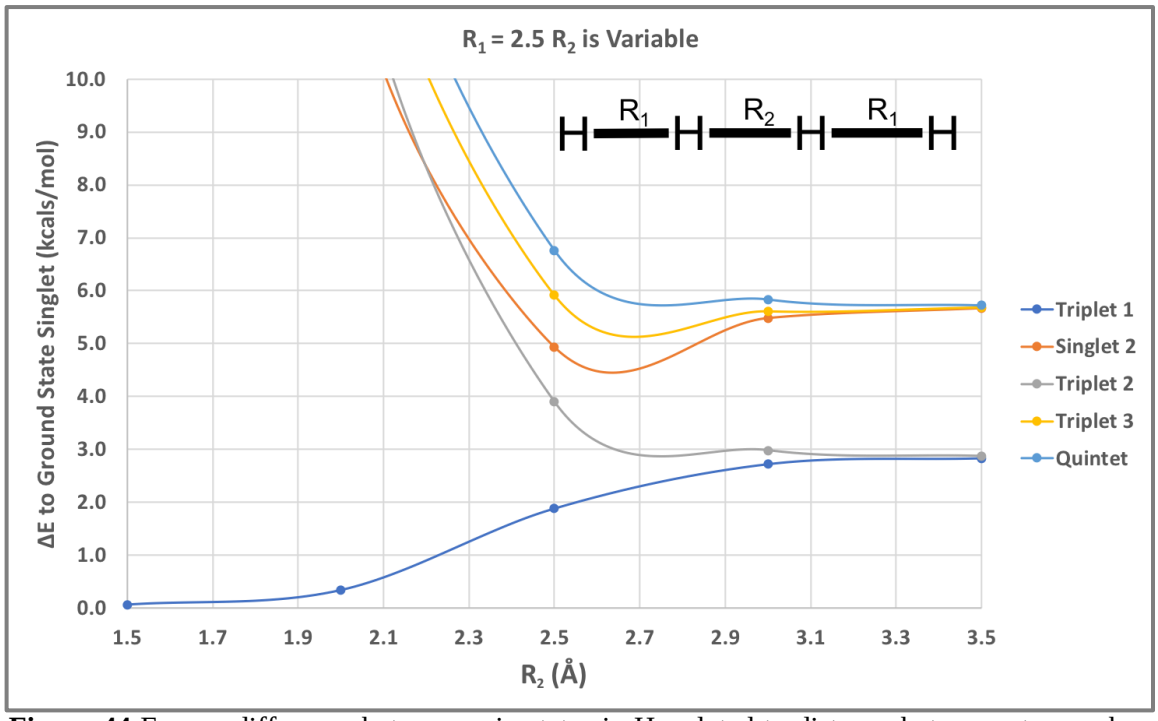

Figure 44 Energy difference between spin states in H_4 related to distance between atoms when R_1=2.5 Å and R_2 varies from 1.5-3.5 Å.

state and the other H_2 molecule in its triplet state), and a singlet, a triplet, and a quintet grouped together at 5.7 kcals/mol (both H_2 molecules in their triplet states). As the R_2 distance decreases and the two H_2 molecule are brought together, the two lowest energy triplets split with one going to toward the energy of the GS and the other going towards higher energies and undergoing a state crossing with the high-energy singlet at about R_2 = 2.2 Å. The low-energy singlet/triplet separation represents the coupling between the two outer hydrogens which experience minimal coupling as they are separated by a distance from each other of 6.5 Å and from their nearest neighbor by 2.5 Å. The other states are all moving to significantly higher energy because the two inner electrons involved in these states and are triplet coupled.

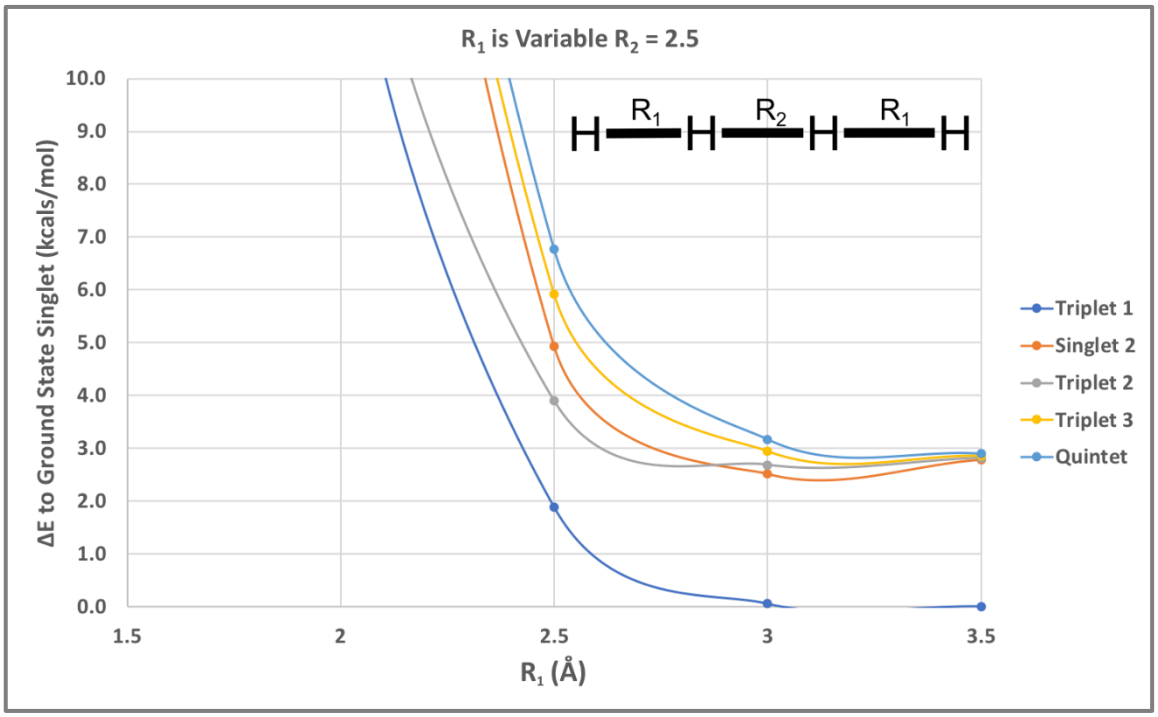

Figure 45 Energy difference between spin states in H_4 related to distance between atoms when R_1=2.5 Å and R_2 varies from 1.5-3.5 Å.

When the opposite situation is plotted and R_1 is varied while R_2 is held constant the data represents two hydrogen atoms approaching an H_2 molecule from a long bond distance of 2.5 Å, **Figure 45**. At long values of R_1 the first triplet excited state is nearly degenerate with the GSS due to the long distance, 9.5 Å, between the outer two hydrogen atoms. The other high-energy spin states are grouped together around 2.9 kcals/mol, which is the energy needed to change coupling of the inner Hs from singlet to triplet, as the distance to the outer electrons is too great for any appreciable coupling. As R_1 decreases all of the spin states increase in energy with the two lower energy triplets grouped together and the high-energy triplet, high-energy singlet, and quintet states grouped together.

4.5 Computational Methodology

The crystal structures of [Fe(NO)-NiS] and $[Fe(NO)\text{-}NiS]_2^{2+}$ were used as the starting point geometries for all calculations. For the IR comparisons in various solvents the $[Fe(NO)\text{-}NiS]^+$ structure was optimized in the gas phase as an open shell singlet using Gaussian 16 with the TPSSTPSS functional with a 6-311++G(d,p) basis set on the nonmetal atoms and a 6-311+G basis set on nickel and iron.[85] The IR values were then obtained in each solvent by performing single point frequency calculations on the optimized gas phase geometry using the SMD solvation model. For comparison, the monomer values were also calculated by optimizing the geometry in each solvent and then performing the frequency calculations in that solvent. The dimer structure could not be optimized in the gas phase so instead it was optimized as a triplet and BS singlet in dichloromethane with methyl groups replacing the phenyls to make the calculations easier. This optimized geometry was then used in single point frequency calculations in the chosen solvents using the same functional and basis sets as the monomer. The triplet was found to be the ground state for the dimer in the solution calculations.

The thermodynamic values for the dimer to monomer dissociation were obtained using values from the DCM optimized dimer triplet and DCM optimized monomer BS singlet with methyl groups in place of the phenyls for both. The free energy and enthalpy values for the monomer were both corrected using the spin projection method and the entropy was found using $\Delta G=\Delta H-T\Delta S$.

For the spin ladder of $[Fe(NO)\text{-}NiS]_2^{2+}$, single point calculations were performed directly from the $[Fe(NO)\text{-}NiS]_2^{2+}$ XRD structure with the same functional and basis sets

as previous calculations. All CI calculations on H_2 and linear H_4 were performed in ORCA version 4.2.1 using a STO-6G basis set.[140,141] The distance between the outer two hydrogen atoms in H_4, R_1, was benchmarked by finding the distance at which H_2 possessed the same singlet-triplet gap as $[Fe(NO)\text{-}NiS]^+$. This benchmarking was done to the singlet triplet gap in solvent optimized $[Fe(NO)\text{-}NiS]^+$ as well the singlet-triplet gap for the geometry of $[Fe(NO)\text{-}NiS]^+$ when taken from the XRD structure of $[Fe(NO)\text{-}NiS]_2^{2+}$. Full CI calculations were then performed on H_4 where R_2 was varied using the previously determined R_1 values until the energy difference for the quintet state and the GSS matched the DFT calculated value.

4.6 Conclusions

The $[Fe(NO)\text{-}NiS]_2^{2+}$ dimer features intriguing magnetic and solution-phase properties. Computational and experimental methods have determined that in solution the dimer and its monomer cation are in an equilibrium that favors the monomeric form in solution. The dimer is held together by a pair of weak Ni-S bonds between the nickel-dithiolene units from each monomer that stabilizes through strong antiferromagnetic coupling the radicals from each dithiolene backbone. From the weak coupling between the distant $\{Fe(NO)\}^7$ units, the $[Fe(NO)\text{-}NiS]_2^{2+}$ dimer has a singlet ground state and low-lying triplet state that become nearly equally occupied at room temperature. The four radical sites contained in the complex make it and related systems an intriguing candidates for further studies on their magnetic properties as a single molecule magnets (SMM) as most SMM's use the rarer and more expensive lanthanide elements.[142] The weak coupling

between the two $\{Fe(NO)\}^7$ units may be tunable by oxidation either one or both to $\{Fe(NO)\}^6$ units as trivalent first row metals have been shown to produce stronger couplings than their divalent analogs.[143]

The radical properties of the $[Fe(NO)\text{-}NiS]_2^{2+}$ dimer and related systems may also have some use in developing better materials for quantum computing or superconductors.[144] Recent efforts have indicated that two dithiolene ligands have potential to function as an organic electron spin qubit when bound on either side of a diamagnetic metal center such as a square planar d^8 nickel atom.[145] The spacing of the four radicals creates differences in coupling and a spin ladder that may have properties similar to some Cu^{II} materials that have been investigated as materials for superconductors. One example are the spin-ladder cuprates with their radicals arranged in an approximate square that share properties of both 1D antiferromagnets and 2D square-lattices and can become superconductors after hole doping.[146] A different configuration is found in copper oxalates which were recently shown to exist as an infinite spin chain instead of a series of non-interacting dimers.[147] Experimental determination whether the $[Fe(NO)\text{-}NiS]_2^{2+}$ dimer has any long range magnetic communication can determine if the complex has any potential uses as a magnetic material.

CHAPTER V

CONCLUSIONS

5.1 Future Directions

There are still some loose ends in the work previously presented. Below are some thoughts on possible routes another researcher could take moving forward.

5.1.1 [NiFeS]- and [NiFeSe]-H_2ase Models and Their Oxygen Reactivity

The largest missing piece remains the mechanism for O_2 reacting with the reduced species. The sulfur mechanism presented in **Figure 19** is missing transition states in the first half of the mechanism. One hurdle in locating these transition states is the necessity of a spin crossover event that can be difficult to find through DFT though a reasonable estimate should be possible. The mechanism for the selenium containing species is also necessary to determine where the two mechanisms divulge. One current hypothesis is that somewhere along the mechanistic path an intermediate for the selenium containing complex is significantly higher in energy than its sulfur containing analog. This would disfavor reactions progress towards the doubly-oxygenated product and instead favor production of the singly-oxygenated product. Another hypothesis is that the doubly-oxygenated form of the selenium complex is formed and then undergoes comproportionation to form two equivalents of the singly-oxygenated species. DFT calculations to find the transition state for this oxygen transfer process could determine if it is a feasible process.

The small molecule benchmarking showed that MN12-L is the best choice, at least among the diverse group of functionals tested, for computational studies into the bonding interactions between oxygen and the heavier chalcogens sulfur and selenium. This should allow for more detailed investigations on the [NiFe]-H_2ase models synthesized and provide inspiration for improved complexes in terms of both catalytic production and oxygen tolerance. MN12-L could also prove useful in performing high level QM/MM calculations on the [NiFe]-H_2ase active site to understand the reactivity of O_2 within the enzyme. Of particular interest is the mechanism by which O_2 appears to selectivity oxidize the terminal thiolate or selenoate in [NiFeSe]-H_2ases instead of the bridging thiolates or the nickel center.

5.1.2 Carbon Monoxide Exchange in Mn_2H_2ema

The ^{13}CO exchange behavior is still not fully understood for the *Mn_2H_2ema* complex. It is currently believed that a transition state similar to the one seen in **Figure 34** should exist for the intermediate found in **Figure 35**. Additional work is needed to locate this transition state to complete the mechanism for CO addition, scrambling, and removal.

5.1.3 $[Fe(NO)\text{-}NiS]_2^{2+}$ Magnetic Properties

The presence of the low-lying triplet excited state for $[Fe(NO)\text{-}NiS]_2^{2+}$ could be modified to create a controllable singlet/triplet spin change. The H_4 model calculations seen in **Figures 44-46** show how modifying the length of the ligands between the metal centers could be used to precisely control the energy of the spin crossover event. The

distance between the nickel-dithiolene units could be controlled by substituting the phenyl group on the dithiolene for groups with different levels of steric bulk. Electronic effects on the coupling between the two dithiolene units could be investigated by substitution at different positions on the phenyl ring with electron donating or withdrawing groups. Different versions of the complex could also be synthesized in which the Fe-NO is replaced with Co-NO or the nickel is replaced with a heavier Group 10 element such as palladium or platinum.

5.2 Outlook

As the world's energy production shifts towards more renewable sources to combat climate change, biologically inspired catalysts will be at the center of innovative research efforts. These catalysts will seek to tackle the problem from two different directions. The first is trying to directly combat current greenhouse gas levels by converting these molecules into more useful products. Some of the most intense focus is on developing catalysts designed to reduce CO_2 or partially oxidize methane (CH_4) into products such as CO, carbonate, formate, methanol. Some success has been found in using catalysts based on carbon monoxide dehydrogenase, methane monooxygenase, and carbonic anhydrase to name a few.[148–150]

The other method for enzyme inspired catalyst development is focused on designing catalysts that replicate the H_2 generation ability of hydrogenase enzymes. Future designs should seek to combine the H_2 production capability of the [FeFe]-H_2ases with the oxygen tolerance shown by the [NiFeSe]-H_2ases to create catalysts that can operate

under milder conditions. Until recently the only forms of [FeFe]-H_2ase known to possess an oxygenated form were found in sulfate-reducing bacteria such as *Desulfovibrio desulfuricans* (DdHydAB) and *Desulfovibrio vulgaris* (DvHydAB). These forms lose roughly 50% of their activity after exposure to aerobic environments but prevent full decomposition by HS^- binding to the H-cluster and inducing a charge rearrangement.[151] An [FeFe]-H_2ase capable of full activity recovery, *Clostridium beijerinckii*, has recently been isolated and DFT investigations provided evidence that its oxygen tolerance was due to protection of the distal iron center by a hydroxide or deprotonated cysteine ligand bound to the open site on the "rotated" iron.[152,153] The possibility of more oxygen tolerant hydrogenases provides an opportunity to develop more robust catalysts for hydrogen production by incorporating motifs already proven to work in nature. An example of this are the [FeFe]-H_2ase model complexes by Darensbourg and Dey that incorporated secondary sphere effects to replicate the O_2 to H_2O reduction pathway suggested from the calculations by Blumberger *et al*.[154,155] These catalysts were able to catalyze the HER at overpotentials of less than 200 mV in aqueous media at near neutral pH; they regained full activity after exposure to O_2 by reducing the bound O_2 to H_2O.

The use of DFT to suggest mechanisms and intermediates for new catalysts is vital where experimental methods would require too many resources, too long, or are simply impossible with current technology. The best source for catalyst design inspiration is found in the active sites of enzymes which are nature's catalysts. Some groups have already begun working in this area such as Qiu *et al*. who used a truncated active site model to explore the difference between the **Ni-A** and **Ni-B** states of the [NiFe]-H2ase

active site.[156] They found that the **Ni-A** state is very stable and this contributes to its more difficult reactivation though the fundamental reasons for this stability are still unclear. Another example is that of Breglia, *et a*l. who have published a small body of theoretical work on [NiFe]-H_2ase oxygenation and utilized rather large models of the active site to understand how the secondary protein environment influenced the results.[90,91,157,158] Their work highlights the ways the [NiFe]-H_2ase active site activates O_2 and how it electrochemically reactivates itself once oxygenated by eliminating the oxygen atoms as water molecules. This knowledge of the enzyme reactivity gained by computational chemistry can provide insights for the design of a new generation of more faithful biomimetics that better replicate the selectivity, robustness, and self-repairing capabilities seen in nature. These catalysts will then lead to better performing fuel cells and electrolyzers that will not only be highly efficient but also able to incorporate the oxygen tolerance abilities seen in the enzymes and certain model complexes.[27]

Computational methods are constantly being developed and modified and as their sophistication improves the capabilities are DFT are increased. Increased parameterization based on new experimental data allows for new systems to be analyzed where previous methodology was insufficient. It is certain that additional rungs will be added to the "Jacob's Ladder of DFT" as new marks of accuracy are achieved by more advanced functionals. Shortcomings such as the inability to properly describe complicated wavefunctions which lead to the inability to fully calculate the spin ladder of $[Fe(NO)\text{-}NiS]_2^{2+}$ may one day be overcome and eliminate the need for smaller and possibly inadequate models. It may also be seen where entire proteins are able to be analyzed at the

quantum mechanical level allowing for a more detailed understanding than is currently possible with molecular mechanical methods.

REFERENCES

(1) Coontz, R. Not So Simple. *Science* **2004**, *305* (5686), 957–957.

(2) Gray, H. B. Powering the Planet with Solar Fuel. *Nat. Chem.* **2009**, *1* (1), 7–7.

(3) Volbeda, A.; Charon, M.-H.; Piras, C.; Hatchikian, E. C.; Frey, M.; Fontecilla-Camps, J. C. Crystal Structure of the Nickel–Iron Hydrogenase from Desulfovibrio Gigas. *Nature* **1995**, *373* (6515), 580–587.

(4) Weber, K.; Krämer, T.; Shafaat, H. S.; Weyhermüller, T.; Bill, E.; van Gastel, M.; Neese, F.; Lubitz, W. A Functional [NiFe]-Hydrogenase Model Compound That Undergoes Biologically Relevant Reversible Thiolate Protonation. *J. Am. Chem. Soc.* **2012**, *134* (51), 20745–20755.

(5) Li, S.; Hall, M. B. Modeling the Active Sites of Metalloenzymes. 4. Predictions of the Unready States of [NiFe] *Desulfovibrio Gigas* Hydrogenase from Density Functional Theory. *Inorg. Chem.* **2001**, *40* (1), 18–24.

(6) Darensbourg, M. Y.; Weigand, W. Sulfoxygenation of Active Site Models of [NiFe] and [FeFe] Hydrogenases – A Commentary on Possible Chemical Models of Hydrogenase Enzyme Oxygen Sensitivity. *Eur. J. Inorg. Chem.* **2011**, *2011* (7), 994–1004.

(7) Zhu, W.; Marr, A. C.; Wang, Q.; Neese, F.; Spencer, D. J. E.; Blake, A. J.; Cooke, P. A.; Wilson, C.; Schroder, M. Modulation of the Electronic Structure and the Ni-Fe Distance in Heterobimetallic Models for the Active Site in [NiFe]Hydrogenase. *Proc. Natl. Acad. Sci.* **2005**, *102* (51), 18280–18285.

(8) Rakowski DuBois, M.; DuBois, D. L. The Roles of the First and Second Coordination Spheres in the Design of Molecular Catalysts for H_2 Production and Oxidation. *Chem Soc Rev* **2009**, *38* (1), 62–72.

(9) Tard, C.; Pickett, C. J. Structural and Functional Analogues of the Active Sites of the [Fe]-, [NiFe]-, and [FeFe]-Hydrogenases. *Chem. Rev.* **2009**, *109* (6), 2245–2274.

(10) Tang, H.; Hall, M. B. Biomimetics of [NiFe]-Hydrogenase: Nickel- or Iron-Centered Proton Reduction Catalysis? *J. Am. Chem. Soc.* **2017**, *139* (49), 18065–18070.

(11) Siegbahn, P. E. M.; Tye, J. W.; Hall, M. B. Computational Studies of [NiFe] and [FeFe] Hydrogenases. *Chem. Rev.* **2007**, *107* (10), 4414–4435.

(12) Tai, H.; Higuchi, Y.; Hirota, S. Comprehensive Reaction Mechanisms at and near the Ni–Fe Active Sites of [NiFe] Hydrogenases. *Dalton Trans.* **2018**, *47* (13), 4408–4423.

(13) Dong, G.; Ryde, U. Protonation States of Intermediates in the Reaction Mechanism of [NiFe] Hydrogenase Studied by Computational Methods. *JBIC J. Biol. Inorg. Chem.* **2016**, *21* (3), 383–394.

(14) Ogata, H.; Mizoguchi, Y.; Mizuno, N.; Miki, K.; Adachi, S.; Yasuoka, N.; Yagi, T.; Yamauchi, O.; Hirota, S.; Higuchi, Y. Structural Studies of the Carbon Monoxide Complex of [NiFe]Hydrogenase from *Desulfovibrio Vulgaris* Miyazaki F: Suggestion for the Initial Activation Site for Dihydrogen. *J. Am. Chem. Soc.* **2002**, *124* (39), 11628–11635.

(15) Ogo, S.; Mori, Y.; Ando, T.; Matsumoto, T.; Yatabe, T.; Yoon, K.-S.; Hayashi, H.; Asano, M. One Model, Two Enzymes: Activation of Hydrogen and Carbon Monoxide. *Angew. Chem. Int. Ed.* **2017**, *56* (33), 9723–9726.

(16) Isegawa, M.; Matsumoto, T.; Ogo, S. Selective Oxidation of H_2 and CO by NiIr Catalyst in Aqueous Solution: A DFT Mechanistic Study. *Inorg. Chem.* **2020**, *59* (2), 1014–1028.

(17) Ulloa, O. A.; Huynh, M. T.; Richers, C. P.; Bertke, J. A.; Nilges, M. J.; Hammes-Schiffer, S.; Rauchfuss, T. B. Mechanism of H_2 Production by Models for the [NiFe]-Hydrogenases: Role of Reduced Hydrides. *J. Am. Chem. Soc.* **2016**, *138* (29), 9234–9245.

(18) Isegawa, M.; Sharma, A. K.; Ogo, S.; Morokuma, K. Electron and Hydride Transfer in a Redox-Active NiFe Hydride Complex: A DFT Study. *ACS Catal.* **2018**, *8* (11), 10419–10429.

(19) Brazzolotto, D.; Gennari, M.; Queyriaux, N.; Simmons, T. R.; Pécaut, J.; Demeshko, S.; Meyer, F.; Orio, M.; Artero, V.; Duboc, C. Nickel-Centred Proton Reduction Catalysis in a Model of [NiFe] Hydrogenase. *Nat. Chem.* **2016**, *8* (11), 1054–1060.

(20) Kishima, T.; Matsumoto, T.; Nakai, H.; Hayami, S.; Ohta, T.; Ogo, S. A High-Valent Iron(IV) Peroxo Core Derived from O_2. *Angew. Chem. Int. Ed.* **2016**, *55* (2), 724–727.

(21) Isegawa, M.; Sharma, A. K.; Ogo, S.; Morokuma, K. DFT Study on Fe(IV)-Peroxo Formation and H Atom Transfer Triggered O_2 Activation by NiFe Complex. *Organometallics* **2018**, *37* (10), 1534–1545.

(22) Lubitz, W.; Ogata, H.; Rüdiger, O.; Reijerse, E. Hydrogenases. *Chem. Rev.* **2014**, *114* (8), 4081–4148.

(23) Beer, L. L.; Boyd, E. S.; Peters, J. W.; Posewitz, M. C. Engineering Algae for Biohydrogen and Biofuel Production. *Curr. Opin. Biotechnol.* **2009**, *20* (3), 264–271.

(24) Hambourger, M.; Gervaldo, M.; Svedruzic, D.; King, P. W.; Gust, D.; Ghirardi, M.; Moore, A. L.; Moore, T. A. [FeFe]-Hydrogenase-Catalyzed H_2 Production in a Photoelectrochemical Biofuel Cell. *J. Am. Chem. Soc.* **2008**, *130* (6), 2015–2022.

(25) Cammack, R.; Frey, M.; Robson, R. *Hydrogen as a Fuel*; Taylor and Francis: London, 2001.

(26) Vincent, K. A.; Parkin, A.; Lenz, O.; Albracht, S. P. J.; Fontecilla-Camps, J. C.; Cammack, R.; Friedrich, B.; Armstrong, F. A. Electrochemical Definitions of O2 Sensitivity and Oxidative Inactivation in Hydrogenases. *J. Am. Chem. Soc.* **2005**, *127* (51), 18179–18189.

(27) Wakerley, D. W.; Reisner, E. Oxygen-Tolerant Proton Reduction Catalysis: Much O_2 about Nothing? *Energy Environ. Sci.* **2015**, *8* (8), 2283–2295.

(28) Baltazar, C. S. A.; Marques, M. C.; Soares, C. M.; DeLacey, A. M.; Pereira, I. A. C.; Matias, P. M. Nickel-Iron-Selenium Hydrogenases - An Overview. *Eur. J. Inorg. Chem.* **2011**, *2011* (7), 948–962.

(29) Buhrke, T.; Lenz, O.; Krauss, N.; Friedrich, B. Oxygen Tolerance of the H2-Sensing [NiFe] Hydrogenase from Ralstonia Eutropha H16 Is Based on Limited Access of Oxygen to the Active Site. *J. Biol. Chem.* **2005**, *280* (25), 23791–23796.

(30) Duché, O.; Elsen, S.; Cournac, L.; Colbeau, A. Enlarging the Gas Access Channel to the Active Site Renders the Regulatory Hydrogenase HupUV of Rhodobacter Capsulatus O2 Sensitive without Affecting Its Transductory Activity: O2 Sensitivity of the Regulatory Hydrogenase HupUV. *FEBS J.* **2005**, *272* (15), 3899–3908.

(31) Fritsch, J.; Lenz, O.; Friedrich, B. Structure, Function and Biosynthesis of O2-Tolerant Hydrogenases. *Nat. Rev. Microbiol.* **2013**, *11* (2), 106–114.

(32) Lenz, O.; Ludwig, M.; Schubert, T.; Bürstel, I.; Ganskow, S.; Goris, T.; Schwarze, A.; Friedrich, B. H2 Conversion in the Presence of O2 as Performed by the Membrane-Bound [NiFe]-Hydrogenase of Ralstonia Eutropha. *ChemPhysChem* **2010**, *11* (6), 1107–1119.

(33) Pandelia, M.-E.; Fourmond, V.; Tron-Infossi, P.; Lojou, E.; Bertrand, P.; Léger, C.; Giudici-Orticoni, M.-T.; Lubitz, W. Membrane-Bound Hydrogenase I from the Hyperthermophilic Bacterium *Aquifex Aeolicus* : Enzyme Activation, Redox Intermediates and Oxygen Tolerance. *J. Am. Chem. Soc.* **2010**, *132* (20), 6991–7004.

(34) Shomura, Y.; Yoon, K.-S.; Nishihara, H.; Higuchi, Y. Structural Basis for a [4Fe-3S] Cluster in the Oxygen-Tolerant Membrane-Bound [NiFe]-Hydrogenase. *Nature* **2011**, *479* (7372), 253–256.

(35) Volbeda, A.; Amara, P.; Darnault, C.; Mouesca, J.-M.; Parkin, A.; Roessler, M. M.; Armstrong, F. A.; Fontecilla-Camps, J. C. X-Ray Crystallographic and Computational Studies of the O2-Tolerant [NiFe]-Hydrogenase 1 from Escherichia Coli. *Proc. Natl. Acad. Sci.* **2012**, *109* (14), 5305–5310.

(36) Vignais, P. M.; Billoud, B. Occurrence, Classification, and Biological Function of Hydrogenases: An Overview. *Chem. Rev.* **2007**, *107* (10), 4206–4272.

(37) Reich, H. J.; Hondal, R. J. Why Nature Chose Selenium. *ACS Chem. Biol.* **2016**, *11* (4), 821–841.

(38) De Lacey, A. L.; Gutiérrez-Sánchez, C.; Fernández, V. M.; Pacheco, I.; Pereira, I. A. C. FTIR Spectroelectrochemical Characterization of the Ni–Fe–Se Hydrogenase from Desulfovibrio Vulgaris Hildenborough. *JBIC J. Biol. Inorg. Chem.* **2008**, *13* (8), 1315–1320.

(39) Parkin, A.; Goldet, G.; Cavazza, C.; Fontecilla-Camps, J. C.; Armstrong, F. A. The Difference a Se Makes? Oxygen-Tolerant Hydrogen Production by the [NiFeSe]-Hydrogenase from *Desulfomicrobium Baculatum*. *J. Am. Chem. Soc.* **2008**, *130* (40), 13410–13416.

(40) Wombwell, C.; Caputo, C. A.; Reisner, E. [NiFeSe]-Hydrogenase Chemistry. *Acc. Chem. Res.* **2015**, *48* (11), 2858–2865.

(41) Garcin, E.; Vernede, X.; Hatchikian, E.; Volbeda, A.; Frey, M.; Fontecilla-Camps, J. The Crystal Structure of a Reduced [NiFeSe] Hydrogenase Provides an Image of the Activated Catalytic Center. *Structure* **1999**, *7* (5), 557–566.

(42) Wombwell, C.; Reisner, E. Synthesis, Structure and Reactivity of Ni Site Models of [NiFeSe] Hydrogenases. *Dalton Trans* **2014**, *43* (11), 4483–4493.

(43) Wombwell, C.; Reisner, E. Synthetic Active Site Model of the [NiFeSe] Hydrogenase. *Chem. - Eur. J.* **2015**, *21* (22), 8096–8104.

(44) Marques, M. C.; Coelho, R.; Pereira, I. A. C.; Matias, P. M. Redox State-Dependent Changes in the Crystal Structure of [NiFeSe] Hydrogenase from Desulfovibrio Vulgaris Hildenborough. *Int. J. Hydrog. Energy* **2013**, *38* (21), 8664–8682.

(45) Volbeda, A.; Martin, L.; Cavazza, C.; Matho, M.; Faber, B. W.; Roseboom, W.; Albracht, S. P. J.; Garcin, E.; Rousset, M.; Fontecilla-Camps, J. C. Structural Differences between the Ready and Unready Oxidized States of [NiFe] Hydrogenases. *JBIC J. Biol. Inorg. Chem.* **2005**, *10* (3), 239–249.

(46) Cracknell, J. A.; Wait, A. F.; Lenz, O.; Friedrich, B.; Armstrong, F. A.; Gray, H. B. A Kinetic and Thermodynamic Understanding of O_2 Tolerance in [NiFe]-Hydrogenases. *Proc. Natl. Acad. Sci. U. S. A.* **2009**, *106* (49), 20681–20686.

(47) Jones, A. K.; Lamle, S. E.; Pershad, H. R.; Vincent, K. A.; Albracht, S. P. J.; Armstrong, F. A. Enzyme Electrokinetics: Electrochemical Studies of the Anaerobic Interconversions between Active and Inactive States of *Allochromatium Vinosum* [NiFe]-Hydrogenase. *J. Am. Chem. Soc.* **2003**, *125* (28), 8505–8514.

(48) Lamle, S. E.; Albracht, S. P. J.; Armstrong, F. A. The Mechanism of Activation of a [NiFe]-Hydrogenase by Electrons, Hydrogen, and Carbon Monoxide. *J. Am. Chem. Soc.* **2005**, *127* (18), 6595–6604.

(49) Radu, V.; Frielingsdorf, S.; Lenz, O.; Jeuken, L. J. C. Reactivation from the Ni–B State in [NiFe] Hydrogenase of Ralstonia Eutropha Is Controlled by Reduction of the Superoxidised Proximal Cluster. *Chem. Commun.* **2016**, *52* (12), 2632–2635.

(50) Armstrong, F. A.; Belsey, N. A.; Cracknell, J. A.; Goldet, G.; Parkin, A.; Reisner, E.; Vincent, K. A.; Wait, A. F. Dynamic Electrochemical Investigations of Hydrogen Oxidation and Production by Enzymes and Implications for Future Technology. *Chem Soc Rev* **2009**, *38* (1), 36–51.

(51) Albracht, S. P. J.; Graf, E.-G.; Thauer, R. K. The EPR Properties of Nickel in Hydrogenase from *Methanobacterium Thermoautotrophicum*. *FEBS Lett.* **1982**, *140* (2), 311–313.

(52) Flores, M.; Agrawal, A. G.; van Gastel, M.; Gärtner, W.; Lubitz, W. Electron−Electron Double Resonance-Detected NMR to Measure Metal Hyperfine Interactions: ^{61} Ni in the Ni−B State of the [NiFe] Hydrogenase of *Desulfovibrio Vulgaris* Miyazaki F. *J. Am. Chem. Soc.* **2008**, *130* (8), 2402–2403.

(53) Horch, M.; Lauterbach, L.; Mroginski, M. A.; Hildebrandt, P.; Lenz, O.; Zebger, I. Reversible Active Site Sulfoxygenation Can Explain the Oxygen Tolerance of a NAD^+ -Reducing [NiFe] Hydrogenase and Its Unusual Infrared Spectroscopic Properties. *J. Am. Chem. Soc.* **2015**, *137* (7), 2555–2564.

(54) Volbeda, A.; Martin, L.; Barbier, E.; Gutiérrez-Sanz, O.; De Lacey, A. L.; Liebgott, P.-P.; Dementin, S.; Rousset, M.; Fontecilla-Camps, J. C. Crystallographic Studies of [NiFe]-Hydrogenase Mutants: Towards Consensus Structures for the Elusive Unready Oxidized States. *JBIC J. Biol. Inorg. Chem.* **2015**, *20* (1), 11–22.

(55) Marques, M. C.; Coelho, R.; De Lacey, A. L.; Pereira, I. A. C.; Matias, P. M. The Three-Dimensional Structure of [NiFeSe] Hydrogenase from Desulfovibrio Vulgaris Hildenborough: A Hydrogenase without a Bridging Ligand in the Active Site in Its Oxidised, "as-Isolated" State. *J. Mol. Biol.* **2010**, *396* (4), 893–907.

(56) Volbeda, A.; Amara, P.; Iannello, M.; De Lacey, A. L.; Cavazza, C.; Fontecilla-Camps, J. C. Structural Foundations for the O2 Resistance of Desulfomicrobium Baculatum [NiFeSe]-Hydrogenase. *Chem. Commun.* **2013**, *49* (63), 7061.

(57) Teixeira, M.; Fauque, G.; Moura, I.; Lespinat, P. A.; Berlier, Y.; Prickril, B.; Peck, H. D.; Xavier, A. V.; Gall, J.; Moura, J. J. G. Nickel-[Iron-Sulfur]-Selenium-Containing Hydrogenases from Desulfovibrio Baculatus (DSM 1743). Redox Centers and Catalytic Properties. *Eur. J. Biochem.* **1987**, *167* (1), 47–58.

(58) Marques, M. C.; Tapia, C.; Gutiérrez-Sanz, O.; Ramos, A. R.; Keller, K. L.; Wall, J. D.; De Lacey, A. L.; Matias, P. M.; Pereira, I. A. C. The Direct Role of Selenocysteine in [NiFeSe] Hydrogenase Maturation and Catalysis. *Nat. Chem. Biol.* **2017**, *13* (5), 544–550.

(59) Matsumoto, T.; Kishima, T.; Yatabe, T.; Yoon, K.-S.; Ogo, S. Mechanistic Insight into Switching between H_2 - or O_2 -Activation by Simple Ligand Effects of [NiFe]Hydrogenase Models. *Organometallics* **2017**, *36* (20), 3883–3890.

(60) Grapperhaus, C. A.; Darensbourg, M. Y. Oxygen Capture by Sulfur in Nickel Thiolates. *Acc. Chem. Res.* **1998**, *31* (8), 451–459.

(61) Lindenmaier, N. J.; Wahlefeld, S.; Bill, E.; Szilvási, T.; Eberle, C.; Yao, S.; Hildebrandt, P.; Horch, M.; Zebger, I.; Driess, M. An S-Oxygenated [NiFe] Complex Modelling Sulfenate Intermediates of an O_2 -Tolerant Hydrogenase. *Angew. Chem. Int. Ed.* **2017**, *56* (8), 2208–2211.

(62) Grapperhaus, C. A.; Maguire, M. J.; Tuntulani, T.; Darensbourg, M. Y. Singlet Oxygen and the Production of Sulfur Oxygenates of Nickel(II) and Palladium(II) Thiolates. *Inorg. Chem.* **1997**, *36* (9), 1860–1866.

(63) Farmer, P. J.; Solouki, T.; Mills, D. K.; Soma, T.; Russell, D. H.; Reibenspies, J. H.; Darensbourg, M. Y. Isotopic Labeling Investigation of the Oxygenation of Nickel-Bound Thiolates by Molecular Oxygen. *J. Am. Chem. Soc.* **1992**, *114* (12), 4601–4605.

(64) Grapperhaus, C. A.; Darensbourg, M. Y.; Sumner, L. W.; Russell, D. H. Template Effect for O_2 Addition across *Cis* -Sulfur Sites in Nickel Dithiolates. *J. Am. Chem. Soc.* **1996**, *118* (7), 1791–1792.

(65) Farmer, P. J.; Solouki, T.; Soma, T.; Russell, D. H.; Darensbourg, M. Y. Divergent Pathways for the Addition of Dioxygen to Sulfur in Nickel Cis-Dithiolates: An Isotopomeric Analysis. *Inorg. Chem.* **1993**, *32* (20), 4171–4172.

(66) Choudhury, S. B.; Pressler, M. A.; Mirza, S. A.; Day, R. O.; Maroney, M. J. Structure and Redox Chemistry of Analogous Nickel Thiolato and Selenolato Complexes: Implications for the Nickel Sites in Hydrogenases. *Inorg. Chem.* **1994**, *33* (22), 4831–4839.

(67) Yang, X.; Elrod, L. C.; Reibenspies, J. H.; Hall, M. B.; Darensbourg, M. Y. Oxygen Uptake in Complexes Related to [NiFeS]- and [NiFeSe]-Hydrogenase Active Sites. *Chem. Sci.* **2019**, *10* (5), 1368–1373.

(68) Jenkins, R. M.; Singleton, M. L.; Leamer, L. A.; Reibenspies, J. H.; Darensbourg, M. Y. Orientation and Stereodynamic Paths of Planar Monodentate Ligands in Square Planar Nickel N_2S Complexes. *Inorg. Chem.* **2010**, *49* (12), 5503–5514.

(69) Broering, E. P.; Dillon, S.; Gale, E. M.; Steiner, R. A.; Telser, J.; Brunold, T. C.; Harrop, T. C. Accessing Ni(III)-Thiolate Versus Ni(II)-Thiyl Bonding in a Family of $Ni–N_2S_2$ Synthetic Models of NiSOD. *Inorg. Chem.* **2015**, *54* (8), 3815–3828.

(70) Hohenberg, P.; Kohn, W. Inhomogeneous Electron Gas. *Phys. Rev.* **1964**, *136* (3B), B864–B871.

(71) Kohn, W.; Sham, L. J. Self-Consistent Equations Including Exchange and Correlation Effects. *Phys. Rev.* **1965**, *140* (4A), A1133–A1138.

(72) Perdew, J. P. Jacob's Ladder of Density Functional Approximations for the Exchange-Correlation Energy. In *AIP Conference Proceedings*; AIP: Antwerp (Belgium), 2001; Vol. 577, pp 1–20.

(73) Denny, J. A.; Darensbourg, M. Y. Metallodithiolates as Ligands in Coordination, Bioinorganic, and Organometallic Chemistry. *Chem. Rev.* **2015**, *115* (11), 5248–5273.

(74) Gale, E. M.; Cowart, D. M.; Scott, R. A.; Harrop, T. C. Dipeptide-Based Models of Nickel Superoxide Dismutase: Solvent Effects Highlight a Critical Role to Ni–S Bonding and Active Site Stabilization. *Inorg. Chem.* **2011**, *50* (20), 10460–10471.

(75) Huang, D.; Deng, L.; Sun, J.; Holm, R. H. Cleavage of Ni-(μ_2-S)-Ni Bridges in Dinuclear Nickel(II) Dithiolate Pincer Complexes and Related Reactions. *Inorg. Chem.* **2009**, *48* (13), 6159–6166.

(76) Yang, X.; Elrod, L. C.; Le, T.; Vega, V. S.; Naumann, H.; Rezenom, Y.; Reibenspies, J. H.; Hall, M. B.; Darensbourg, M. Y. Controlling O_2 Reactivity in Synthetic Analogues of [NiFeS]- and [NiFeSe]-Hydrogenase Active Sites. *J. Am. Chem. Soc.* **2019**, *141* (38), 15338–15347.

(77) Hammett, L. P. The Effect of Structure upon the Reactions of Organic Compounds. Benzene Derivatives. *J. Am. Chem. Soc.* **1937**, *59* (1), 96–103.

(78) Ding, S.; Ghosh, P.; Lunsford, A. M.; Wang, N.; Bhuvanesh, N.; Hall, M. B.; Darensbourg, M. Y. Hemilabile Bridging Thiolates as Proton Shuttles in Bioinspired H_2 Production Electrocatalysts. *J. Am. Chem. Soc.* **2016**, *138* (39), 12920–12927.

(79) Ghosh, P.; Quiroz, M.; Wang, N.; Bhuvanesh, N.; Darensbourg, M. Y. Complexes of $MN_2S_2 \cdot Fe(\eta^5\text{-}C_5R_5)(CO)$ as Platform for Exploring Cooperative

Heterobimetallic Effects in HER Electrocatalysis. *Dalton Trans.* **2017**, *46* (17), 5617–5624.

(80) Glendening, E. D.; Badenhoop, J. K.; Reed, A. E.; Carpenter, J. E.; Bohmann, J. A.; Morales, C. M.; Landis, C. R.; Weinhold, F. *NBO 6.0*; Theoretical Chemistry Institute, University of Wisconsin: Madison, WI, 2013.

(81) Liu, C.; Liu, T.; Hall, M. B. Influence of the Density Functional and Basis Set on the Relative Stabilities of Oxygenated Isomers of Diiron Models for the Active Site of [FeFe]-Hydrogenase. *J. Chem. Theory Comput.* **2015**, *11* (1), 205–214.

(82) Amend, J. P.; Aronson, H. S.; Macalady, J.; LaRowe, D. E. Another Chemolithotrophic Metabolism Missing in Nature: Sulfur Comproportionation. *Environ. Microbiol.* **2020**, *22* (6), 1971–1976.

(83) Ogata, H.; Lubitz, W.; Higuchi, Y. [NiFe] Hydrogenases: Structural and Spectroscopic Studies of the Reaction Mechanism. *Dalton Trans.* **2009**, No. 37, 7577.

(84) Frisch, M. J.; Trucks, G. W.; Schlegel, H. B.; Scuseria, G. E.; Robb, M. A.; Cheeseman, J. R.; Scalmani, G.; Barone, V.; Mennucci, B.; Peterson, G. A.; Nakatsuji, H.; Caricato, M.; Li, X.; Hratchian, H. P.; Izmaylov, A. F.; Bloino, J.; Zheng, G.; Gomperts, R.; Sonnenberg, J. L.; Hada, M.; Ehara, M.; Toyota, K.; Fukuda, R.; Hasegawa, J.; Ishida, M.; Nakajima, T.; Honda, Y.; Kitao, O.; Nakai, H.; Vreven, T.; Montgomery Jr., J. A.; Peralta, J. E.; Ogliaro, F.; Rega, N.; Bearpark, M. J.; Heyd, J. J.; Brothers, E.; Kudin, K. N.; Staroverov, V. N.; Keith, T. A.; Kobayashi, R.; Normand, J.; Raghavachari, K.; Rendell, A. P.; Burant, J.

C.; Iyengar, S. S.; Tomasi, J.; Cossi, M.; Rega, N.; Millam, J. M.; Klene, M.; Knox, J. E.; Cross, J. B.; Bakken, V.; Adamo, C.; Jaramillo, J.; Gomperts, R.; Stratmann, R. E.; Yazyev, O.; Austin, A. J.; Cammi, R.; Pomelli, C.; Ochterski, J. W.; Martin, R. L.; Morokuma, K.; Zakrzewski, V. G.; Voth, G. A.; Salvador, P.; Dannenberg, J. J.; Dapprich, S.; Daniels, A. D.; Farkas, O.; Foresman, J. B.; Ortiz, J. V.; Cioslowski, J.; Fox, D. J. *Gaussian 09, Revision D.01*; Gaussian, Inc.: Wallingford, CT, 2013.

(85) Frisch, M. J.; Trucks, G. W.; Schlegel, H. B.; Scuseria, G. E.; Robb, M. A.; Cheeseman, J. R.; Scalmani, G.; Barone, V.; Peterson, G. A.; Nakatsuji, H.; Li, X.; Caricato, M.; Marenich, A. V.; Bloino, J.; Janesko, B. G.; Gomperts, R.; Mennucci, B.; Hratchian, H. P.; Ortiz, J. V.; Izmaylov, A. F.; Sonnenberg, J. L.; Williams-Young, D.; Ding, F.; Lipparini, F.; Egidi, F.; Goings, J.; Peng, B.; Petrone, A.; Henderson, T.; Ranasinghe, D.; Zakrzewski, V. G.; Gao, J.; Rega, N.; Zheng, G.; Liang, W.; Hada, M.; Ehara, M.; Toyota, K.; Fukuda, R.; Hasegawa, J.; Ishida, M.; Nakajima, T.; Honda, Y.; Kitao, O.; Nakai, H.; Vreven, T.; Throssell, K.; Montgomery Jr., J. A.; Peralta, J. E.; Ogliaro, F.; Bearpark, M. J.; Heyd, J. J.; Brothers, E. N.; Kudin, K. N.; Staroverov, V. N.; Keith, T. A.; Kobayashi, R.; Normand, J.; Raghavachari, K.; Rendell, A. P.; Burant, J. C.; Iyengar, S. S.; Tomasi, J.; Cossi, M.; Millam, J. M.; Klene, M.; Adamo, C.; Cammi, R.; Ochterski, J. W.; Martin, R. L.; Morokuma, K.; Farkas, O.; Foresman, J. B.; Fox, D. J. *Gaussian 16, Revision B.01*; Gaussian, Inc.: Wallingford, CT, 2016.

(86) *AMPAC 9*; Semichem Inc: Shawnee, KS, 2008.

(87) Mardirossian, N.; Head-Gordon, M. Thirty Years of Density Functional Theory in Computational Chemistry: An Overview and Extensive Assessment of 200 Density Functionals. *Mol. Phys.* **2017**, *115* (19), 2315–2372.

(88) Ogo, S. H2 and O2 Activation by [NiFe]Hydrogenases – Insights from Model Complexes. *Coord. Chem. Rev.* **2017**, *334*, 43–53.

(89) Ogo, S. H_2 and O_2 Activation-A Remarkable Insight into Hydrogenase: H_2 and O_2 Activation by Hydrogenase. *Chem. Rec.* **2014**, *14* (3), 397–409.

(90) Breglia, R.; Greco, C.; Fantucci, P.; De Gioia, L.; Bruschi, M. Theoretical Investigation of Aerobic and Anaerobic Oxidative Inactivation of the [NiFe]-Hydrogenase Active Site. *Phys. Chem. Chem. Phys.* **2018**, *20* (3), 1693–1706.

(91) Breglia, R.; Greco, C.; Fantucci, P.; De Gioia, L.; Bruschi, M. Reactivation of the Ready and Unready Oxidized States of [NiFe]-Hydrogenases: Mechanistic Insights from DFT Calculations. *Inorg. Chem.* **2019**, *58* (1), 279–293.

(92) Westheimer, F. Why Nature Chose Phosphates. *Science* **1987**, *235* (4793), 1173–1178.

(93) Pan, Z.-H.; Tao, Y.-W.; He, Q.-F.; Wu, Q.-Y.; Cheng, L.-P.; Wei, Z.-H.; Wu, J.-H.; Lin, J.-Q.; Sun, D.; Zhang, Q.-C.; Tian, D.; Luo, G.-G. The Difference Se Makes: A Bio-Inspired Dppf-Supported Nickel Selenolate Complex Boosts Dihydrogen Evolution with High Oxygen Tolerance. *Chem. - Eur. J.* **2018**, *24* (33), 8275–8280.

(94) Huang, W.; Jia, J.; Cummings, J.; Nelson, M.; Schneider, G.; Lindqvist, Y. Crystal Structure of Nitrile Hydratase Reveals a Novel Iron Centre in a Novel Fold. *Structure* **1997**, *5* (5), 691–699.

(95) Song, L.; Wang, M.; Shi, J.; Xue, Z.; Wang, M.-X.; Qian, S. High Resolution X-Ray Molecular Structure of the Nitrile Hydratase from Rhodococcus Erythropolis AJ270 Reveals Posttranslational Oxidation of Two Cysteines into Sulfinic Acids and a Novel Biocatalytic Nitrile Hydration Mechanism. *Biochem. Biophys. Res. Commun.* **2007**, *362* (2), 319–324.

(96) Doukov, T. I. A Ni-Fe-Cu Center in a Bifunctional Carbon Monoxide Dehydrogenase/ Acetyl-CoA Synthase. *Science* **2002**, *298* (5593), 567–572.

(97) Darnault, C.; Volbeda, A.; Kim, E. J.; Legrand, P.; Vernède, X.; Lindahl, P. A.; Fontecilla-Camps, J. C. Ni-Zn-[Fe4-S4] and Ni-Ni-[Fe4-S4] Clusters in Closed and Open α Subunits of Acetyl-CoA Synthase/Carbon Monoxide Dehydrogenase. *Nat. Struct. Mol. Biol.* **2003**, *10* (4), 271–279.

(98) Svetlitchnyi, V.; Dobbek, H.; Meyer-Klaucke, W.; Meins, T.; Thiele, B.; Romer, P.; Huber, R.; Meyer, O. A Functional Ni-Ni-[4Fe-4S] Cluster in the Monomeric Acetyl-CoA Synthase from Carboxydothermus Hydrogenoformans. *Proc. Natl. Acad. Sci.* **2004**, *101* (2), 446–451.

(99) Kruger, H. J.; Peng, Gang.; Holm, R. H. Low-Potential Nickel(III,II) Complexes: New Systems Based on Tetradentate Amidate-Thiolate Ligands and the Influence of Ligand Structure on Potentials in Relation to the Nickel Site in [NiFe]-Hydrogenases. *Inorg. Chem.* **1991**, *30* (4), 734–742.

(100) Duff, S. E.; Barclay, J. E.; Davies, S. C.; Evans, D. J. Homonuclear Dinickel Complexes: Structural Mimics for the Dinickel Subsite of the A-Cluster of Acetyl-CoA Synthase. *Inorg. Chem. Commun.* **2005**, *8* (2), 170–173.

(101) Zhao, T.; Ghosh, P.; Martinez, Z.; Liu, X.; Meng, X.; Darensbourg, M. Y. Discrete Air-Stable Nickel(II)–Palladium(II) Complexes as Catalysts for Suzuki–Miyaura Reactions. *Organometallics* **2017**, *36* (9), 1822–1827.

(102) Rampersad, M. V.; Jeffery, S. P.; Reibenspies, J. H.; Ortiz, C. G.; Darensbourg, D. J.; Darensbourg, M. Y. N2S2Ni Metallothiolates as a Class of Ligands That Support Organometallic and Bioorganometallic Reactivity. *Angew. Chem. Int. Ed.* **2005**, *44* (8), 1217–1220.

(103) Lunsford, A. M.; Goldstein, K. F.; Cohan, M. A.; Denny, J. A.; Bhuvanesh, N.; Ding, S.; Hall, M. B.; Darensbourg, M. Y. Comparisons of MN_2S_2 vs. Bipyridine as Redox-Active Ligands to Manganese and Rhenium in $(L–L)M'(CO)_3Cl$ Complexes. *Dalton Trans.* **2017**, *46* (16), 5175–5182.

(104) Bourrez, M.; Molton, F.; Chardon-Noblat, S.; Deronzier, A. [Mn(Bipyridyl)(CO)3Br]: An Abundant Metal Carbonyl Complex as Efficient Electrocatalyst for CO2 Reduction. *Angew. Chem. Int. Ed.* **2011**, *50* (42), 9903–9906.

(105) Franco, F.; Cometto, C.; Ferrero Vallana, F.; Sordello, F.; Priola, E.; Minero, C.; Nervi, C.; Gobetto, R. A Local Proton Source in a $[Mn(Bpy\text{-}R)(CO)_3Br]$-Type Redox Catalyst Enables CO_2 Reduction Even in the Absence of Brønsted Acids. *Chem Commun* **2014**, *50* (93), 14670–14673.

(106) Agarwal, J.; Shaw, T. W.; Schaefer, H. F.; Bocarsly, A. B. Design of a Catalytic Active Site for Electrochemical CO_2 Reduction with Mn(I)-Tricarbonyl Species. *Inorg. Chem.* **2015**, *54* (11), 5285–5294.

(107) Sampson, M. D.; Kubiak, C. P. Manganese Electrocatalysts with Bulky Bipyridine Ligands: Utilizing Lewis Acids To Promote Carbon Dioxide Reduction at Low Overpotentials. *J. Am. Chem. Soc.* **2016**, *138* (4), 1386–1393.

(108) Franco, F.; Cometto, C.; Nencini, L.; Barolo, C.; Sordello, F.; Minero, C.; Fiedler, J.; Robert, M.; Gobetto, R.; Nervi, C. Local Proton Source in Electrocatalytic CO_2 Reduction with [Mn(Bpy-R)$(CO)_3$Br] Complexes. *Chem. - Eur. J.* **2017**, *23* (20), 4782–4793.

(109) Ngo, K. T.; McKinnon, M.; Mahanti, B.; Narayanan, R.; Grills, D. C.; Ertem, M. Z.; Rochford, J. Turning on the Protonation-First Pathway for Electrocatalytic CO_2 Reduction by Manganese Bipyridyl Tricarbonyl Complexes. *J. Am. Chem. Soc.* **2017**, *139* (7), 2604–2618.

(110) Sung, S.; Li, X.; Wolf, L. M.; Meeder, J. R.; Bhuvanesh, N. S.; Grice, K. A.; Panetier, J. A.; Nippe, M. Synergistic Effects of Imidazolium-Functionalization on *Fac* -Mn$(CO)_3$ Bipyridine Catalyst Platforms for Electrocatalytic Carbon Dioxide Reduction. *J. Am. Chem. Soc.* **2019**, *141* (16), 6569–6582.

(111) Machan, C. W.; Sampson, M. D.; Chabolla, S. A.; Dang, T.; Kubiak, C. P. Developing a Mechanistic Understanding of Molecular Electrocatalysts for CO_2 Reduction Using Infrared Spectroelectrochemistry. *Organometallics* **2014**, *33* (18), 4550–4559.

(112) Grills, D. C.; Farrington, J. A.; Layne, B. H.; Lymar, S. V.; Mello, B. A.; Preses, J. M.; Wishart, J. F. Mechanism of the Formation of a Mn-Based CO_2 Reduction Catalyst Revealed by Pulse Radiolysis with Time-Resolved Infrared Detection. *J. Am. Chem. Soc.* **2014**, *136* (15), 5563–5566.

(113) Jenkins, R. M.; Pinder, T. A.; Hatley, M. L.; Reibenspies, J. H.; Darensbourg, M. Y. Tetradentate N_2S_2 Vanadyl(IV) Coordination Complexes: Synthesis, Characterization, and Reactivity Studies. *Inorg. Chem.* **2011**, *50* (5), 1849–1855.

(114) Le, T.; Nguyen, H.; Perez, L. M.; Darensbourg, D. J.; Darensbourg, M. Y. Metal-Templated, Tight Loop Conformation of a Cys-X-Cys Biomimetic Assembles a Dimanganese Complex. *Angew. Chem. Int. Ed.* **2020**, *59* (9), 3645–3649.

(115) Reichardt, C.; Welton, T. Empirical Parameters of Solvent Polarity. In *Solvents and Solvent Effects in Organic Chemistry*; Wiley-VCH, 2010; pp 425–508.

(116) Britt, R. D.; Rao, G.; Tao, L. Biosynthesis of the Catalytic H-Cluster of [FeFe] Hydrogenase: The Roles of the Fe–S Maturase Proteins HydE, HydF, and HydG. *Chem. Sci.* **2020**, *11* (38), 10313–10323.

(117) Dunbar, R. C.; Martens, J.; Berden, G.; Oomens, J. Complexes of Ni(II) and Cu(II) with Small Peptides: Deciding Whether to Deprotonate. *Phys. Chem. Chem. Phys.* **2016**, *18* (38), 26923–26932.

(118) Francke, R.; Little, R. D. Redox Catalysis in Organic Electrosynthesis: Basic Principles and Recent Developments. *Chem. Soc. Rev.* **2014**, *43* (8), 2492.

(119) Luca, O. R.; Crabtree, R. H. Redox-Active Ligands in Catalysis. *Chem Soc Rev* **2013**, *42* (4), 1440–1459.

(120) Feltham, H. L. C.; Brooker, S. Review of Purely 4f and Mixed-Metal Nd-4f Single-Molecule Magnets Containing Only One Lanthanide Ion. *Coord. Chem. Rev*. **2014**, *276*, 1–33.

(121) Woodruff, D. N.; Winpenny, R. E. P.; Layfield, R. A. Lanthanide Single-Molecule Magnets. *Chem. Rev.* **2013**, *113* (7), 5110–5148.

(122) Layfield, R. A. Organometallic Single-Molecule Magnets. *Organometallics* **2014**, *33* (5), 1084–1099.

(123) Comstock, R. L. Review Modern Magnetic Materials in Data Storage. 15.

(124) Kaes, C.; Katz, A.; Hosseini, M. W. Bipyridine: The Most Widely Used Ligand. A Review of Molecules Comprising at Least Two 2,2‘-Bipyridine Units. *Chem. Rev*. **2000**, *100* (10), 3553–3590.

(125) Constable; Housecroft. The Early Years of 2,2’-Bipyridine—A Ligand in Its Own Lifetime. *Molecules* **2019**, *24* (21), 3951.

(126) Enemark, J. H.; Feltham, R. D. Principles of Structure, Bonding, and Reactivity for Metal Nitrosyl Complexes. *Coord. Chem. Rev.* **1974**, *13* (4), 339–406.

(127) Johnson, D. C.; Dean, D. R.; Smith, A. D.; Johnson, M. K. Structure, Function, and Formation of Biological Iron-Sulfur Clusters. *Annu. Rev. Biochem.* **2005**, *74* (1), 247–281.

(128) Mouesca, J.-M.; Lamotte, B. Iron–Sulfur Clusters and Their Electronic and Magnetic Properties. *Coord. Chem. Rev.* **1998**, *178–180*, 1573–1614.

(129) Noodleman, L.; Peng, C. Y.; Case, D. A.; Mouesca, J.-M. Orbital Interactions, Electron Delocalization and Spin Coupling in Iron-Sulfur Clusters. *Coord. Chem. Rev*. **1995**, *144*, 199–244.

(130) Carney, M. J.; Papaefthymiou, G. C.; Spartalian, K.; Frankel, R. B.; Holm, R. H. Ground Spin State Variability in [Fe4S4(SR)4]3-. Synthetic Analogs of the Reduced Clusters in Ferredoxins and Other Iron-Sulfur Proteins: Cases of Extreme Sensitivity of Electronic State and Structure to Extrinsic Factors. *J. Am. Chem. Soc.* **1988**, *110* (18), 6084–6095.

(131) Sawyer, D. T.; Srivatsa, G. Susan.; Bodini, M. E.; Schaefer, W. P.; Wing, R. M. Redox Chemistry and Spectroscopy of Toluene-3,4-Dithiol (TDTH2) and of Its M(TDT)22-/- Complexes with Zinc(II), Copper(II), Nickel(II), Cobalt(II), Iron(II), and Manganese(II). Formation of a Stable Dn-(.Cntdot.SR) Bond upon Oxidation by One Electron. *J. Am. Chem. Soc.* **1986**, *108* (5), 936–942.

(132) Zuleta, J. A.; Bevilacqua, J. M.; Eisenberg, R. Solvatochromic and Emissive Properties of Pt(II) Complexes with 1,1- and 1,2-Ditholates. *Coord. Chem. Rev.* **1991**, *111*, 237–248.

(133) Cassoux, P.; Valade, L.; Kobayashi, H.; Kobayashi, A. Molecular Metals and Superconductors Derived from Metal Complexes of 1,3-Dithiol-2-Thione-4,5-Dithiolate (DMIT). *Coord. Chem. Rev.* **1991**, *110*, 115–160.

(134) Dang, L.; Yang, X.; Zhou, J.; Brothers, E. N.; Hall, M. B. Computational Studies on Ethylene Addition to Nickel Bis(Dithiolene). *J. Phys. Chem. A* **2012**, *116* (1), 476–482.

(135) Dang, L.; Shibl, M. F.; Yang, X.; Alak, A.; Harrison, D. J.; Fekl, U.; Brothers, E. N.; Hall, M. B. The Mechanism of Alkene Addition to a Nickel Bis(Dithiolene) Complex: The Role of the Reduced Metal Complex. *J. Am. Chem. Soc.* **2012**, *134* (10), 4481–4484.

(136) Dang, L.; Shibl, M. F.; Yang, X.; Harrison, D. J.; Alak, A.; Lough, A. J.; Fekl, U.; Brothers, E. N.; Hall, M. B. Apparent Anti-Woodward–Hoffmann Addition to a Nickel Bis(Dithiolene) Complex: The Reaction Mechanism Involves Reduced, Dimetallic Intermediates. *Inorg. Chem.* **2013**, *52* (7), 3711–3723.

(137) Moscattini, J.; Lough, A. J.; Fekl, U. C2-Isomer of [Pd(Tfd)]6 [Tfd Is S2C2(CF3)2] as Its Benzene Solvate: A New Member of the Small but Growing Class of Homoleptic Palladium(II) Monodi-thio-lenes in the Form of Hexa-meric Cubes. *Acta Crystallogr. Sect. E Crystallogr. Commun.* **2017**, *73* (7), 957–962.

(138) Gutmann, V. *The Donor-Acceptor Approach to Molecular Interactions*; Plenum Press: New York, 1978.

(139) Kitagawa, Y.; Saito, T.; Nakanishi, Y.; Kataoka, Y.; Matsui, T.; Kawakami, T.; Okumura, M.; Yamaguchi, K. Spin Contamination Error in Optimized Geometry of Singlet Carbene ($^{1}A_{1}$) by Broken-Symmetry Method. *J. Phys. Chem. A* **2009**, *113* (52), 15041–15046.

(140) Neese, F. The ORCA Program System. *WIREs Comput. Mol. Sci.* **2012**, *2* (1), 73–78.

(141) Neese, F. Software Update: The ORCA Program System, Version 4.0. *WIREs Comput. Mol. Sci.* **2018**, *8* (1).

(142) Liddle, S. T.; van Slageren, J. Improving F-Element Single Molecule Magnets. *Chem. Soc. Rev.* **2015**, *44* (19), 6655–6669.

(143) Nunzi, F.; Ruiz, E.; Cano, J.; Alvarez, S. Strong Antiferromagnetic Coupling at Long Distance through a Ligand to Metal Charge Transfer Mechanism. *J. Phys. Chem. C* **2007**, *111* (2), 618–621.

(144) De Luca, G. M.; Ghiringhelli, G.; Perroni, C. A.; Cataudella, V.; Chiarella, F.; Cantoni, C.; Lupini, A. R.; Brookes, N. B.; Huijben, M.; Koster, G.; Rijnders, G.; Salluzzo, M. Ubiquitous Long-Range Antiferromagnetic Coupling across the Interface between Superconducting and Ferromagnetic Oxides. *Nat. Commun.* **2014**, *5* (1), 5626.

(145) McGuire, J.; Miras, H. N.; Donahue, J. P.; Richards, E.; Sproules, S. Ligand Radicals as Modular Organic Electron Spin Qubits. *Chem. – Eur. J.* **2018**, *24* (66), 17598–17605.

(146) Dagotto, E.; Rice, T. M. Surprises on the Way from One- to Two-Dimensional Quantum Magnets: The Ladder Materials. *Science* **1996**, *271* (5249), 618–623.

(147) Pokhilko, P.; Bezrukov, D. S.; Krylov, A. I. Is Solid Copper Oxalate a Spin Chain or a Mixture of Entangled Spin Pairs? *J. Phys. Chem. C* **2021**, *125* (13), 7502–7510.

(148) Appel, A. M.; Bercaw, J. E.; Bocarsly, A. B.; Dobbek, H.; DuBois, D. L.; Dupuis, M.; Ferry, J. G.; Fujita, E.; Hille, R.; Kenis, P. J. A.; Kerfeld, C. A.; Morris, R. H.; Peden, C. H. F.; Portis, A. R.; Ragsdale, S. W.; Rauchfuss, T. B.; Reek, J. N. H.; Seefeldt, L. C.; Thauer, R. K.; Waldrop, G. L. Frontiers, Opportunities, and

Challenges in Biochemical and Chemical Catalysis of CO_2 Fixation. *Chem. Rev.* **2013**, *113* (8), 6621–6658.

(149) Yadav, R. K.; Baeg, J.-O.; Oh, G. H.; Park, N.-J.; Kong, K.; Kim, J.; Hwang, D. W.; Biswas, S. K. A Photocatalyst–Enzyme Coupled Artificial Photosynthesis System for Solar Energy in Production of Formic Acid from CO_2. *J. Am. Chem. Soc.* **2012**, *134* (28), 11455–11461.

(150) Merz, K. M.; Banci, L. Binding of Bicarbonate to Human Carbonic Anhydrase II: A Continuum of Binding States. *J. Am. Chem. Soc.* **1997**, *119* (5), 863–871.

(151) Rodríguez-Maciá, P.; Reijerse, E. J.; van Gastel, M.; DeBeer, S.; Lubitz, W.; Rüdiger, O.; Birrell, J. A. Sulfide Protects [FeFe] Hydrogenases From O_2. *J. Am. Chem. Soc.* **2018**, *140* (30), 9346–9350.

(152) Morra, S.; Arizzi, M.; Valetti, F.; Gilardi, G. Oxygen Stability in the New [FeFe]-Hydrogenase from *Clostridium Beijerinckii* SM10 (CbA5H). *Biochemistry* **2016**, *55* (42), 5897–5900.

(153) Corrigan, P. S.; Tirsch, J. L.; Silakov, A. Investigation of the Unusual Ability of the [FeFe] Hydrogenase from *Clostridium Beijerinckii* to Access an O_2-Protected State. *J. Am. Chem. Soc.* **2020**, *142* (28), 12409–12419.

(154) Kubas, A.; Orain, C.; De Sancho, D.; Saujet, L.; Sensi, M.; Gauquelin, C.; Meynial-Salles, I.; Soucaille, P.; Bottin, H.; Baffert, C.; Fourmond, V.; Best, R. B.; Blumberger, J.; Léger, C. Mechanism of O2 Diffusion and Reduction in FeFe Hydrogenases. *Nat. Chem.* **2017**, *9* (1), 88–95.

(155) Ahmed, M. E.; Dey, S.; Darensbourg, M. Y.; Dey, A. Oxygen-Tolerant H_2 Production by [FeFe]-H_2 Ase Active Site Mimics Aided by Second Sphere Proton Shuttle. *J. Am. Chem. Soc.* **2018**, *140* (39), 12457–12468.

(156) Qiu, S.; Olsen, S.; MacFarlane, D. R.; Sun, C. The Oxygen Reduction Reaction on [NiFe] Hydrogenases. *Phys. Chem. Chem. Phys.* **2018**, *20* (36), 23528–23534.

(157) Breglia, R.; Ruiz-Rodriguez, M. A.; Vitriolo, A.; Gonzàlez-Laredo, R. F.; De Gioia, L.; Greco, C.; Bruschi, M. Theoretical Insights into [NiFe]-Hydrogenases Oxidation Resulting in a Slowly Reactivating Inactive State. *JBIC J. Biol. Inorg. Chem.* **2017**, *22* (1), 137–151.

(158) Breglia, R.; De Gioia, L.; Greco, C.; Bruschi, M. Theory Related to [FeFe]- and [NiFe]-Hydrogenases: Stereoelectronic Properties, H-Cluster Oxidation, and Mechanisms for Increasing Oxygen Tolerance. In *Microalgal Hydrogen Production: Achievements and Perspectives*; Royal Society of Chemistry, 2018; pp 67–106.